

In presenting this dissertation in partial fulfillment of the requirements for an advanced degree at Idaho State University, I agree that the Library shall make it freely available for inspection. I further state that permission to download and/or print my dissertation for scholarly purposes may be granted by the Dean of Graduate School, Dean of my academic division, or by the University Librarian. It is understood that any copying or publication of this dissertation for financial gain shall not be allowed without my written permission.

Signature_____

Date_____

The Sensitivity of Mountain Snowpack to Warming

By

Christopher J. Tennant

A dissertation submitted in partial fulfillment

of the requirements for the degree of

Doctor of Philosophy in the Department of Geosciences

Idaho State University

August, 2015

To the Graduate Faculty:

The members of the committee appointed to examine the dissertation of CHRISTOPHER J. TENNANT find it satisfactory and recommend that it be accepted.

Dr. Benjamin T. Crosby, Major Advisor

Dr. Sarah E. Godsey, Committee Member

Dr. Kathleen A. Lohse, Committee Member

Dr. Robert W. VanKirk, Committee Member

Dr. Colden V. Baxter, Graduate Faculty Representative

Acknowledgements

I extend the dearest gratitude and thanks to my committee members: Dr. Benjamin Crosby, Dr. Sarah Godsey, Dr. Kathleen Lohse, Dr. DeWayne Derryberry, and Dr. Robert VanKirk and to my graduate faculty representative Dr. Colden Baxter. A special thanks is extended to Drs. Crosby and Godsey for their roles as my primary advisers. The work presented in this dissertation was supported by a NASA Idaho Space Grant Consortium Fellowship, NSF awards EPS-0814387 and EPS-1006968 from the Idaho NSF EPSCoR Program, National Science Foundation award EAR 1349384, RC CZO Cooperative Agreement EAR 1331872, and a National Science Foundation CZO SAVI Award # 1445246. My deepest thanks is extended to my family for their enduring support; thank you Jude, Quinn, and Renee, you guys are the best!

Table of Contents

List of Figures.....	viii
List of Tables.....	x
Abstract.....	xi

Chapter 1: Introduction

1.1 Why study the sensitivity of mountain snowpack to warming?.....	1
1.2 Background	1
1.3 Guiding hypotheses and project objectives.....	2
1.4 Dissertation Structure.....	4

Chapter 2: A simple framework for assessing the sensitivity of mountain watersheds to warming-driven snowpack loss

2.1 Abstract	7
2.2 Introduction	8
2.3 Methods & Experimental Design.....	9
2.3.1 Elevation-based Framework	9
2.3.2 Current and Future Peak SWE-Elevation Relationships	12
2.3.3 Areal-Average Peak SWE Estimation for Simulated Elevation Distributions 15	
2.3.4 Current and Future Snowline Elevations	15
2.3.5 Extent of Evergreen Forest	16
2.3.6 Snowpack Sensitivity Metrics.....	17
2.4 Discussion of Simulation Results.....	17
2.4.1 Peak SWE Loss.....	17
2.4.2 Area Above Snowline (AAS) Loss.....	19
2.4.3 Potential Model Limitations	20
2.4.4 Examples of Model Application.....	21
2.5 Conclusions	22
2.6 Acknowledgements	23
2.7 Figures and Tables	24

Chapter 3: The sensitivity of Rocky Mountain ecoregions to snowpack loss

3.1	Abstract	32
3.2	Introduction	33
3.3	Setting.....	35
3.4	Methods.....	36
3.4.1	Elevation-based framework	36
3.4.2	Snowpack-based framework.....	38
3.4.3	Simulating watershed warming-driven snowpack loss.....	41
3.4.4	Geographically weighted regression of watershed peak SWE loss	41
3.5	Results and discussion.....	44
3.5.1	Inter-ecoregion patterns of peak SWE loss.....	44
3.5.2	Intra-ecoregion patterns of peak SWE loss.....	46
3.5.3	Spatial structure of ecoregion peak SWE loss	47
3.6	Conclusions	50
3.7	Acknowledgements	51
3.8	Figures and Tables	52
	References.....	62

Chapter 4: The influence of elevation, aspect, and vegetation on seasonal snowpack: case studies from five mountain Critical Zone Observatory sites across the western U.S.

4.1	Abstract	66
4.2	Introduction	67
4.3	Data description and Critical Zone Observatories	70
4.3.1	LiDAR-derived snow depths	70
4.3.2	Boulder Creek Watershed (BCW)	72
4.3.3	Jemez River Basin (JRB).....	74
4.3.4	Reynolds Creek Experimental Watershed (KREW).....	74
4.3.5	Southern Sierra Critical Zone Observatory.....	75
4.4	Methods.....	77

4.4.1	Snow depth, vegetation, and topographic analyses	77
4.4.2	Elevation and snowpack distribution comparison	78
4.4.3	Statistical analyses of snow depths in alpine, forested, and shrubland areas 78	
4.5	Results and discussion.....	79
4.5.1	How consistent are snow depth-elevation relationships?	79
4.5.2	Does hypsometry accurately predict where the majority of snow volume is stored? 80	
4.5.3	Aspect-dependent snow depths in forested and open terrain.....	81
4.6	Conclusions	84
4.7	Acknowledgements	85
4.8	Figures	86
5	Appendix 1.....	96
6	Appendix 2.....	107
7	Appendix 3.....	120

List of Figures

- Figure 2.1. Examples of the influence of location (μ), scale (σ), and shape (k) parameters on a series of generalized extreme value probability distributions for watershed elevations.
- Figure 2.2. Peak snow water equivalent (SWE) as a function of elevation with the best-fit Richard's function.
- Figure 2.3. Catchment-wide predictions of peak SWE loss and loss of area above snowline given +1° to +5°C warming.
- Figure 3.1. HUC-10 watersheds and U.S. EPA Level-III ecoregion boundaries.
- Figure 3.2. Idealized plot showing how the generalized extreme value (GEV) distribution parameters are used to characterize mountain watershed elevation distributions. Three parameters, the location (μ), scale (σ), and shape (k), describe the central tendency, variance, and shape (skewness and kurtosis) of the distribution.
- Figure 3.3. All-ecoregion comparison of average annual peak SWE-elevation relation for water years 2004 – 2014. The average annual peak SWE-elevation relationships for the four ecoregions with the combined Richard's/linear fits as solid lines. All-ecoregion comparison of elevation distributions.
- Figure 3.4. Predicted loss in the average annual peak SWE-elevation relationship for the Canadian Rockies, Idaho Batholith, Middle Rockies, and Northern Rockies with warming.
- Figure 3.5. Absolute and relative peak SWE loss for +1°C to + 4°C warming for HUC 10 watersheds located in the Canadian Rockies, Idaho Batholith, Middle Rockies, and Northern Rockies ecoregions.
- Figure 3.6. Relationships between the watershed location parameter (μ) of HUC-10 watersheds and absolute and relative (cumulative peak SWE loss for the Canadian Rockies, Idaho Batholith, Middle Rockies, and Northern Rockies ecoregions.
- Figure 3.7. Maps and watershed elevation distributions of absolute and relative average annual peak SWE loss with +1°C warming for HUC-10 watersheds within the Canadian Rockies, Idaho Batholith, Middle Rockies, and Northern Rockies ecoregions.
- Figure 3.8. Spatial autocorrelation (Moran's I) of absolute peak SWE loss for HUC-10 watersheds in the Canadian Rockies, Idaho Batholith, Middle Rockies and Northern Rockies ecoregions.

Figure 4.1. Locations of critical zone observatories, Boulder Creek Watershed (BCW), Jemez River Basin (JRB), Kings River Experimental Watershed (KREW), Reynolds Creek Watershed (RCW), and Wolverton Basin (WOLV).

Figure 4.2. Elevation-area relationships, percent of land area grouped by aspect, and percent of land area grouped by vegetation cover for the snow-covered extents of the Critical Zone Observatories.

Figure 4.3. Binned snow depth plotted against elevation for the Critical Zone Observatories.

Figure 4.4. Snow depth and area for the Critical Zone Observatories.

Figure 4.5: Comparison of aspect-dependent snow depths in alpine, forested, and shrubland areas for the Critical Zone Observatories.

List of tables

Table 2.1 Summary statistics for HUC-10 catchments in each ecoregion and for all four ecoregions combined. Bayesian information criterion (BIC) routinely selected the generalized extreme value (GEV) as the best fit for catchment elevation distributions. The GEV parameters location, scale, and shape characterize the central tendency, variability, and shape, respectively, of a catchment's elevation distribution.

Table 2.2. Summary of Richard's parameters describing A , the maximum peak SWE, M , the maximum slope, λ , the elevation where peak SWE exhibits rapid increase and ν , the shape parameter of average annual peak SWE-elevation for water years 2004 – 2014.

The Sensitivity of Mountain Snowpack to Warming

Abstract

Mountain snowpack provides a reservoir of water that sustains human and ecological systems around the globe. The reliability of snowpack-derived water sources is threatened by warming. A simple function relating warming, elevation, and snowpack was identified and used to simulate snowpack losses for a large number of western U.S. watersheds. Regression analyses of simulation results demonstrate that snowpack loss is best described by three topographic parameters identifying the central tendency, variance, and shape of watershed elevation distributions. Responses to warming were nonlinear and emphasize that the sensitivity of snowpack will likely be watershed-dependent. This framework was further tested across watersheds in four Rocky Mountain ecoregions covering a wider range of topographic and climatic conditions. This study demonstrates that snowpack losses will likely vary between and within ecoregions. Simulated peak SWE losses across watersheds with an ecoregion varied from less than 100 mm to more than 400 mm for +4°C warming. The spatial structure of snowpack loss was also ecoregion-dependent. In some ecoregions, the strength and distance of positive autocorrelation between snowpack losses increased with warming, suggesting that nearby watersheds will respond similarly. In other ecoregions, the distance and strength of positive autocorrelation decreased, indicating more variable responses to warming. I then used high-resolution, spatially-extensive snow-on, snow-off Light Detection and Ranging surveys from five Critical Zone Observatory (CZO) sites across the western U.S. to evaluate the influence of elevation, aspect, and forest cover on the spatial distribution of

seasonal snow accumulation. All of the CZO sites exhibited increases in snow depth with elevation; however, the relationship between snow depth and elevation was not monotonic and rates of increase varied from site to site. The elevation distributions of the CZOs generally predicted snow volume distributions with high accuracy, implying that hypsometry will be useful for measuring a watershed's sensitivity to warming-driven snowpack loss. At sites where elevation less reliably predicted snow storage, wind transport and aspect-dependent snow storage were important. Results from this study emphasize that the interaction of regional-scale mass and energy fluxes with site specific topographic and vegetation characteristics can produce a wide array of patterns in local snow accumulation.

Chapter 1: Introduction

1.1 Why study the sensitivity of mountain snowpack to warming?

In the western U.S. alone, water resources derived from mountain regions support over 60 million people [*Bales et al.*, 2006]. Numerous studies indicate that past warming has caused declines in mountain snowpacks [e.g. *Mote et al.*, 2005; *Pederson et al.*, 2011a] and affected the amount and timing of snowmelt runoff [*Luce and Holden*, 2009; *Luce et al.*, 2013; *Pederson et al.*, 2011b]. Snowmelt derived waters are essential in providing potable water, irrigation, ecosystem services, and recreational opportunities to communities residing in or near mountainous regions [*Barnett et al.*, 2008]. High certainty of future warming and continued population growth [*IPCC*, 2014] increase the demand for reliable water resources and motivate an evaluation of the sensitivity of mountain snowpack to warming. In particular, identifying which mountain watersheds will be more sensitive or more resistant to warming and the controls driving these differences is of paramount significance to the human and ecological systems they support.

1.2 Background

The observed declines in mountain snowpack [e.g. *Mote et al.*, 2005; *Pederson et al.*, 2011] and changes in the amounts and timing of annual streamflow [*Luce and Holden*, 2009; *Luce et al.*, 2013; *Pederson et al.*, 2011b] are attributed to many factors. They include, but are not limited to; increases in air temperatures [*Hamlet et al.*, 2005; *Pederson et al.*, 2013], variability in the strength of Pacific decadal oscillation cycles [*Hamlet et al.*, 2005], reduced strength of westerly winds [*Luce et al.*, 2013], and increases in elevation of freezing levels [*Abatzoglou*, 2011]. Synoptic-scale climatic

drivers can be correlated to regional scale snowpack losses [e.g. *Pederson et al.*, 2013], but, the magnitude and even the direction of response of individual watersheds and entire mountainous regions have been observed to diverge from broader-scale patterns, as documented by *Stewart* [2009] and *Giroto et al.* [2014]. This divergence likely originates from variability in regional-scale orography [*Houze*, 2012 and *Roe*, 2005] and variability in the elevation and topographic characteristics of individual watersheds [*Stewart*, 2009].

Steep topography can affect both precipitation amount and phase. For example, reviews of orographic precipitation from *Houze* [2012] and *Roe* [2005] find that precipitation amounts at high elevation meteorological stations can be five times as much as those at low elevation stations. *Kirchner et al.* [2014] recently used spatially extensive measurements of snow depth at the peak of seasonal accumulation to demonstrate that instrumental stations did not capture the full pattern or rate of increase in snow depth with elevation. Data assimilation approaches utilizing physically-driven mass and energy snow balance models, coupled with satellite observations to predict snow depth and snow water equivalent confirm that meteorological stations often do not match the pattern or rates of increase derived using remote sensing approaches [*Giroto et al.*, 2014].

1.3 Guiding hypotheses and project objectives

The work presented in this dissertation is guided by the following hypotheses. The sensitivity of mountain watersheds to warming and snowpack loss is controlled by (1) differences in mountain watershed elevation distributions and (2) variability in the regional rates of increase in snow water equivalent with elevation. Furthermore, (3) the diversity of mountain watershed elevation distributions and rates of snowpack increase with elevation drive the observed variability in mountain snowpack losses.

Chapter 2 presents an initial test of hypotheses 1, 2, and 3. To test these hypotheses I developed a framework characterizing mountain watershed elevation distributions and how snow water equivalent (SWE) changes with elevation. This work focused on characterizing the relationship between peak SWE and elevation because peak SWE reveals the maximum seasonal water content of the snowpack. The relationship between peak SWE and elevation was evaluated using a spatially distributed product at a resolution of 1 km². The elevation- and climate-based framework was then used to simulate a population of mountain watershed elevation distributions, warming driven changes to the peak SWE-elevation relationship, and to estimate individual watershed snowpack losses under a warmer climate. Results from these simulations were used to generate statistical models to evaluate which parameters of an elevation distribution are most important in explaining simulated snowpack losses.

Chapter 3 builds on this theoretical framework and further tests hypotheses 1, 2, and 3 by applying the frameworks developed in chapter 2 to a large number of real watersheds with varying relations between peak SWE and elevation. This chapter explores which Rocky Mountain ecoregions and catchments within are the most sensitive to warming, and how the characteristics of their peak SWE-elevation relationships and watershed elevation distributions control this sensitivity. This chapter also quantifies how variable snowpack losses are within a given ecoregion and whether or not sensitive/resilient watersheds exhibit spatial clustering.

Chapter 4 extends the work of chapters 2 and 3 by utilizing light detection and ranging (LiDAR) derived snow depths from five diverse mountainous Critical Zone Observatories to evaluate elevation- and vegetation-based controls on snow depths. In

particular, this chapter addresses a key assumption made in the first two chapters. The assumption applied in the theoretical framework developed in chapters 2 and 3 is that a watershed's elevation distribution is an accurate indicator of where the majority of its snowpack is stored. While this central tenant has precedence and is supported by theory and observations from instrumental stations, the low density of meteorological stations in high relief topography has made a robust test of this idea effectively impossible. The availability of LiDAR-derived snow depths from a diverse range of hydroclimatic and topographic settings provides a spatially extensive and reliable data set for testing this idea. Analyses presented in the final chapter supports the work of chapters 2 and 3 and evaluates the importance of elevation, aspect and vegetation in controlling the spatial distribution of snowpack.

1.4 Dissertation Structure

This dissertation is composed of three stand-alone papers. They are the fundamental contributions of this work and compose chapters 2, 3, and 4.

1.5 Referemces

Abatzoglou, J. T. (2011), Influence of the PNA on declining mountain snowpack in the Western United States, *International Journal of Climatology*, 31(8), 1135-1142.

Bales, R. C., N. P. Molotch, T. H. Painter, M. D. Dettinger, R. Rice, and J. Dozier (2006), Mountain hydrology of the western United States, *Water Resources Research*, 42(8), 13.

Barnett, T. P., et al. (2008), Human-induced changes in the hydrology of the western United States, *Science*, 319(5866), 1080-1083.

- Giroto, M., G. Cortes, S. A. Margulis, and M. Durand (2014), Examining spatial and temporal variability in snow water equivalent using a 27 year reanalysis: Kern River watershed, Sierra Nevada, *Water Resources Research*, 50(8), 6713-6734.
- Hamlet, A. F., P. W. Mote, M. P. Clark, and D. P. Lettenmaier (2005), Effects of temperature and precipitation variability on snowpack trends in the western United States, *Journal of Climate*, 18(21), 4545-4561.
- Houze, R. A. (2012), OROGRAPHIC EFFECTS ON PRECIPITATING CLOUDS, *Reviews of Geophysics*, 50, 47.
- Kirchner, P. B., R. C. Bales, N. P. Molotch, J. Flanagan, and Q. Guo (2014), LiDAR measurement of seasonal snow accumulation along an elevation gradient in the southern Sierra Nevada, California, *Hydrology and Earth System Sciences*, 18(10), 4261-4275.
- Luce, C. H., and Z. A. Holden (2009), Declining annual streamflow distributions in the Pacific Northwest United States, 1948-2006, *Geophysical Research Letters*, 36, 6.
- Luce, C. H., J. T. Abatzoglou, and Z. A. Holden (2013), The Missing Mountain Water: Slower Westerlies Decrease Orographic Enhancement in the Pacific Northwest USA, *Science*, 342(6164), 1360-1364.
- Mote, P. W., A. F. Hamlet, M. P. Clark, and D. P. Lettenmaier (2005), Declining mountain snowpack in western north America, *Bulletin of the American Meteorological Society*, 86(1), 39-+.

- Pederson, G. T., J. L. Betancourt, and G. J. McCabe (2013), Regional patterns and proximal causes of the recent snowpack decline in the Rocky Mountains, US, *Geophysical Research Letters*, 40(9), 1811-1816.
- Pederson, G. T., S. T. Gray, T. Ault, W. Marsh, D. B. Fagre, A. G. Bunn, C. A. Woodhouse, and L. J. Graumlich (2011a), Climatic Controls on the Snowmelt Hydrology of the Northern Rocky Mountains, *Journal of Climate*, 24(6), 1666-1687.
- Pederson, G. T., S. T. Gray, C. A. Woodhouse, J. L. Betancourt, D. B. Fagre, J. S. Littell, E. Watson, B. H. Luckman, and L. J. Graumlich (2011b), The Unusual Nature of Recent Snowpack Declines in the North American Cordillera, *Science*, 333(6040), 332-335.
- Roe, G. H. (2005), Orographic precipitation, in *Annual Review of Earth and Planetary Sciences*, edited, pp. 645-671, Annual Reviews, Palo Alto.
- Stewart, I. T. (2009), Changes in snowpack and snowmelt runoff for key mountain regions, *Hydrological Processes*, 23(1), 78-94.
- Stewart, I. T., D. R. Cayan, and M. D. Dettinger (2005), Changes toward earlier streamflow timing across western North America, *Journal of Climate*, 18(8), 1136-1155.

Chapter 2: A simple framework for assessing the sensitivity of mountain watersheds to warming-driven snowpack loss

This chapter is published in Geophysical Research Letters and is reprinted here with permission of John Wiley and Sons under license number 3634450689209, issued on May 22, 2015.

2.1 Abstract

The common observation that snowpack increases with elevation suggests that a catchment's elevation distribution should be a robust indicator of its potential to store snow and its sensitivity to snowpack loss. To capture a wide range of potential elevation-based responses, we used Monte Carlo methods to simulate 20,000 watershed elevation distributions. We applied a simple function relating warming, elevation, and snowpack to explore snowpack losses from the simulated elevation distributions. Regression analyses demonstrate that snowpack loss is best described by three parameters that identify the central tendency, variance, and shape of each catchment's elevation distribution. Equal amounts of snowpack loss can occur even when catchments are centered within different elevation zones; this stresses the value of also measuring the variance and shape of elevation distributions. Responses of the simulated elevation distributions to warming are nonlinear and emphasize that the sensitivity of mountain forests to snowpack loss will likely be watershed dependent.

2.2 Introduction

Throughout the world, communities living in dry low-elevation valleys depend on water from high-elevation snowpack. The timing and amount of water release from snowpack sets the pace and potential of human activities such as irrigation, power generation, and availability of municipal water supply [Clark, 2010]. Recent studies have documented a reduction in the proportion of precipitation falling as snow [Knowles *et al.*, 2006], widespread decreases in snow water equivalent (SWE) [Mote *et al.*, 2005], and earlier snowmelt from mountain regions [Stewart, 2009]. Many of these changes are linked to increases in the elevation of the freezing level [Abatzoglou, 2011] and accelerated warming at high elevations [Rangwala and Miller, 2012]. Warming and changes in snow accumulation and melt have important implications for the spatial distribution of plant communities [Ford *et al.*, 2013], forest greenness [Trujillo *et al.*, 2012], growth rates of high-elevation tree species [Salzer *et al.*, 2009], and annual patterns of carbon and nitrogen cycling [Brooks *et al.*, 2011].

Tools for estimating snow accumulation and melt operate at different spatial and temporal scales. Small-scale models, which retain the detailed physics of the energy balance, are useful for evaluating how changes in local-scale energy budgets affect snowpack dynamics. For example, Kumar *et al.* [2012] used the SNOBAL model [Marks *et al.*, 1998] to locally demonstrate how less frequent but more intense storm events could increase the maximum seasonal SWE. Coarser, large-scale energy balance approaches have been used to evaluate temporal trends in SWE for the western U.S. [Mote *et al.*, 2005]. Remote sensing observations (satellite and airborne lidar) of snow cover depth and extent, coupled with in situ measurement of snow density offer improvements for

estimating SWE over tens to hundreds of square kilometers [Barrett, 2003; Giroto *et al.*, 2014; Harpold *et al.*, 2014; Kirchner *et al.*, 2014; Rice *et al.*, 2011].

Field studies, remote sensing, and modeling efforts all demonstrate that snow depth and water equivalent typically increase with elevation [e.g., Abatzoglou, 2011; Bradley *et al.*, 2009; Clark *et al.*, 2011; Ford *et al.*, 2013; Giroto *et al.*, 2014; Kirchner *et al.*, 2014; Rice *et al.*, 2011]. Given this consistent relationship between SWE and elevation, and the expectation of global warming in the range of 1.7 to 4.8°C by 2081–2100 [Intergovernmental Panel on Climate Change, 2014], we argue that a watershed’s elevation distribution should strongly influence its response to warming-driven snowpack loss. Because catchments draining mountainous terrain exhibit a wide variety of elevation distributions, we expect that snowpack losses will vary from catchment to catchment, generating a complex pattern at the landscape scale.

Here we present a theoretical framework and simulation results designed to quantify the elevation-based sensitivity of mountain watersheds to warming-driven snowpack loss. We identify the metrics important in characterizing a watershed’s elevation-based susceptibility to snowpack loss and link our simulation results to landscape sensitivities.

2.3 Methods & Experimental Design

2.3.1 Elevation-based Framework

2.3.1.1 Elevation Characteristics of Northern Rocky Mountain Watersheds

We characterized the elevation distributions of 3175 mountain watersheds in the U.S. northern Rocky Mountains (Figure S1 in the supporting information), a region

covering large portions of central Idaho and western Montana and Wyoming. Variations in the lithology and the tectonic and geomorphic histories of the area produce a diverse set of watershed elevation distributions ideal for testing the sensitivity of mountain catchments to snowpack loss. The characterized watersheds range in size from 18 km² to 850 km², with a mean area of 86 km² and a mean elevation of 1900 m. We used 30m resolution data from the National Elevation Dataset [Gesch *et al.*, 2002] for our elevation-based analyses.

Several common probability distributions were fit to the northern Rocky Mountain elevation distributions. The goodness of fit for each distribution was determined using the Bayesian Information Criterion [Claeskens and Hjort, 2008]. More than 88% (2804) of the surveyed elevation distributions were best described by the generalized extreme value (GEV) distribution [Kotz and Nadarajah, 2000]. The GEV distribution is convenient because its probability density function (PDF, equation (1)) can be used to model a variety of distribution types.

$$f(x|k, \mu, \sigma) = \begin{cases} \left(\frac{1}{\sigma}\right) \exp\left(-\left(1 + k\frac{(x - \mu)}{\sigma}\right)^{\frac{1}{k}}\right) \left(\left(1 + k\frac{(x - \mu)}{\sigma}\right)^{-1 - \frac{1}{k}}\right), & k \neq 0 \\ \left(\frac{1}{\sigma}\right) \exp\left(-\exp\left(-\frac{(x - \mu)}{\sigma}\right) - \left(\frac{(x - \mu)}{\sigma}\right)\right), & k = 0 \end{cases} \quad (1)$$

In the context of this study, the location parameter (μ) determines the elevation where the distribution is centered (Figure 1a); similar metrics of location include the mean, median, or mode. The scale parameter (σ) determines the variability in the

distribution by “compacting” or “stretching” it (Figure 1b); similar metrics for scale include variance or standard deviation. The shape parameter (k) describes the asymmetry and tail behavior of the distribution and is analogous to descriptors such as skewness and kurtosis (Figure 1c). For the natural watershed elevation distributions, no correlation was observed between the GEV parameters location and scale or location and shape (Figure S2) or between any of the GEV parameters and watershed drainage area (Figure S3). A correlation was observed between the scale and shape parameters; a regression was developed (Figure S4) and used in the simulation of elevation distributions.

2.3.1.2 Monte Carlo Simulation of Mountain Watershed Elevation Distributions

Monte Carlo methods were used to simulate 20,000 elevation distributions that cover a wide range of potential watershed elevation distribution types. The distributions were randomly generated using the GEV PDF (equation (1)) for a given set of location, scale, and shape parameters selected at random from values observed in the U.S. northern Rocky Mountains. Because shape and scale are correlated in natural watersheds (Figure S4), we maintained the observed covariance structure by selecting a shape parameter for each randomly drawn scale parameter in the regression equation (Figure S4). The shape-scale correlation of simulated elevation distributions ($r = -0.566$) closely matched that of real-world elevation distributions ($r = -0.574$).

Using a Monte Carlo approach and the GEV distribution to generate synthetic watershed elevation distributions is advantageous for several reasons. First, the synthetic distributions reflect the characteristics of the natural landscape but overcome potential spatial autocorrelation issues. Second, our simulated distributions filled in gaps in our sample of natural watersheds, allowing us to explore elevation distributions not common

in our sample from the U.S. northern Rocky Mountains. Third, the GEV distribution is defined by three parameters and provides a parsimonious system for distinguishing different distribution types.

2.3.2 Current and Future Peak SWE-Elevation Relationships

2.3.2.1 Peak SWE-elevation Relationship

The peak SWE-elevation relationship defines how average annual peak SWE varies with elevation. We chose peak SWE as a metric of focus because it represents the maximum water accumulation in a snowpack on an annual basis and is important for understanding current snow storage patterns and predicting future ones. We used 1km² gridded estimates of SWE from the National Weather Service's Snow Data Assimilation System (SNODAS) [Barrett, 2003; Carroll *et al.*, 2003], a national-scale snow mass and energy model based on SNTHERM.89 [Jordan, 1991], to estimate the average peak SWE-elevation relationship for water years 2004–2012. A raster of peak SWE was matched to elevation grids of the same resolution, enabling the calculation of mean peak SWE for each elevation. Although the 2004–2012 water years represent a relatively short time period, they capture a wide range of climatic variability. The 1 April SWE during the 2004–2012 water years ranged from 50 to 130% of the 1981–2010 median 1 April SWE based on SNOTEL records located in the same region. Thus, the SNODAS records represent a range of potential snowpack conditions. However, the number of SNODAS pixels at the highest elevations (>3800 m) within the region of our SWE-based analysis is limited and may not be representative.

We focused on a 36,000 km² subregion central to the overall study area to estimate the peak SWE-elevation relationship (Figure S1). The selected region covers a wide range of climate types from maritime influenced to drier continental areas and broadly represents the region of our elevation-based analyses. We evaluated the peak SWE-elevation relationship for other regions within the U.S. northern Rocky Mountains and found that the overall patterns were broadly consistent; peak SWE-elevation relationships have a sigmoidal shape. For all of the surveyed subregions, peak SWE was smallest at low elevations. Near ~1000m, peak SWE increased rapidly, and at higher elevations, the rate of increase of peak SWE was near zero. While these basic patterns were consistent across the region, maximum peak SWE values and maximum rates of increase in peak SWE can vary with location. The sigmoidal function presented below should be calibrated using local peak SWE-elevation relationships when exact estimates of SWE loss are needed. Because our focus is on developing an elevation-based framework, we chose to use a peak SWE-elevation relationship from a subregion that is broadly representative of the larger region (Figure S1).

2.3.2.2 Modeling the Current Peak SWE-Elevation Relationship

We used the Richard's growth function, a sigmoidal function, to empirically describe the relationship between peak SWE and elevation (Figure 2a) and to predict future warming-driven modifications (Figure 2b). Peak snow water equivalent (SWE_{pk}) for a given elevation, $elev_i$ (where i ranges from the minimum to maximum elevation) is described using equation (2):

$$SWE_{pk}(elev_i) = A \left[1 + v \exp \left\{ 1 + v + \frac{M}{A} (1 + v)^{1 + \frac{1}{v}} (\lambda - elev_i) \right\} \right]^{-1/v} \quad (2)$$

where A sets the maximum peak SWE, M is the maximum slope of the curve, λ is a location parameter, and v influences the shape of the function (the location and shape parameters for equation (2) are not related to the location and shape parameter for the GEV PDF, equation (1)). The empirically derived parameters of the Richard's equation are convenient because they set a maximum peak SWE value (A) and curve slope (M). The location parameter (λ) can be used to assess the elevation at which SWE exhibits the most rapid increase. These parameters can easily be adjusted to model different observed relationships between peak SWE and elevation and could be used to compare peak SWE-elevation relationships across different mountain regions.

2.3.2.3 Modeling Potential Future Peak SWE-Elevation Relationships

To model how warming could affect peak SWE, we applied a typical lapse rate of -0.65°C per 100m to shift the location parameter (λ) in equation (2). Shifting λ raises the elevation zone where rapid increases in peak SWE occur, reduces peak SWE in a systematic manner across all elevations, and is analogous to a warming-driven increase in the elevation of the snowline (Figure 2b). The greatest SWE reductions occur at low and middle elevations where temperatures would more frequently be above 0°C. Increases in precipitation at high elevations may partially offset the impacts of warming [*Giroto et al.*, 2014; *López-Moreno et al.*, 2013]. Our method for modeling the peak SWE-elevation relationship can be modified for anticipated changes in precipitation by modifying parameter A in equation (2) and is flexible enough to accommodate a variety of warming and elevation-dependent changes to the peak SWE-elevation relationship.

2.3.3 Areal-Average Peak SWE Estimation for Simulated Elevation Distributions

Areal-average peak SWE for each of the 20,000 simulated elevation distributions was determined using the following formula:

$$SWE = \sum_{i=1}^I SWE_{(i)} (a_i) \quad (3)$$

where SWE_i is the peak SWE value at elevation i and a_i is the fraction of total watershed area at elevation i (i ranges from the minimum to maximum watershed elevation (I)). SWE_i for each fraction of area (a_i) was determined using equation (2). Equation (3) was used for determining the current (+ 0°C) and potential future (+1° to +5°C) watershed areal-average peak SWE and is described in Section 2.3.6.

2.3.4 Current and Future Snowline Elevations

In landscapes experiencing seasonal snow cover, it is useful to evaluate the duration of snow cover as a function of elevation to understand elevation-dependent streamflow patterns [Tennant *et al.*, 2015], wintertime biogeochemical fluxes [Brooks *et al.*, 2011], and ecological sensitivities of mountain communities [Bales *et al.*, 2006]. Closely linked to the duration of snow cover is the idea of a snowline elevation, which can be useful for characterizing catchment sensitivity to warming-driven hydrologic change. However, a robust definition of the snowline is difficult because of short-term (storm-driven) and long-term (interannual climate-driven) variability in the freezing elevation. Here we define the snowline as the elevation where there is a 50% probability of encountering $SWE > 0$ on an annual basis; elevations above this value would, on average, have snow cover at least 6 months of each year. This snowline definition has

precedence [*Hantel and Maurer, 2011*] and designates elevations that have consistent wintertime snow cover from those that do not; other snowline definitions may be appropriate for different sensitivity assessments. We identified the average snowline elevation for water years 2004–2012 by calculating the probability of SWE>0 for all elevations using SNODAS SWE and elevation grids of the same resolution. For the region of climatic characterization (Figure S1), the current snowline elevation is ~1980 m. Shifting the snowline upward using a typical lapse rate results in future snowline elevations of 2134, 2288, 2442, 2595, and 2749m (for + 1°C, 2°C, 3°C, 4°C, and 5°C, respectively).

2.3.5 Extent of Evergreen Forest

To link our rising snowline and snowpack loss simulations (section 2.3.2) to a landscape sensitivity, we defined the lower and upper extents of evergreen forest within the region of our peak SWE-elevation characterization. We focused on evergreen forests because of their sensitivity to changes in temperature and water availability [*Salzer et al., 2009; Trujillo et al., 2012*] and their importance to the hydrologic cycle [*Goulden and Bales, 2014*]. The lower and upper extents of evergreen forest were identified using 30m resolution elevation data and land cover data from the 2011 National Landcover Database (NLD) [*Jin et al., 2013*]. We binned the elevations within the region used for climatic characterization (Figure S1) into 10 bins. The corresponding NLD cells that fell within each elevation bin were extracted and used to calculate the percentage that each land cover type composes within each respective elevation bin (Figure S5). The extent of evergreen forest is defined by the elevations of the lower and upper bins where evergreen forest composed the greatest percentage of land cover (Table S1). We evaluated a variety

of bin sizes and found that increasing the number of bins had minimal effect on the elevations where evergreen forest was identified as the dominant land cover type.

2.3.6 Snowpack Sensitivity Metrics

To evaluate the sensitivity of the simulated watershed elevation distributions to warming-driven snowpack loss, we recalculated watershed areal-average peak SWE for a range of increased temperatures (+1°C to +5°C) using equations (2) and (3). Parameters in equation (2) were adjusted for each warming scenario as described above (section 2.2.3 and Figure 2b). Peak SWE loss for a given catchment was determined by differencing the current (+0°C) areal-average peak SWE from a modeled future value (e.g., +5°C). Calculating the area above the snowline (AAS) reveals the percentage of the watershed that maintains snow cover for at least 6 months. We calculated the percent loss in AAS for each warming increment. We report percent loss instead of area loss because the drainage areas of all the simulated elevation distributions are held constant (section 2.3.1.2).

2.4 Discussion of Simulation Results

2.4.1 Peak SWE Loss

Peak SWE losses are controlled by the location and scale parameters of the GEV elevation distributions. The pattern of peak SWE loss is nonlinear across the simulated elevation distributions and forms a parabolic pattern with respect to the location parameter (Figure 3a). The location parameter is the primary control on peak SWE loss while the scale parameter is a lesser, though consistent indicator of peak SWE loss. The greatest losses occur in watersheds with location parameters between 1000 and 2000m

and with scale parameters less than ~300 m. Elevation distributions with higher scale parameters have lower SWE losses even if they are located between 1000 and 2000m (Figure 3a). The role of large scale parameters in reducing peak SWE loss becomes increasingly apparent as warming progresses (Figure 3a, +5°C). For example, at +5°C warming, elevation distributions with scale parameters $\geq 600\text{m}$ have nearly 70mm less peak SWE loss than watersheds with narrow-elevation distributions. These simulation results demonstrate that only watersheds with location parameters $>2000\text{m}$ and a small number of watersheds located between 1000 and 2000m with large-scale parameters ($\geq 500\text{ m}$) are resilient to significant warming. These catchments will serve as persistent water resources and be the most capable of sustaining ecosystems which depend on snow-dominated hydrology.

We performed multivariate regression analysis to quantify how elevation distributions influence the patterns of peak SWE loss (Table S1). For +1°C to +5°C, we used the Bayesian Information Criterion (BIC) to select the most parsimonious regression from all model subsets of the GEV parameters up to third-order GEV interactions (e.g., location^3 or $\text{location} \times \text{shape}^2$; all regressions had $R^2 = 0.99$). The GEV elevation parameters that explained the most variance in peak SWE loss were location and scale. Of these regression parameters, location^2 explained the majority of the variance in peak SWE loss across all warming scenarios. The variance explained by location^2 and location^3 increases with warming (Figure S6) and emphasizes the highly nonlinear, elevation-dependent response of peak SWE loss (Figure 3a). The GEV shape parameter was selected in each regression by BIC (Table S2), however, it explained $<0.5\%$ of the variance in peak SWE loss across all warming scenarios.

The peak SWE loss results presented here demonstrate that multiparameter descriptions of elevation distributions will prove useful in estimating catchment sensitivity to snowpack loss. Our simulation results are consistent with *Pederson et al.* [2013] and *Stewart* [2009], showing that middle elevations are the most sensitive to warming-driven snowpack loss. We add to these results by demonstrating and quantifying the potential nonlinear, elevation-dependent response of mountain catchments to SWE loss (Figure 3a).

2.4.2 Area Above Snowline (AAS) Loss

Patterns of area above snowline (AAS) loss are strongly influenced by the location of an elevation distribution relative to the elevation of the snowline. The greatest losses occur for watersheds centered just below the snowline elevation (Figure 3b). The scale parameter also plays an important role in regulating AAS loss. For example, in the +1°C warming scenario, AAS loss for elevation distributions centered just below the snowline can be as great as 100% for those with small variance in elevation (scale <200 m), whereas those with larger variance (scale >500 m) experience AAS loss of less than 10%.

Warming causes the patterns of AAS loss to shift in complex ways. For example, the elevation zone where the greatest AAS losses are focused expands with warmer temperatures and the value of minimum AAS loss within this zone increases (Figure 3c). At +5°C, only a small number of watershed elevation distributions have not experienced significant AAS loss. These catchments have location parameters greater than ~2800m and scale parameters less than 300 m. These AAS loss simulations reinforce that

multiparameter descriptions of elevation distributions are crucial to characterizing catchment sensitivity to snowpack loss.

2.4.3 Potential Model Limitations

We expect our elevation-based framework to be widely applicable, but it may be ill suited for some locations or situations. The GEV PDF produces distributions that tend to be smoother than natural ones. Thus, catchments with strong asymmetry or bimodality in their elevation distributions may not be as well represented. The peak SWE-elevation relationship used in our simulations involved large-scale spatial averaging, collapsing the many nonuniform physical processes (e.g., sublimation, wind redistribution, ablation, and avalanching) controlling the spatial distribution of SWE into a single, elevation-dependent metric. A central assumption is that the processes controlling the energy and mass balance over the years that are summarized by the peak SWE-elevation relationship can be shifted to represent future ones (e.g., Figure 2b). Because our framework is centered on fundamental principles like temperature lapse rate and orographic precipitation enhancement (see review in *Roe* [2005]), we assert that it provides adequate first-order estimates of watershed sensitivity to snowpack loss.

Our framework is intended to be applied at the intermediate watershed scale (50 km² to 1000 km²) because SWE amounts at these scales are dominantly influenced by the freezing level elevation, snowfall amounts, and available melt energy [*Abatzoglou*, 2011; *Bradley et al.*, 2009; *Clark et al.*, 2011; *Elder et al.*, 1998]. Variations in SWE at the hillslope to small-catchment (~0.5 to 10 km²) scales caused by drifting [*Luce et al.*, 1998], interception by vegetation [*Varhola et al.*, 2010], sublimation [*Gustafson et al.*, 2010], and avalanching [*Clark et al.*, 2011] are lumped in our functional relationship between peak

SWE and elevation (Figure 2). Although these processes may govern SWE variability at smaller scales or when relief is less than ~200m [Clark *et al.*, 2011], we expect that at intermediate watershed scales and above, the model will perform well.

The results from our simulations are theoretical, and an important future step is to evaluate how well this characterization matches observed snowpack loss on the landscape. To rigorously evaluate our framework, long-term estimates of peak SWE that span large-elevation gradients from a number of different catchments having experienced a warming trend are needed. Lidar snow-on, snow-off depth estimates [Harpold *et al.*, 2014] coupled with spatially extensive density measurements may soon provide data sets that allow a rigorous test of our framework.

2.4.4 Examples of Model Application

2.4.4.1 Watershed Sensitivity Analyses

Our results indicate that catchment sensitivity to warming depends on the elevation distribution of a watershed and which consequences are of greatest concern. For example, following +5°C of warming, the greatest peak SWE losses occur in watersheds centered at 1500 m; however, the greatest AAS losses occur around 2250 m. Therefore, catchment sensitivity needs to be clearly defined for particular management needs or research questions. The framework and regression models presented here could be used to estimate the amount of peak SWE or AAS loss for a given amount of warming to identify which watersheds are most capable of sustaining snow-based water resources. Our framework is easily applied to categorize sensitive versus resilient watersheds or to prioritize the rehabilitation of habitat for snowmelt-dependent aquatic species. Our

snowpack loss simulations offer a probability space of potential watershed responses to warming and could be used to focus the efforts of physically based models to identify mechanistic controls on watersheds that are expected to be either sensitive or resilient to warming.

2.4.4.2 Sensitivity of Evergreen Forests to Peak SWE and AAS Loss

We found that evergreen forests are the dominant land cover type within the sensitive middle elevations (1000–2000 m; Figure S5). Furthermore, the peak areal extent of evergreen forest cover was located between 2000 and 2400m (Table S1); our AAS and peak SWE loss simulations (Figures 3c and 3d) indicate that these elevations will likely experience decreases in snow cover amount and duration. *Trujillo et al.* [2012] report that forest greenness, an indicator of forest health, is strongly correlated with peak SWE, and predict that middle-elevation mountain forests are highly sensitive to temperature increases. Our results confirm that middle elevations are highly sensitive to peak SWE loss but show that different watershed elevation distributions will likely exhibit different peak SWE losses, even if the mean catchment elevation (location) is held constant. Thus, some forested basins may be more sensitive or more resilient than expected if sensitivity were evaluated on their mean elevations alone. Further, because snow cover duration influences wintertime heterotrophic activity [*Brooks et al.*, 2011], our AAS loss model could improve predictions of which catchments are most likely to experience decreased carbon (C) and nitrogen (N) cycling occurring during winter months (Figure 3d).

2.5 Conclusions

The expectation of future warming and strong anthropogenic and ecosystem ties to melt-supplied water sources drive the need to map the potential trajectories of snowpack

loss in sensitive mountain catchments. The framework presented here provides a parsimonious method for characterizing the potential sensitivity of individual mountain catchments to snowpack loss.

2.6 Acknowledgements

The elevation data used for this paper are available from the National Elevation Dataset (<http://ned.usgs.gov/>). The Snow Data Assimilation System (SNODAS) snow water equivalent (SWE) data can be obtained at the National Snow and Ice Data Center's Polaris tool (<http://nsidc.org/data/polaris/>). All MATLAB and R scripts used in the presented analyses are available upon request from the lead author. The work was supported by a NASA Idaho Space Grant Consortium Fellowship and by NSF awards EPS-0814387 and EPS-1006968 from the Idaho NSF EPSCoR Program. This work benefited from conversations and feedback from Noah Molotch, Paul Brooks, Kathleen Lohse, and John Welhan. We thank Keith Musselman and an anonymous reviewer.

2.7 Figures and Tables

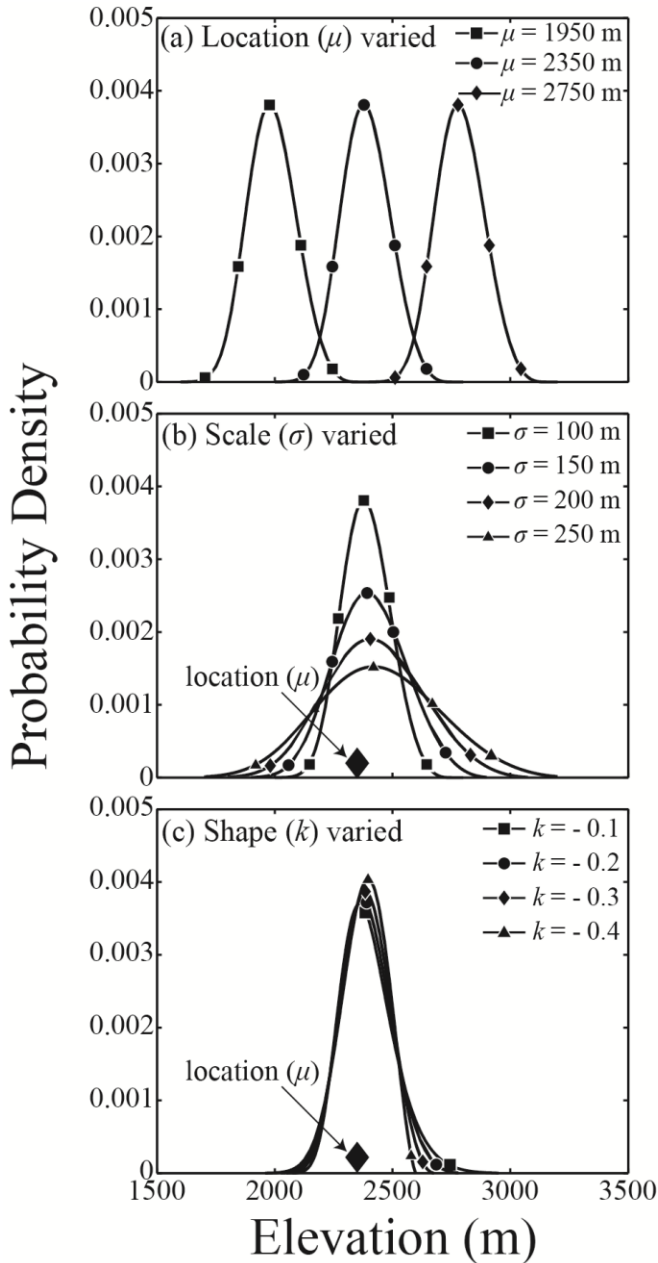


Figure 2.1. Examples of the influence of (a) location (μ), (b) scale (σ), and (c) shape (k) parameters on a series of generalized extreme value probability distributions for watershed elevations. In each plot, only the labeled variable is changed. The diamonds positioned on the x axis in b and c show the value of the location parameter for all distributions.

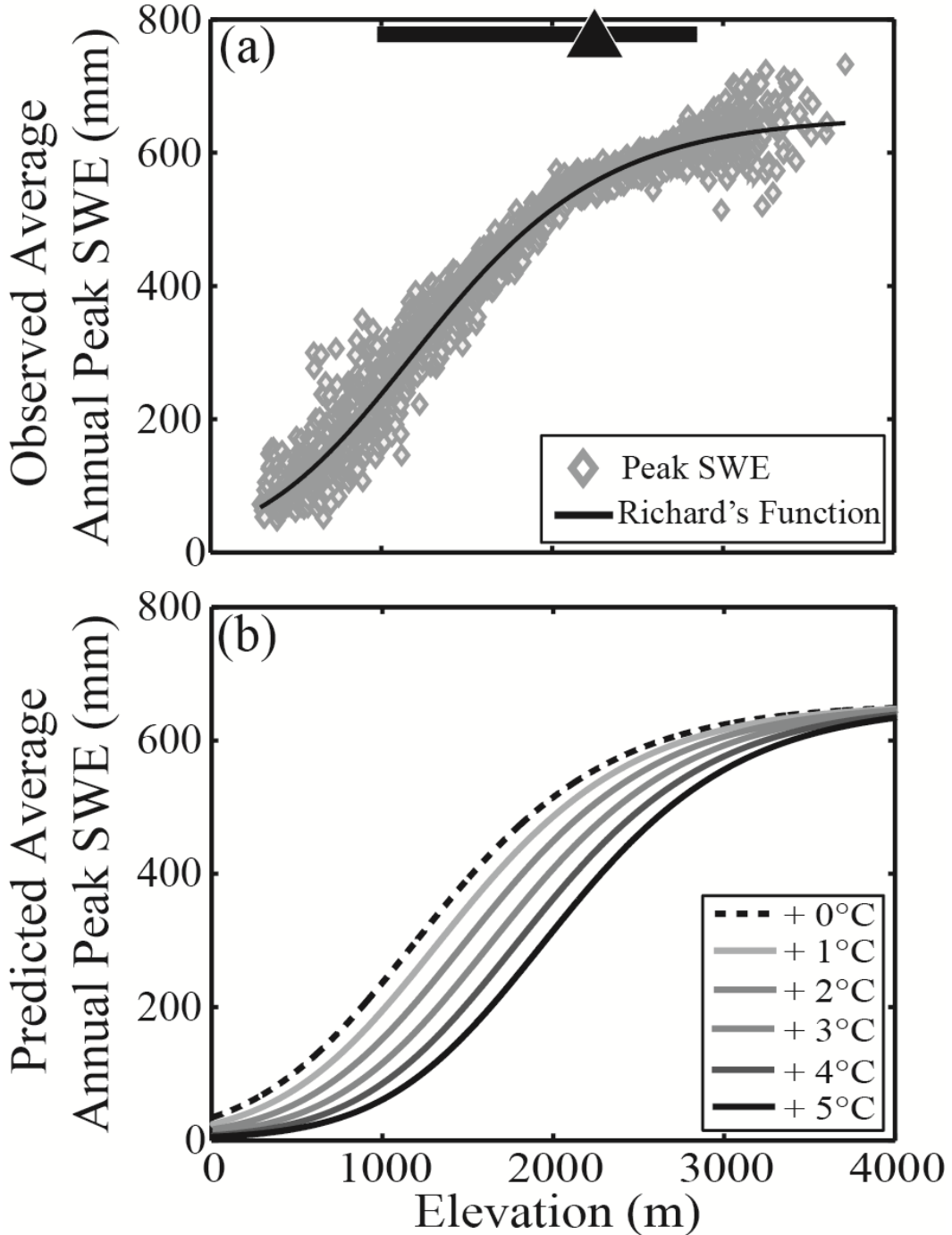


Figure 2.2. (a) Peak snow water equivalent (SWE) as a function of elevation with the best-fit Richard's function (thin black line). Grey diamonds are data from the Snow Data Assimilation System for the region of peak SWE characterization (Figure S1), the thick horizontal line in (a) shows the range of elevations (990 – 2776 m) where evergreen forest are the dominant land cover type and the triangle shows the midpoint (2240 m) of the elevation bin where evergreen forests reach their maximum percent cover. (b) Current (+0°C, dashed black line) and expected future changes (darkening solid lines) to the relationship between peak SWE and elevation.

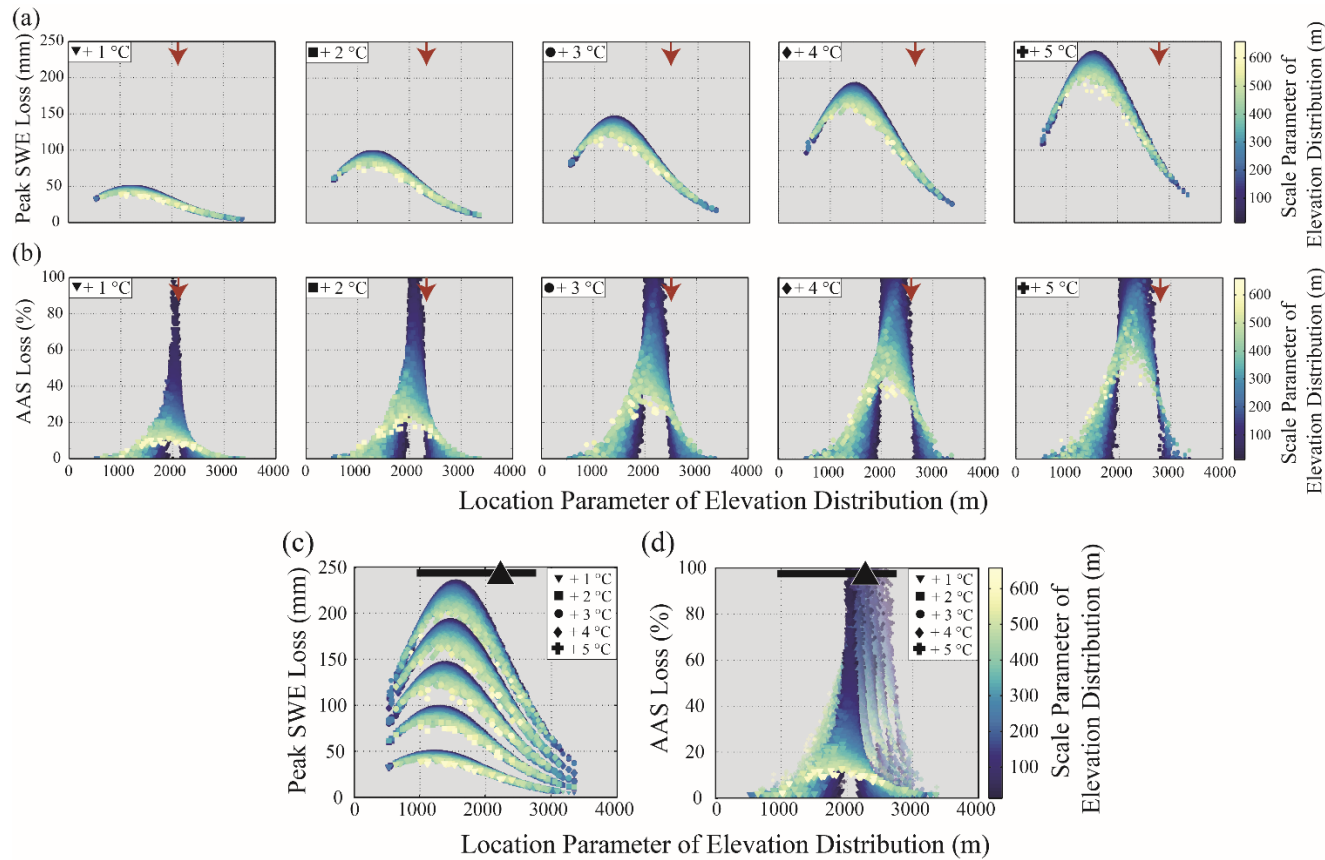


Figure 2.3. Catchment-wide predictions of peak SWE loss (a and c) and loss of area above snowline (AAS; b and d) given +1° to +5°C warming. Each point represents a Monte Carlo simulated watershed elevation distribution, the location parameter (μ) describes the central tendency and the scale parameter (σ) the variance of the individual distributions. The arrows in (a) and (b) indicate the snowline elevation for each degree of warming. Simulations emphasize that catchment sensitivity varies with peak SWE loss or AAS loss, and depends on the location (μ) and scale (σ) parameters of each elevation distribution and the degree of warming. Horizontal bars in (c) and (d) denote the range of elevations (990 – 2776 m) where evergreen forest are currently the dominant land cover and the triangles show the midpoint (2240 m) of the elevation bin where evergreen forests reach their maximum percent cover.

2.8 References

- Abatzoglou, J.T. (2011), Influence of the PNA on declining mountain snowpack in the Western United States, *Int. J. of Climatol.*, *31*, 1135-1142. doi: 10.1002/joc.2137
- Bales, R. C., N. P. Molotch, T. H. Painter, M. D. Dettinger, R. Rice, and J. Dozier (2006), Mountain hydrology of the western United States, *Water Resour. Res.*, *42*, W08432, doi: 10.1029/2005wr004387.
- Barrett, A.P. (2003), National operational hydrologic remote sensing center snow data assimilation system (SNODAS) products at NSIDC, *NSIDC Spec. Rep. 11.*, 19 pp., Natl. Snow and Ice Data Cent., Boulder, Colo.
- Bradley, R. S., F. T. Keimig, H. F. Diaz, and D. R. Hardy (2009), Recent changes in freezing level heights in the Tropics with implications for the deglaciation of high mountain regions, *Geophys. Res. Lett.*, *36*, L17701, doi: 10.1029/2009gl037712.
- Brooks, P. D., P. Grogan, P. H. Templer, P. Groffman, M. G. Öquist, and J. Schimel (2011), Carbon and nitrogen cycling in snow-covered environments, *Geog. Compass*, *5*(9), 682-699, doi: 10.1111/j.1749-8198.2011.00420.x.
- Carroll, T., D. Cline, G. Fall, L. Li, and A. Nilsson (2003), Seasonal snow cover monitoring and modeling for the coterminous United States, paper presented at EGS-AGU-EUG Joint Assembly, Nice, France, p. 1396.
- Claeskens, G., and N.L. Hjort (2008), Model selection and model averaging (Cambridge Series in Statistical and Probabilistic Mathematics), Cambridge University Press, Cambridge, New York.

- Clark, G. M. (2010), Changes in Patterns of Streamflow From Unregulated Watersheds in Idaho, Western Wyoming, and Northern Nevada, *J. Am. Water Resour. Assoc.*, 46(3), 486 - 497, doi: 10.1111/j.1752-1688.2009.00416.x.
- Clark, M. P., J. Hendrikx, A. G. Slater, D. Kavetski, B. Anderson, N. J. Cullen, T. Kerr, E. O. Hreinsson, and R. A. Woods (2011), Representing spatial variability of snow water equivalent in hydrologic and land-surface models: A review, *Water Resour. Res.*, 47, W07539, doi: 10.1029/2011wr010745.
- Elder, K., W. Rosenthal, and R. E. Davis (1998), Estimating the spatial distribution of snow water equivalence in a montane watershed, *Hydro. Processes*, 12(10-11), 1793-1808, doi: 10.1002/(SICI)1099-1085(199808/09)12:10/11<1793::AID-HYP695>3.0.CO;2-K.
- Ford, K. R., A. K. Ettinger, J. D. Lundquist, M. S. Raleigh, and J. H. R. Lambers (2013), Spatial heterogeneity in ecologically important climate variables at coarse and fine scales in a high-snow mountain landscape, *Plos One*, 8(6), e65008, doi: 10.1371/journal.pone.0065008.
- Giroto, M., G. Cortes, S. A. Margulis, and M. Durand (2014), Examining spatial and temporal variability in snow water equivalent using a 27 year reanalysis: Kern River watershed, Sierra Nevada, *Water Resour. Res.*, 50(8), 6713-6734, doi: 10.1002/2014wr015346.
- Gesch, D., M. Oimoen, S. Greenlee, C. Nelson, M. Steuck, and D. Tyler (2002), The national elevation dataset, *Photogram. Eng. and Remote Sens.*, 68(1), 5-32.

- Goulden, M. L., and R. C. Bales (2014), Mountain runoff vulnerability to increased evapotranspiration with vegetation expansion, *Proc. Natl. Acad. of Sci.*, *111*(39), 14071-14075, doi:10.1073/pnas.1319316111.
- Gustafson, J. R., P. D. Brooks, N. P. Molotch, and W. C. Veatch (2010), Estimating snow sublimation using natural chemical and isotopic tracers across a gradient of solar radiation, *Water Resour. Res.*, *46*, W12511, doi: 10.1029/2009wr009060.
- Hantel, M., and C. Maurer (2011), The median winter snowline in the Alps, *Meteorologische Zeitschrift*, *20*(3), 267-276, doi:10.1127/0941-2948/2011/0495.
- Harpold, A. A., et al. (2014), LiDAR-derived snowpack data sets from mixed conifer forests across the Western United States, *Water Resour. Res.*, *50*(3), 2749-2755, doi:10.1002/2013wr013935.
- IPCC, 2014: Summary for Policymakers. In: *Climate Change 2014: Impacts, Adaptation, and Vulnerability. Part A: Global and Sectoral Aspects. Contribution of Working Group II to the Fifth Assessment Report of the Intergovernmental Panel on Climate Change* [Field, C.B., V.R. Barros, D.J. Dokken, K.J. Mach, M.D. Mastrandrea, T.E. Bilir, M. Chatterjee, K.L. Ebi, Y.O. Estrada, R.C. Genova, B. Girma, E.S. Kissel, A.N. Levy, S. MacCracken, P.R. Mastrandrea, and L.L. White (eds.)]. Cambridge University Press, Cambridge, United Kingdom and New York, NY, USA, pp. 1-32.
- Jordan, R. (1991), A one-dimensional temperature model for a snow cover: Technical documentation for SNTHERM. 89, U.S. Army Cold Regions Research and Engineering Laboratory Special Rep., 91-16, pp. 1- 49.
- Kirchner, P., R. Bales, N. Molotch, J. Flanagan, and Q. Guo (2014), LiDAR measurement of seasonal snow accumulation along an elevation gradient in the

- southern Sierra Nevada, California, *Hydrol. Earth Sys. Sci. Disc.*, 18(10), 4261-4275, doi: 10.5194/hess-18-4261-2014.
- Knowles, N., M. D. Dettinger, and D. R. Cayan (2006), Trends in snowfall versus rainfall in the Western United States, *J. Climate*, 19(18), 4545-4559, doi: 10.1175/jcli3850.1.
- Kotz, S. and Nadarajah, S., (2000), Extreme value distributions, Imperial College Press., London, England.
- Kumar, M., R. Wang, and T. E. Link (2012), Effects of more extreme precipitation regimes on maximum seasonal snow water equivalent, *Geophys. Res. Lett.*, 39, L20504, doi: 10.1029/2012gl052972.
- Lopez-Moreno, J. I., J. W. Pomeroy, J. Revuelto, and S. M. Vicente-Serrano (2013), Response of snow processes to climate change: spatial variability in a small basin in the Spanish Pyrenees, *Hydrol. Processes*, 27(18), 2637-2650, doi: 10.1002/hyp.9408.
- Luce, C. H., D. G. Tarboton, and R. R. Cooley (1998), The influence of the spatial distribution of snow on basin-averaged snowmelt, *Hydrol. Processes*, 12(10-11), 1671-1683, doi: 10.1002/(sici)1099-1085(199808/09)12:10/11<1671::aid-hyp688>3.0.co;2-n.
- Marks, D., J. Kimball, D. Tingey, and T. Link (1998), The sensitivity of snowmelt processes to climate conditions and forest cover during rain-on-snow: a case study of the 1996 Pacific Northwest flood, *Hydrol. Processes*, 12(10-11), 1569-1587, doi:10.1002/(sici)1099-1085(199808/09)12:10/11<1569::aid-hyp682>3.3.co;2-c.
- Mote, P.W., Hamlet, A.F., Clark, M.P., D.P. Lettenmaier (2005), Declining mountain snowpack in western north America, *Bull. Am. Meteorol. Soc.*, 86(1), 39 – 49, doi: 10.1175/bams-86-1-39.

- Rangwala, I., and J. R. Miller (2012), Climate change in mountains: a review of elevation-dependent warming and its possible causes, *Climatic Change*, 114(3-4), 527-547, doi: 10.1007/s10584-012-0419-3.
- Roe, G. H. (2005), Orographic precipitation, in *Annual Review of Earth and Planetary Sciences*, edited, pp. 645-671, Annual Reviews, Palo Alto, doi: 10.1146/annurev.earth.33.092203.122541.
- Rice, R., R. C. Bales, T. H. Painter, and J. Dozier (2011), Snow water equivalent along elevation gradients in the Merced and Tuolumne River basins of the Sierra Nevada, *Water Resources Research*, 47, W08515, doi: 10.1029/2010wr009278.
- Salzer, M. W., M. K. Hughes, A. G. Bunn, and K. F. Kipfmueller (2009), Recent unprecedented tree-ring growth in bristlecone pine at the highest elevations and possible causes, *Proc. Natl. Acad. of Sci.*, 106(48), 20348-20353, doi: 10.1073/pnas.0903029106.
- Stewart, I.T. 2009, Changes in snowpack and snowmelt runoff for key mountain regions. *Hydrol. Processes*, 23, 78-94, doi: 10.1002/hyp.7128.
- Tennant, C. J., B. T. Crosby, and S. E. Godsey (2014), Elevation-dependent responses of streamflow to climate warming, *Hydrol. Processes*, doi: 10.1002/hyp.10203.
- Trujillo, E., N. P. Molotch, M. L. Goulden, A. E. Kelly, and R. C. Bales (2012), Elevation-dependent influence of snow accumulation on forest greening, *Nature Geosci.*, 5(10), 705-709, doi: 10.1038/ngeo1571.
- Varhola, A., N. C. Coops, M. Weiler, and R. D. Moore (2010), Forest canopy effects on snow accumulation and ablation: An integrative review of empirical results, *J. Hydrology*, 392(3-4), 219-233, doi: 10.1016/j.jhydrol.2010.08.009.

Chapter 3: The sensitivity of Rocky Mountain ecoregions to snowpack loss

3.1 Abstract

Topographic complexity and climatic variability complicate assessments of how mountain snowpacks will respond to warming. We present a framework to efficiently assess landscape sensitivity to warming-driven snowpack loss from the catchment to ecoregion scale. This framework, founded on observed correlations between snowpack, elevation, and temperature, is tested in 634 watersheds distributed between four diverse Rocky Mountain ecoregions. Warming simulations (+1°C to +4°C) reveal that sensitivity to snowpack loss varies both between and within ecoregions and that losses are non-linear and elevation-dependent at the ecoregion scale. Within an ecoregion, catchment peak SWE losses can be widely variable, ranging from less than 100 mm to more than 400 mm for a +4°C warming scenario. Ecoregions with large areas in mid elevations exhibiting rapid increases in snowpack with elevation are most sensitive to snowpack loss. Warming simulations also indicate a strong, ecoregion-dependent spatial structure in snowpack loss. In some ecoregions, the strength and distance of positive autocorrelation between losses increases with warming, suggesting that nearby watersheds will respond similarly. In other ecoregions, the distance and strength of positive autocorrelation decrease, indicating more variable responses to warming. Our framework quantifies these differences and will help water managers and researchers distinguish between watersheds with sensitive and resistant snowpacks, enabling more targeted management and monitoring of changes in snowmelt-dependent ecosystems.

3.2 Introduction

Snowy mountain landscapes provide a reservoir of water that supports millions of people in the western U.S. [Bales *et al.*, 2006]. In turn, human and ecological systems residing in mountainous regions are adapted to both the magnitude and timing of snowmelt runoff [Barnett *et al.*, 2005]. Recent studies document reductions in snow water equivalent [SWE; e.g. Mote *et al.*, 2005], earlier spring snowmelt [Stewart, 2009], and declines in annual streamflow quartiles [Luce and Holden, 2009]. These trends have been attributed to warming temperatures [Stewart, 2009], more precipitation falling as rain instead of snow [Knowles *et al.*, 2006], increases in the freezing elevation caused by changes in the Pacific-North American pattern [Abatzoglou, 2011], and reduced winter westerlies [Luce *et al.*, 2013]. The high certainty of predicted warming [Intergovernmental Panel on Climate Change, 2014] suggests that the future of mountain snowpack-derived water resources is uncertain.

Declines in mountain snowpack caused by warming have been widespread [Barnett *et al.*, 2008], but the magnitude and direction of these responses have varied between and within different regions [Barnett *et al.*, 2004; Stewart, 2009]. For example, Stewart *et al.* [2005] demonstrate that many USGS streamflow sites have experienced earlier snowmelt and peak streamflow timing. However, the significance and direction of these trends varies on a catchment by catchment basis [Stewart, 2009]. Furthermore, projections of +3°C winter warming indicate that declines in April 1 SWE and snow residence times at SNOTEL sites throughout the western U.S. will likely vary with region and even by station [Luce *et al.*, 2014]. Thus, there is a continuum of potential responses: some

watersheds may be quite sensitive to warming-driven snowpack loss, while others will likely exhibit greater resistance.

We hypothesize that differences in the regional climatic and elevation characteristics of mountain basins are important drivers of potential variability in hydrologic responses to warming. In particular, we expect that the rates of change in SWE with elevation and differences in the central tendencies, variances, and shapes of elevation distributions generate disparities in the ability of mountain watersheds to function as snowpack reservoirs. Advances in remote sensing techniques and data assimilation approaches are providing new understanding that allow spatially distributed estimates of how snow storage varies with elevation. LiDAR measurements of snow depth [Kirchner *et al.*, 2014] and data assimilation estimates of SWE [Giroto *et al.*, 2014; Tennant *et al.*, 2015] demonstrate that the relationship between snowpack and elevation often takes a sigmoidal form. At low elevations, peak SWE exhibits low rates of increase with elevation. Between low and middle elevations, peak SWE typically exhibits a rapid non-linear transition; in middle elevations, the relationship between peak SWE and elevation is linear. At the highest elevations, SWE or snow depth often levels off or even declines [Giroto *et al.*, 2014; Grunewald *et al.*, 2014; Kirchner *et al.*, 2014; Tennant *et al.*, 2015].

Here we focus on developing a robust framework for quantifying differences in the peak SWE-elevation relationships and elevation distributions of northern Rocky Mountain ecoregions. The framework was developed using spatially distributed (1 km²) estimates of peak SWE and elevation data for 634 mountain watersheds that cover a wide range of topographic and climate conditions. A simple function relating peak SWE and elevation is used to simulate and explore the potential responses of mountain watersheds to +1°C to

+4°C of warming, and to answer three main questions. (1) Which northern Rocky Mountain ecoregions are the most sensitive to warming-based snowpack loss? (2) How spatially variable are watershed snowpack losses within an ecoregion? Are they randomly distributed or strongly clustered? (3) Do snowpack losses of catchments within an ecoregion become more similar or diverge with continued warming? The results presented here have important implications for water resources management and sensitivity studies interested in the potential responses of snowmelt-dependent mountain ecosystems to warming.

3.3 Setting

We focused our sensitivity characterization on watersheds defined by 10-digit hydrologic unit codes (HUC-10) within four U.S. Rocky Mountain, EPA Level III ecoregions: the Canadian Rockies, Idaho Batholith, Middle Rockies and Northern Rockies (Figure 1). Because the delineated ecoregions [*Commission for Environmental Cooperation, 2009*] often cut across watershed boundaries [*U.S. Geological Survey and U.S. Department of Agriculture, Natural Resources Conservation Service, 2013*], we designated a watershed's ecoregion using its geometric center. Thus, Figure 1 shows slightly different extents than the published EPA Level III ecoregions. We selected these ecoregions (Figure 1) because they cover a wide range of elevations, topographic forms, and hydroclimates; thus we expect their sensitivities to warming and snowpack loss to be variable and conducive to testing our climatic and elevation-based framework. Based on this variability, we also expect differences in the spatial structure of how watersheds will respond to warming. We define the spatial structure as the strength and distance of correlation in watershed snowpack losses. These ecoregions also form headwaters for two

major rivers, the Columbia and Missouri Rivers, support numerous key mountain ecosystems (e.g. Yellowstone and Glacier National Parks), and provide critical habitat for native Rocky Mountain trout, salmon, and char [Isaak *et al.*, 2012].

3.4 Methods

3.4.1 Elevation-based framework

Within each ecoregion, we performed a statistical characterization of the HUC-10 watersheds, with the goal of developing a consistent framework for characterizing mountain watershed elevation distributions. We used HUC-10 boundaries to delineate and extract 10 m resolution elevation data from the National Elevation Dataset [Gesch *et al.*, 2002] for all watersheds contained within the four ecoregions (Figure 1).

For each HUC-10 watershed, we used the Bayesian Information Criterion [Claeskens and Hjort, 2008] to select a best-fit distribution from among 17 common distributions (e.g. Beta, Gaussian, Weibull, etc.) to characterize mountain watershed elevation distributions. Because nearly all of the watersheds surveyed in this study do not have symmetrical elevation distributions (i.e. they have non-zero skewness and kurtosis values), the mean is a biased estimator of a distributions central tendency. As observed in our previous work from central Idaho [Tennant *et al.*, 2015], we found the generalized extreme value distribution [Kotz and Nadarajah, 2000] to provide the best-fit for the majority of the HUC-10 watersheds (Table 1). The GEV probability function works well because it can describe the central tendency, variance, and shape (skewness and kurtosis) for a wide range of elevation distributions. The GEV probability density function (PDF)

$$f(x|k, \mu, \sigma) = \begin{cases} \left(\frac{1}{\sigma}\right) \exp\left(-\left(1 + k \frac{(x - \mu)}{\sigma}\right)^{-\frac{1}{k}}\right) \left(\left(1 + k \left(\frac{x - \mu}{\sigma}\right)\right)^{-1 - \frac{1}{k}}\right), & k \neq 0 \\ \left(\frac{1}{\sigma}\right) \exp\left(-\exp\left(-\frac{(x - \mu)}{\sigma}\right) - \left(\frac{x - \mu}{\sigma}\right)\right), & k = 0 \end{cases} \quad (1)$$

has three parameters that control the location (μ), scale (σ), and shape (k) of the distribution (Figure 2). Here, the location parameter (μ) specifies the elevation where a watershed's elevation distribution is centered. The mean, median, and mode are common analogs to the location parameter. The scale parameter (σ) describes the variance of the distribution; a large value for σ describes a broad distribution whereas a small scale parameter reflects a narrow distribution. As its name implies, the shape parameter (k) affects the shape of a distribution and does not alter the scale or location of the distribution. Skewness and kurtosis are examples of common analogs to the shape parameter. Maximum likelihood was used to estimate the location, scale, and shape parameter for each HUC-10 watershed within the study region (Figure 1).

3.4.1.1 GEV performance for modeling watershed elevation distributions

To evaluate the performance of the GEV PDF for characterizing natural watershed elevation distributions, we used Agresti's dissimilarity index (*ADI*) [Agresti, 1996].

$$ADI = 100 \left(\sum_{i=1}^N \frac{|O_i - E_i|}{2N} \right) \quad (2)$$

In the context of this study, the dissimilarity index (*ADI*) is the percentage of a watershed's elevation distribution that needs to be reclassified to perfectly match its GEV

PDF. O_i is the observed elevation of the i th bin of a watershed's elevation histogram, E_i is the corresponding expected value determined by the watershed's GEV PDF (eq. 1, see examples in Figure S1) and N is the number of observations. Because the number and width of histogram bins affects the estimate of the dissimilarity index, we used the Freedman-Diaconis rule [Freedman and Diaconis, 1981] to develop an unbiased bin width. The median dissimilarity index across all HUC-10 watersheds was 12% (Table 1).

Because of the large number of watersheds in which the GEV was the BIC best-fit distribution and the low median dissimilarity index (ADI), we argue that the GEV location (μ), scale (σ), and shape (k) values provide a flexible parameterization of mountain watershed elevation distributions. Furthermore, the GEV is advantageous because it offers the opportunity to simulate more elevation distributions than those identified by sampling natural watersheds alone [Tennant *et al.*, 2015].

3.4.2 Snowpack-based framework

3.4.2.1 Increase in SWE with elevation

A framework describing how SWE varies as a function of elevation is critical for understanding how snowpack-derived water resources could change as temperatures warm. We focus here on average annual peak SWE because it reveals the typical maximum water storage provided by snowpack on a year-to-year basis. We used daily estimates of SWE (1 km² resolution) from the National Weather Service's Snow Data Assimilation System (SNODAS) [Barrett, 2003; Carroll *et al.*, 2003] for the 2004 – 2014 water years to estimate how peak SWE varies as a function of elevation. SNODAS uses SNTHERM.89 [Jordan, 1991], a national-scale snow mass and energy model that

integrates instrumental and satellite observations of snow cover to develop daily, spatially-distributed SWE estimates (see *Clow et al.*, [2012], *Anderson et al.* [2014] and *Hedrick et al.* [2015] for in-depth reviews of SNODAS products). Gridded estimates of average peak SWE were matched to elevation grids with the same extent and resolution to calculate the average annual peak SWE elevation relationship across the 2004 – 2014 water years for the four ecoregions (Figure 3). Our estimates of peak SWE at the highest elevations within each ecoregion may be less accurate than at lower elevations because of fewer SNODAS pixels at these elevations.

3.4.2.2 Modeling current and future peak SWE-elevation relationships

It is critical to understand how peak SWE currently varies as a function of elevation in order to accurately predict potential warming-driven reductions to the peak SWE-elevation relationship. We previously established that the Richard’s function (eq. 3) is a robust function for modeling the current (Figure 3) and potential future average annual peak SWE-elevation relationships [*Tennant et al.*, 2015]. The Richard’s function has four parameters that can be used to compare average annual peak SWE elevation relationships for different regions (Table 2).

$$SWE_{pk}(elev_i) = A \left[1 + v \exp \left\{ 1 + v + \frac{M}{A} (1 + v)^{1 + \frac{1}{v}} (\lambda - elev_i) \right\} \right]^{-1/v} \quad (3)$$

In the Richard’s function, A defines the maximum peak SWE value, M is the maximum slope of the curve, λ sets the elevation where peak SWE increases rapidly and v is a parameter that influences the shape of the function.

The relationship between peak SWE and elevation in the Canadian Rockies, Idaho Batholith, and Middle Rockies ecoregions was not monotonic; peak SWE declined with

elevation beyond a critical elevation (Figure 3b-e). To determine the elevation where this decline initiated, we identified where the first derivative of a 3rd order polynomial fit to the peak SWE-elevation relationship experienced a sign change. Following the mathematical terminology, we refer to this elevation as the turning point. Peak SWE for elevations below the turning point were modeled with the Richard's function. For elevations above the turning point, peak SWE was described with a linear fit (Table S1). The elevation of the turning point was held constant under a series of warming scenarios (detailed below, Figure 4). We evaluated the peak SWE-elevation relationship for water years with high and low snowfall amounts and found that while the maximum peak SWE (A) and the maximum slope (M) varied on an annual basis, the elevation of the turning point was consistent, varying on average only by tens of meters (Figure S2).

To simulate the potential effects of a warmer climate on the average annual peak SWE-elevation relationship (Figure 4), we shifted λ in eq. 3 to higher elevations using typical lapse rates of -0.65°C per 100 m. We held the slope of the linear fit between peak SWE and elevation constant to maintain the form of the current relationship (Figure 3). Shifting λ to higher elevations reduces peak SWE in a systematic manner; the greatest peak SWE loss occurs in mid elevation zones where warming is most likely to reduce snowpack. While it has been demonstrated that seasonal [Lundquist and Cayan, 2007] and intra-storm [Marks et al., 2013] lapse rates can be variable, the rate cited above best reflects the average annual lapse rate [Rolland, 2003] and is important for determining the long-term average annual peak SWE-elevation relationship.

3.4.3 Simulating watershed warming-driven snowpack loss

To evaluate how patterns of snowpack loss could vary with ecoregion, areal-average peak SWE ($\overline{SWE_{pk}}$) was calculated for +1°C, +2°C, +3°C, and +4°C for each HUC-10 catchment (Figure 1) using the following equation:

$$\overline{SWE_{pk}} = \sum_{i=1}^N SWE_{pk(i)} (a_i) \quad (4)$$

where a_i is the fractional catchment area within the range of the i th elevation bin and $SWE_{pk(i)}$ is the peak SWE at the i th elevation. $SWE_{pk(i)}$ for the current (+0°C), and future warming scenarios (+1°C to +4°C) was determined using equation (3). As described in section 3.2.2, we simulate the influence of warming by shifting λ to higher elevations to systematically change the average annual peak SWE-elevation relationship. We used 10 m resolution elevation data to determine $\overline{SWE_{pk}}$ for each HUC-10 watershed instead of matching the resolution of our elevation data to the 1 km² SNODAS grids. We found that resampling the elevation data to 1 km² cells affected estimates of the central tendency, variance and shapes of the elevation distributions. Applying the SNODAS model to the higher resolution elevation data to quantify the peak SWE-elevation relationship required extrapolation of the Richard's function and linear fits shown in Figure 3 to the highest and lowest elevations within a catchment. On average, this extrapolation affected < 1% of the catchment area.

3.4.4 Geographically weighted regression of watershed peak SWE loss

Understanding the similarity in peak SWE losses between neighboring watersheds requires an assessment of the spatial structure and potential autocorrelation of simulated

peak SWE loss for catchments within an ecoregion. This assessment was performed using geographically weighted regression (GWR; equation (5)) between modeled catchment SWE losses (y_i) and potential explanatory variables (X_{ij}), such as the GEV-estimated elevation parameters (location (μ), scale (σ), and shape (k)) weighted by regression coefficients (β) that may vary across space (u_i, v_i).

$$y_i = \beta_0(u_i, v_i) + \sum_j \beta_j(u_i, v_i)X_{ij} + \varepsilon_i \quad (5)$$

Regression coefficients (β) are estimated for each watershed i , where (u_i, v_i) denotes the coordinates of the geometric center of the i th watershed, and j refers to each possible explanatory variable.

The calibration of regression coefficients (β) in eq. 5 assumes that neighboring watersheds' peak SWE losses near watershed i are more influential in determining regression coefficients than ones that are far from i . This is accomplished by weighting observations near the i th watershed as a function of their distance from i . Regression coefficients ($\hat{\beta}$) are estimated by:

$$\hat{\beta}(u_i, v_i) = (X^T W(u_i, v_i) X)^{-1} X^T W(u_i, v_i) y \quad (6)$$

where a weighting matrix (W) determines the weight given to a surrounding watershed, in the estimation of regression coefficients (β). Each element w_{ij} of the W matrix is determined by a weighting function, and in this study, we used three common weighting functions: a bi-square, Gaussian, and moving window. We selected the weighting function that both minimized the score of the Akaike information criteria corrected for

sample size [AIC_c; *Hurvich and Tsai*, 1989] and produced the lowest amount of autocorrelation in regression residuals. According to these criteria, we selected the bi-square function (eq. 8) for the Idaho Batholith, Middle Rockies and Northern Rockies:

$$w_{ij} = \begin{cases} \left[1 - \left(\frac{d_{ij}}{b}\right)^2\right]^2 & \text{if } d_{ij} < b \\ 0 & \text{otherwise} \end{cases} \quad (7)$$

We selected a Gaussian function (eq. 9) for the Canadian Rockies:

$$w_{ij} = \exp\left[-1/2(d_{ij}/b)^2\right] \quad (8)$$

Equations (7) and (8) determine the weight (w_{ij}) given to the n surrounding watersheds within distance (d_{ij}) of watershed i modified by the bandwidth (b) of the weighting function. AIC_c was used to select the optimal bandwidth (b) of each ecoregions weighting function for each GWR (+1°C, +2°C, +3°C, and +4°C). All GWRs were performed using the Spatial Analysis in Macroecology (SAM) software package [*Rangel et al.*, 2010]. Diagnostic statistics and further information regarding the regressions can be found in Geographically Weighted Regressions section of the supplemental information, Tables S2 – S9, and Figures S3 – S6.

Understanding the spatial structure of how watersheds respond to warming is important for managing water resources and snowmelt-dependent ecosystems. We define spatial structure as the similarity or dissimilarity in how watersheds within a given ecoregion respond to warming and snowpack loss. We used Moran's I (equation S4) as a measure of spatial autocorrelation as it reveals both the correlation between watersheds' snowpack losses and the distance over which this correlation persists. Moran's I is a spatial

extension to Pearson's correlation coefficient (r) and takes values on the interval -1 to +1; -1 indicates a strong negative correlation and +1 indicates a strong positive correlation [Legendre and Legendre, 2012].

3.5 Results and discussion

Our simulations show that peak SWE losses in Rocky Mountain ecoregions are controlled by the individual elevation distributions of each watershed as well as the current (Figure 3a) and anticipated relationships (Figure 4) between average annual peak SWE and elevation. Below we summarize results from warming simulations and discuss the variability of peak SWE loss between and within ecoregions. We also characterize how elevation and snowpack-enhancement may control peak SWE loss, and detail ecoregion-specific spatial structures in how watersheds could respond to warming.

3.5.1 Inter-ecoregion patterns of peak SWE loss

The magnitude of the peak SWE loss response to warming scenarios varies with ecoregion (Figure 5). The Canadian Rockies and Northern Rockies have the largest absolute and relative peak SWE losses while the Idaho Batholith and Middle Rockies ecoregions exhibit smaller losses. For example, with +1°C warming, the Canadian and Northern Rockies ecoregions both experience median peak SWE losses around 100 mm whereas the median losses in the Idaho Batholith and Middle Rockies ecoregions are 50 mm or less. Relative peak SWE losses (Figure 5e - h) are also generally higher in the Canadian and Northern Rockies ecoregions.

The distributions of absolute and relative peak SWE losses are also variable between the four ecoregions. Absolute peak SWE losses exhibit greater variability in the Canadian

Rockies and Northern Rockies ecoregions (Figure 5a - d). Under most warming scenarios, each ecoregion has a small number of watersheds with low amounts of peak SWE loss. This is especially pronounced in the Idaho Batholith and Middle Rockies relative peak SWE losses (Figure 5e - h).

In part, the differences in absolute and relative peak SWE loss between the ecoregions reflect variability in the magnitude of the average annual peak SWE-elevation relationships (Figure 3a). The Canadian Rockies and Northern Rockies ecoregions currently have higher maximum peak SWE values (Table 2; parameter A) and higher rates of increase in peak SWE with elevation (Table 2; parameter M) than the Idaho Batholith and Middle Rockies ecoregions. This indicates that, on average, watersheds in the Canadian and Northern Rockies ecoregions have greater peak SWE and thus more to lose. The steep slopes in their peak SWE-elevation relationships (Figure 3b and 3e) also make these two ecoregions more susceptible to declines in their anticipated snowpack-elevation enhancement rates under a warmer climate. In these two regions, shifting the elevation where peak SWE exhibits rapid increases (parameter λ ; eq. 3) results in large changes to the peak SWE elevation relationship (Figure 4a and d). The Canadian and Northern Rockies elevation distributions (Figure 3f) also drive their larger absolute and relative peak SWE losses. These ecoregions have large proportions of land area at lower elevations (Figure 3f) and thus their snowpack storage is currently located at lower elevations, making them more susceptible to warming-driven snowpack loss (Figure 5). In contrast, the Idaho Batholith and Middle Rockies ecoregions have elevation distributions with more area at higher elevations (Figure 3f) that will remain above the freezing elevation (Figure 5).

3.5.2 Intra-ecoregion patterns of peak SWE loss

Variability in the peak SWE-elevation relationships (Figure 3a) and the elevation characteristics (Figure 3f) of the four ecoregions produce different patterns of snowpack loss with respect to the location parameter of the HUC-10 watersheds (Figure 6). Two patterns of absolute peak SWE loss are observable. In the Canadian and Northern Rockies ecoregions, watershed peak SWE losses are mostly positive and linear across the range of watershed location parameters (Figure 6a and d). Peak SWE losses in the Idaho Batholith and Middle Rockies catchments are linear and increase up to a maximum value. Above the elevation zone with maximum loss, peak SWE losses decline as the elevation of the watershed location parameter increases (Figure 6b and c). As warming progresses, the slopes of the relationships between peak SWE loss and the watershed location parameters become progressively steeper, indicating increasing SWE loss in high elevation catchments (Figure 6a - d).

Some patterns of relative peak SWE loss as a function of the watershed location parameter are similar to the patterns of absolute peak SWE loss. Relative peak SWE losses generally decrease with the location parameter across the Canadian Rockies and the Northern Rockies across their full range of elevations (Figure 6e and h), whereas, relative peak SWE losses in the Idaho Batholith and Middle Rockies do not exhibit significant correlation with the watershed location parameter except at higher elevations (Figure 6f and g). For the higher watershed location parameters, relative peak SWE loss in the Idaho Batholith and Middle Rockies show inverse relationships; the elevation of this transition corresponds to the elevation where maximum absolute peak SWE losses occur (Figure 6b and c). Relative peak SWE losses in watersheds with location

parameters below this elevation have slopes that are not distinguishable from zero (Figure 6f and g). The poor correlation between relative peak SWE losses and the watershed location parameters in low to middle elevations in the Idaho Batholith and Middle Rockies ecoregions reflects higher proportional losses in middle elevation watersheds. Because the areally-averaged peak SWE for the HUC-10 catchments is determined for each ecoregion (eqs. 3 and 4), the scatter in the relationships between peak SWE loss and the elevations of the watershed location parameters reflects variations in the elevation distributions of HUC-10 watersheds (Figure 6). Each watershed exhibits variance that cannot be explained by the watershed's location parameter alone (Figure 6). This indicates the scale and shape parameters of a catchment's elevation distribution also influence a catchment's sensitivity to warming and snowpack loss [Tennant *et al.*, 2015].

3.5.3 Spatial structure of ecoregion peak SWE loss

Identifying the spatial structure of snowpack losses is critical for measuring the sensitivity of mountain watershed to warming and will be useful for managing water and ecosystem resources under a warmer climate. Maps of absolute and relative peak SWE loss illustrate that there is a strong spatial structure to how watersheds within each ecoregion respond to warming and snowpack loss (Figure 7).

Absolute and relative peak SWE losses both exhibit spatial clustering (Figures 7-8 and S3-S6) and reflect spatial correlation in how watersheds respond to warming. Watersheds with high amounts of peak SWE loss tend to neighbor other watersheds with high amounts of loss and vice versa (Figure 7). We find it useful to evaluate both the absolute and relative amounts of average annual peak SWE loss in determining a watershed's

sensitivity. Watersheds that have high amounts of absolute and relative peak SWE loss (red colors in Figure 7) will likely experience significant hydrologic change with warming. Ones with low amounts of absolute and relative peak SWE loss (blue colors Figure 7) should be more resistant to warming. These two cases are end-members: one represents the most sensitive watersheds (all red, Figure 7) and the other represents the most resistant (all blue, Figure 7). A spectrum of sensitivities exist between these two end-member cases. Because our approach to modeling warming driven snowpack loss is based on ecoregion-specific climate and orographic characteristics (equations 3 and 4, Figure 3), our simulations demonstrate how variations in watershed elevation distributions, shaped by different tectonic, lithologic, and erosion histories, combine with current climatic characteristics to influence a watershed's sensitivity to contemporary warming.

Using the GEV location, scale, and shape parameters (Figure 2) to model geographic patterns of simulated snowpack loss provides a link between geomorphic history and current snowpack characteristics to understand drivers that influence a watershed's sensitivity. Based on geographically weighted regression (GWR), the GEV parameters location, scale, and shape and the ecoregion-specific spatial structure of watershed responses to warming explained most of the variation in peak SWE loss for +1°C, +2°C, +3°C, and +4°C warming (average R^2 of 0.97; Tables S2, S4, S6, and S8). As part of our model selection procedure, we evaluated AIC_c scores between ordinary least squares (OLS) regressions and GWR's; AIC_c consistently selected the GWR over the OLS generated regressions (Tables S2, S4, S6, and S8). AIC_c is designed to select the best model and penalizes heavily for the addition of extra parameters [Hurvich and Tsai,

1989]. The consistency with which AIC_c selected the GWRs over the OLS regressions, even though the number of parameters in a GWR far exceed those in an OLS regression, is strong evidence of spatial structure and autocorrelation in watershed peak SWE losses. This confirms that nearby watersheds tend to respond similarly to warming and snowpack loss (Tables S2, S4, S6, and S8). However, as we illustrate below, the strength and distance over which watersheds share similar responses is variable and ecoregion-specific.

To evaluate the spatial structure of simulated snowpack losses, we calculated Moran's I to determine the strength and characteristic lengths over which watersheds respond similarly to the simulated warming and snowpack loss. Results indicate that each ecoregion has a unique, characteristic scale of autocorrelation (Figure 8). Furthermore, the scale over which neighboring watersheds exhibit similar snowpack loss (or positive autocorrelation) changes in an ecoregion-specific manner with increasing warming. For example, both the strength and maximum distance of positive autocorrelation increase with warming for the Canadian Rockies and the Middle Rockies (Figure 8a and c). In the Canadian Rockies, the maximum correlation of watershed peak SWE losses for +1°C is 0.2, with watersheds exhibiting a positive correlation up to 40 km from one another. With +4°C warming the correlation increases to 0.52 and positive correlation persists up to 55 km (Figure 8a). In the Middle Rockies ecoregion, correlation increases from 0.48 to 0.6 from +1°C to +4°C and the maximum distance of positive correlation increases from 136 km to 210 km across the same warming interval (Figure 8c). In contrast, in the Idaho Batholith, the strength and distance of positive autocorrelation decreases from 0.65 to 0.29 and from 85 km to 55 km, respectively, from +1°C to +4°C warming (Figure 8b).

The spatial autocorrelation for the Northern Rockies is consistent across all warming scenarios (Figure 8d). These results emphasize that efforts to adapt water or ecosystem resources to climate warming will require an ecoregion-specific approach that acknowledges landscape complexity. Results from the numerical experiment presented in this manuscript demonstrate that simple variations in watershed elevation distributions and local rates of snowpack increase with elevation can produce a multiplicity of potential responses to warming.

3.6 Conclusions

The elevation and snowpack-based frameworks presented here attempt to capture the characteristics that may be most salient in evaluating catchment-scale sensitivity to warming and snowpack loss. We found that the elevation characteristics and peak SWE elevation relationships vary with ecoregion (Figure 3). The generalized extreme value parameters (location (μ), scale (σ), and shape (k)) provide a consistent framework for characterizing mountain watershed elevation distributions. The Richard's function (equation (3)) provides a robust methodology for describing current average annual peak SWE-elevation relationships and can be easily adjusted to model potential future relationships between peak SWE and elevation under a warmer climate (Figure 4). Together, the GEV elevation parameters and the Richard's function provide a simple approach for evaluating how mountain watersheds could respond to warming and snowpack loss. Our warming simulations suggest that mountain snowpack losses will be non-linear and elevation- and ecosystem-dependent (Figures 5 and 6). Patterns of snowpack loss vary across and within ecoregions (Figure 7) and the spatial structure of snowpack loss is also ecoregion specific (Figure 8). The strength and distance over which

nearby watersheds exhibit similarity in their responses to warming and snowpack loss increases in some ecoregions, while in others they diverge (Figure 8).

The results presented here indicate that the vulnerability of snowmelt-derived water resources and snowmelt-dependent ecosystems to warming needs to be ecoregion and watershed specific. Our framework provides a parsimonious approach for characterizing the sensitivity of mountain snowpack to warming.

3.7 Acknowledgements

The elevation data used for this paper are available from the National Elevation Dataset (<http://ned.usgs.gov/>). The Snow Data Assimilation System (SNODAS) snow water equivalent (SWE) data for water years 2004 – 2014 can be obtained using the National Snow and Ice Data Center's Polaris tool (<http://nsidc.org/data/polaris/>). All MATLAB and R scripts used in the analyses presented here are available upon request from the lead author. This work was supported by awards from the Idaho State University Department of Geosciences and by the National Science Foundation award EAR 1349384, RC CZO Cooperative Agreement EAR 1331872 and the USDA ARS.

3.8 Figures and Tables

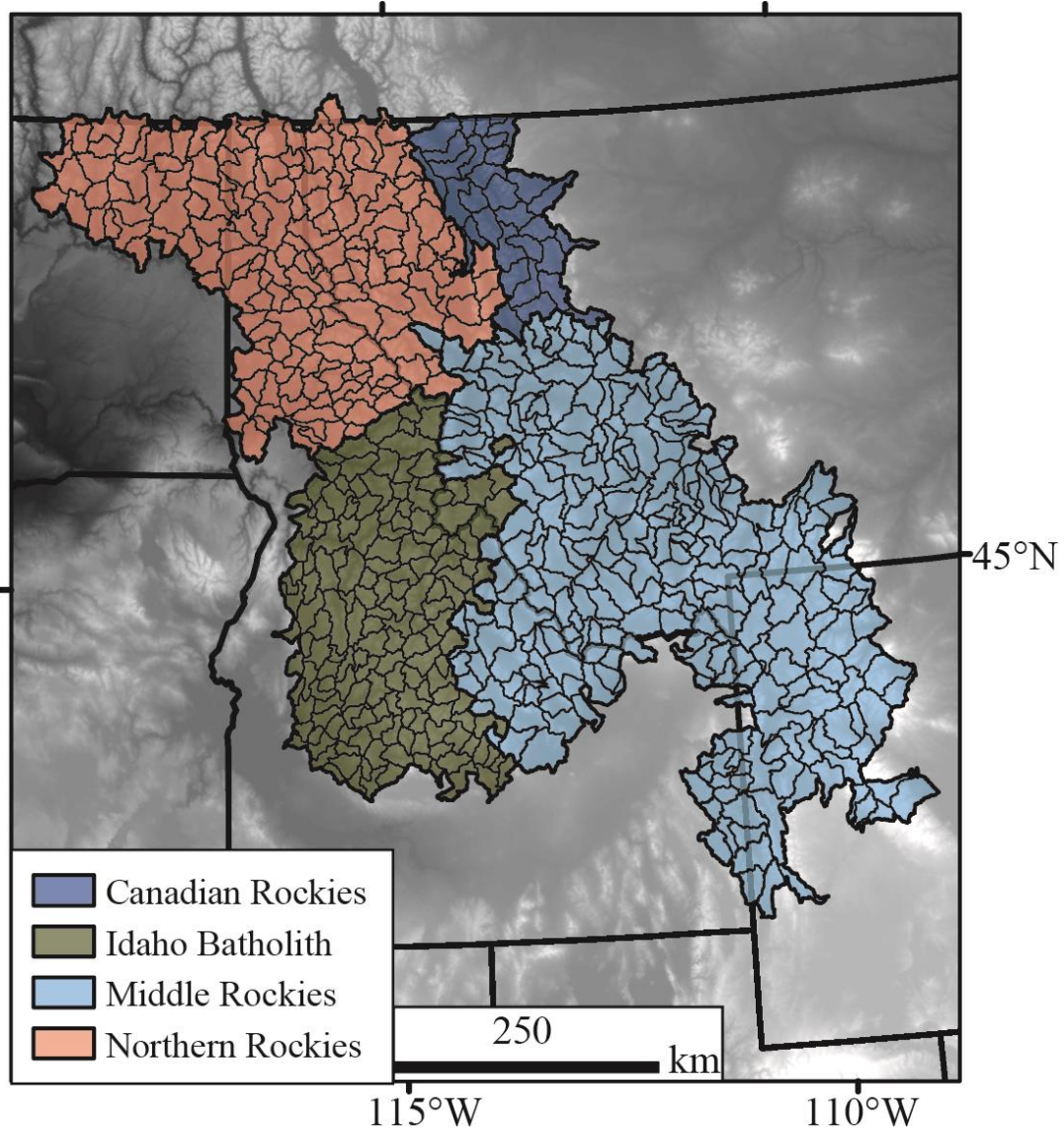


Figure 3.1. HUC-10 watersheds (thin black lines) and U.S. EPA Level-III ecoregion boundaries. Ecoregion delineations are from the *Commission for Environmental Cooperation* [2009] and are available at http://www.epa.gov/wed/pages/ecoregions/na_eco.htm. Ecoregion and watershed characteristics are presented in Table 1.

Ecoregion	# of catchments	Mean catchment area (km ²)	# of catchments where BIC selected GEV	Mean GEV-location (m)	Mean GEV-scale (m)	Mean GEV-shape	Median ADI (%)
Canadian Rockies	32	544	29 (91%)	1545	257	-0.024	12
Idaho Batholith	163	351	122 (75%)	1806	283	-0.207	9
Middle Rockies	268	488	242 (90%)	1970	243	0.005	12
Northern Rockies	171	478	107 (63%)	1042	221	-0.100	12
Combined Ecoregions	634	465	500 (79%)	1591	251	-0.082	12

Table 3.1. Summary statistics for HUC-10 catchments in each ecoregion and for all four ecoregions combined. Bayesian information criterion (BIC) routinely selected the generalized extreme value (GEV) as the best fit for catchment elevation distributions. The GEV parameters location, scale, and shape characterize the central tendency, variability, and shape, respectively, of a catchment's elevation distribution. Agresti's dissimilarity index (ADI; eq. 2) quantifies the amount of misfit between the GEV PDF and the actual elevation distribution. 0% would indicate a perfect fit.

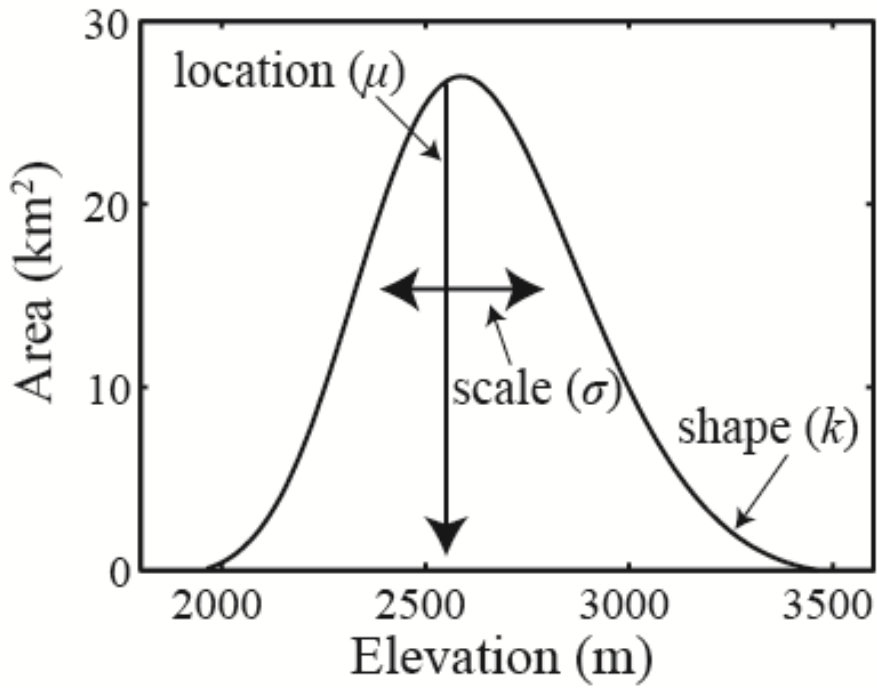


Figure 3.2. Idealized plot showing how the generalized extreme value (GEV) distribution parameters are used to characterize mountain watershed elevation distributions. Three parameters, the location (μ), scale (σ), and shape (k), describe the central tendency, variance, and shape (skewness and kurtosis) of the distribution.

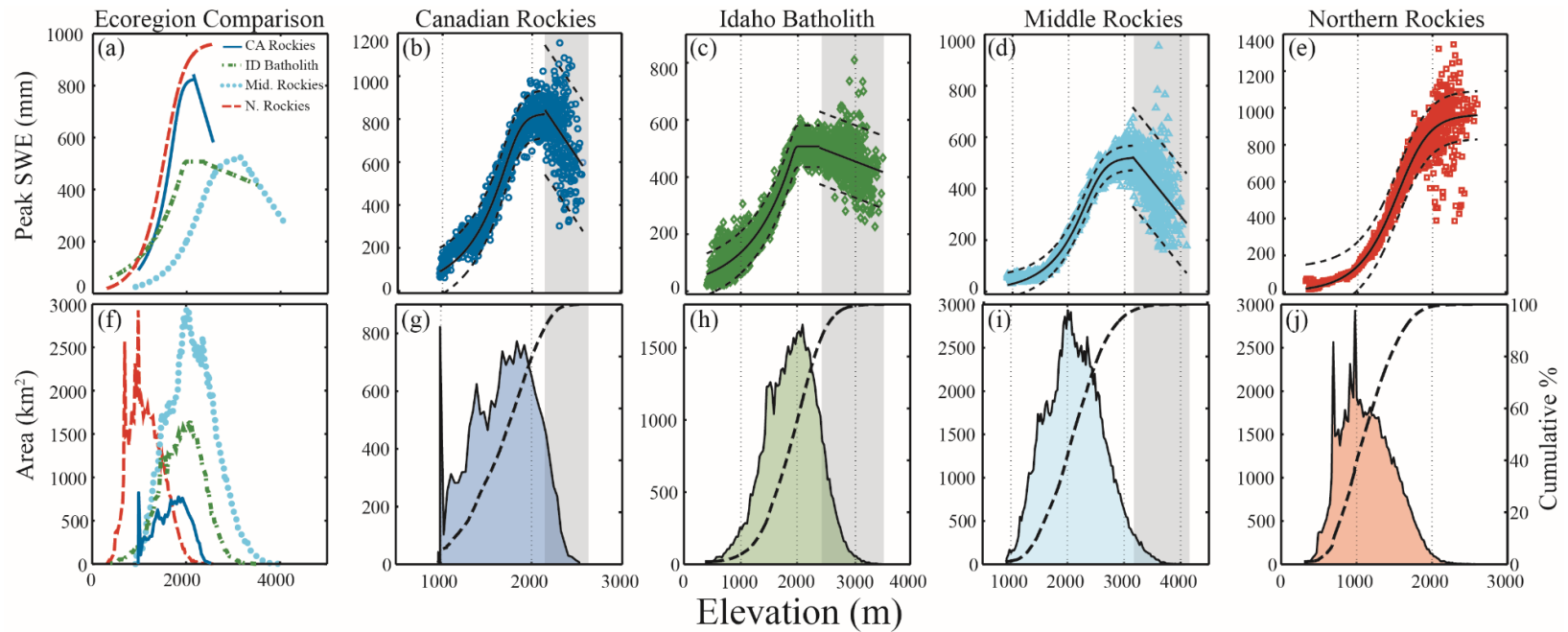


Figure 3.3. (a) All-ecoregion comparison of average annual peak SWE-elevation relation for water years 2004 – 2014. (b - e) The average annual peak SWE-elevation relationships for the four ecoregions with the combined Richard's/linear fits as solid lines (eq. 3) and 95% confidence intervals as dashed lines. (f) All-ecoregion comparison of elevation distributions. (g - j) The elevation distributions and cumulative percent of elevations (dashed black lines) for each ecoregion. The vertical grey bands highlight that only a small fraction of ecoregion area exists above the elevation of the turning point. Although the average annual peak SWE-elevation relationships for each ecoregion display sigmoidal forms, there is variability in the maximum value (A), maximum slope (M), the elevation where SWE exhibits rapid increase (λ), and rate of peak SWE decline above the turning point. The x and y axes limits vary with ecoregion.

Ecoregion	A (mm)	M (mm/m)	λ (m)	ν
Canadian Rockies	826	1.2	1234	4.9
Idaho Batholith	508	0.6	1133	43.6
Middle Rockies	522	0.5	1618	3.3
Northern Rockies	965	1.0	999	1.8

Table 3.2. Summary of Richard's parameters (eq. 3) describing A , the maximum peak SWE, M , the maximum slope, λ , the elevation where peak SWE exhibits rapid increase and ν , the shape parameter of average annual peak SWE-elevation for water years 2004 – 2014.

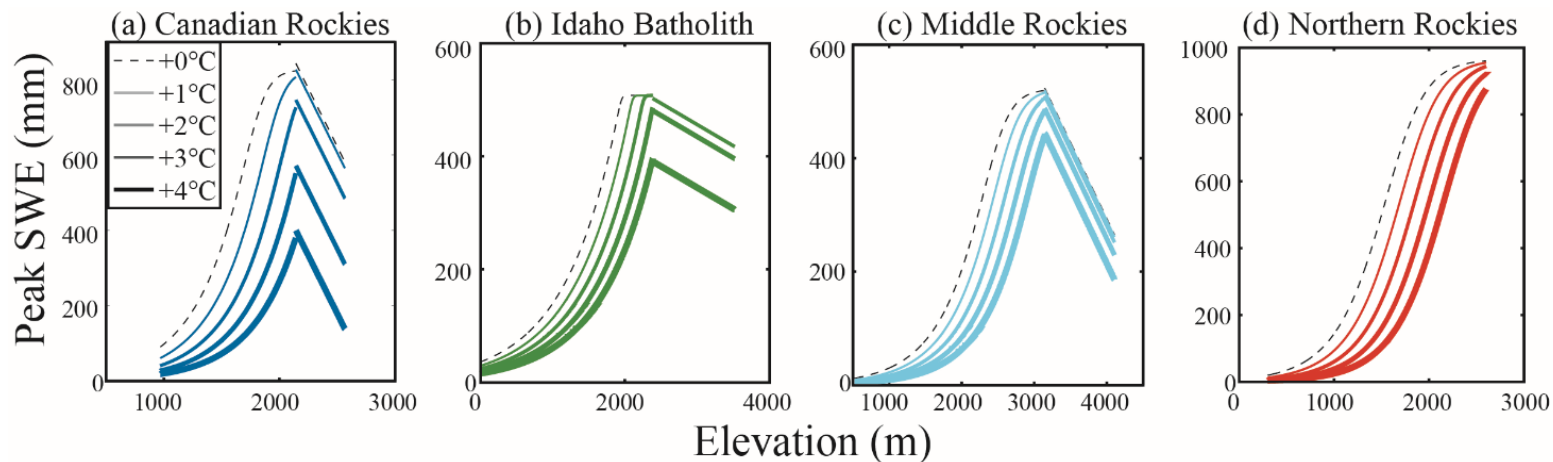


Figure 3.4. Predicted loss in the average annual peak SWE-elevation relationship for the (a) Canadian Rockies, (b) Idaho Batholith, (c) Middle Rockies, and (d) Northern Rockies with warming. For each ecoregion (a - d), the current (+0°C) peak SWE-elevation relationship is shown as a dashed line and predicted (+1°C, +2°C, +3°C, and +4°C) relationships are indicated by thickening lines. Future average annual peak SWE relationships were predicted using eq. 3. Note that x and y axes limits vary with ecoregion.

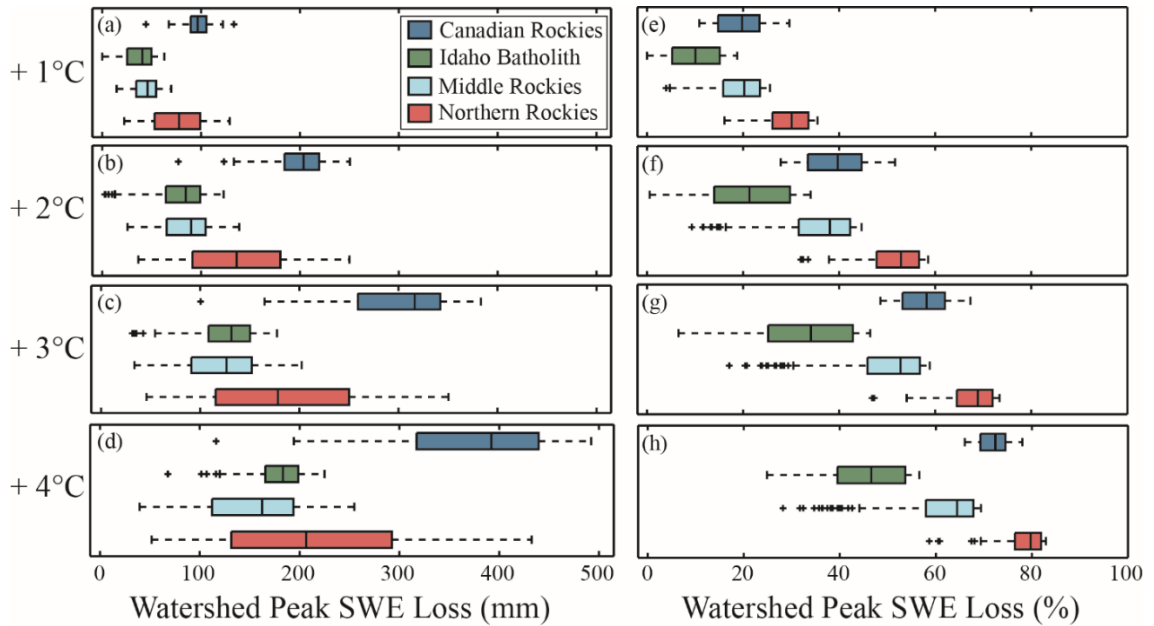


Figure 3.5. (a - d) Absolute and (e - h) relative peak SWE loss for +1°C to +4°C warming for HUC 10 watersheds located in the Canadian Rockies, Idaho Batholith, Middle Rockies, and Northern Rockies ecoregions. The edges of the boxes display the 25th and 75th percentiles (left and right edges, respectively) the vertical line shows the median, the whiskers extend to 1.5 times the inter-quartile range, and any values (+ symbols) that fall outside this range are considered outliers. Note that the Canadian and Northern Rockies ecoregions tend to have greater amounts of (a - d) absolute and (e - h) relative peak SWE loss.

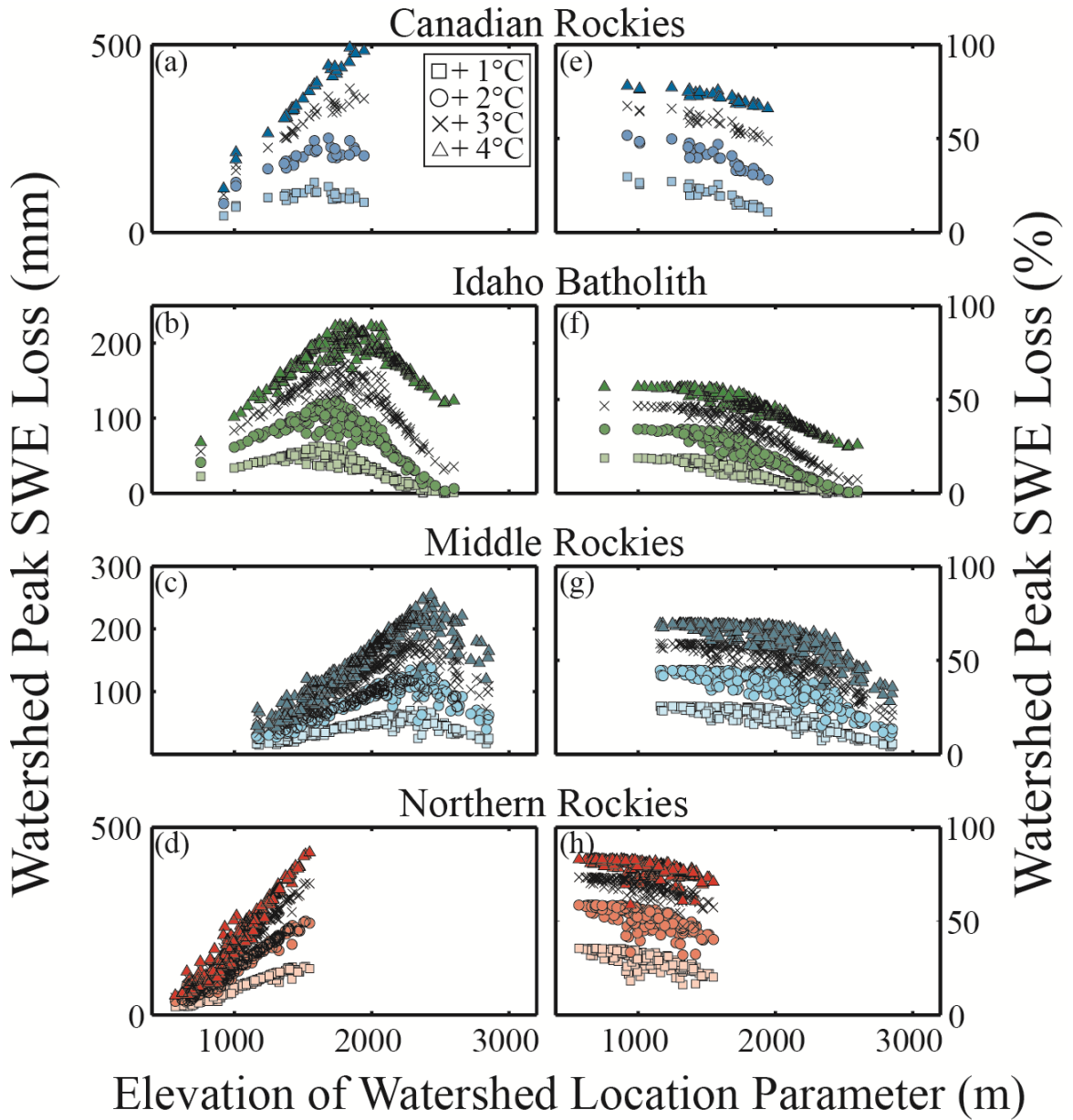


Figure 3.6. Relationships between the watershed location parameter (μ) of HUC-10 watersheds and (a - e) absolute and relative (e - h) cumulative peak SWE loss for the Canadian Rockies, Idaho Batholith, Middle Rockies, and Northern Rockies ecoregions. Note that the y-axis scales for peak SWE loss differ by ecoregion.

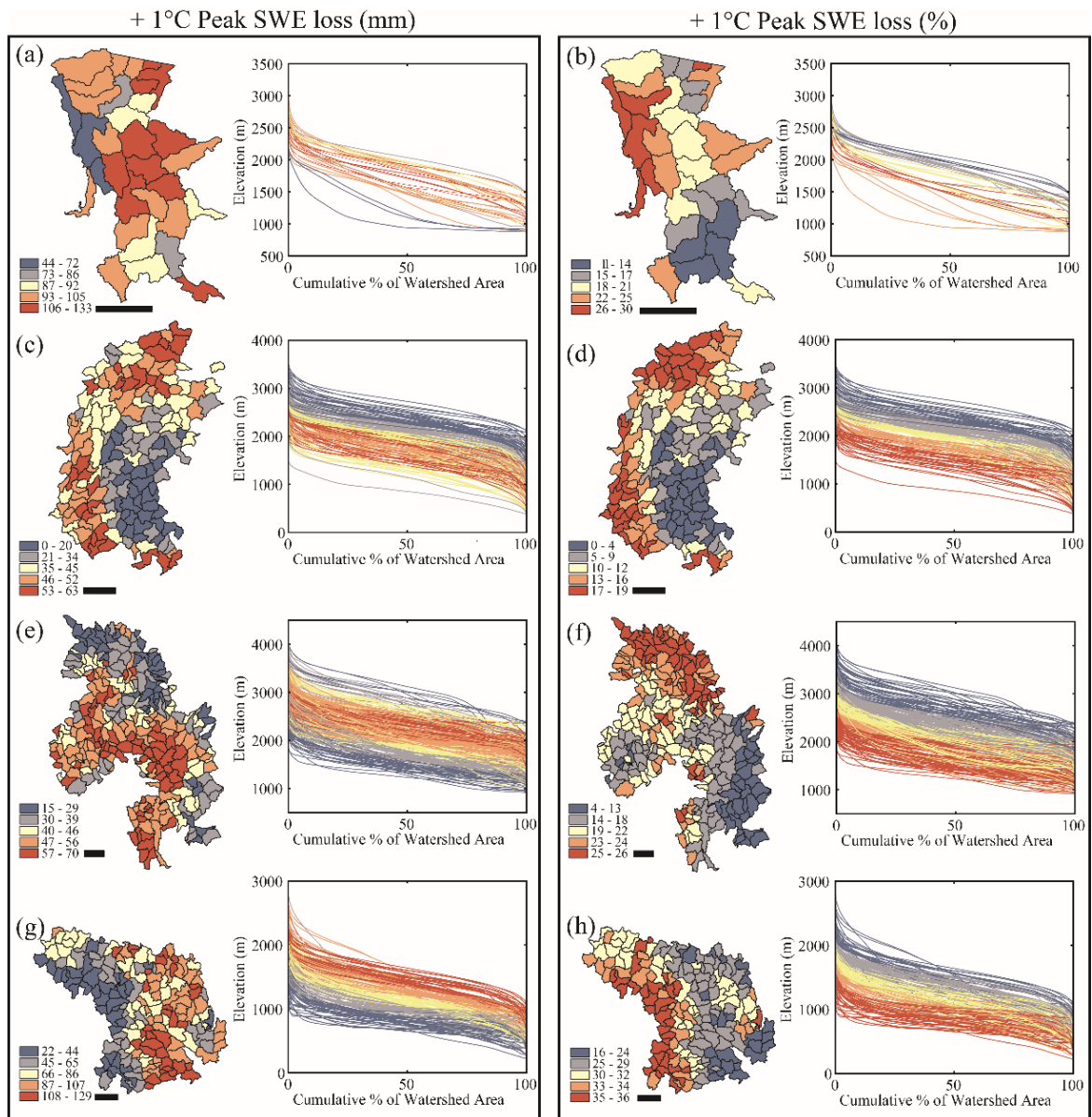


Figure 3.7. Maps and watershed elevation distributions (shown as hypsometric curves) of absolute (mm; left panel) and relative (%; right panel) average annual peak SWE loss with +1°C warming for HUC-10 watersheds within the (a and b) Canadian Rockies, (c and d) Idaho Batholith, (e and f) Middle Rockies, and (g and h) Northern Rockies ecoregions. Scale (horizontal black bar) represents 50 km. The hypsometric curves are colored by absolute (left panels) and relative (right panels) peak SWE loss to evaluate catchment sensitivity to snowpack loss. Note the spatial clustering in both absolute and relative peak SWE loss.

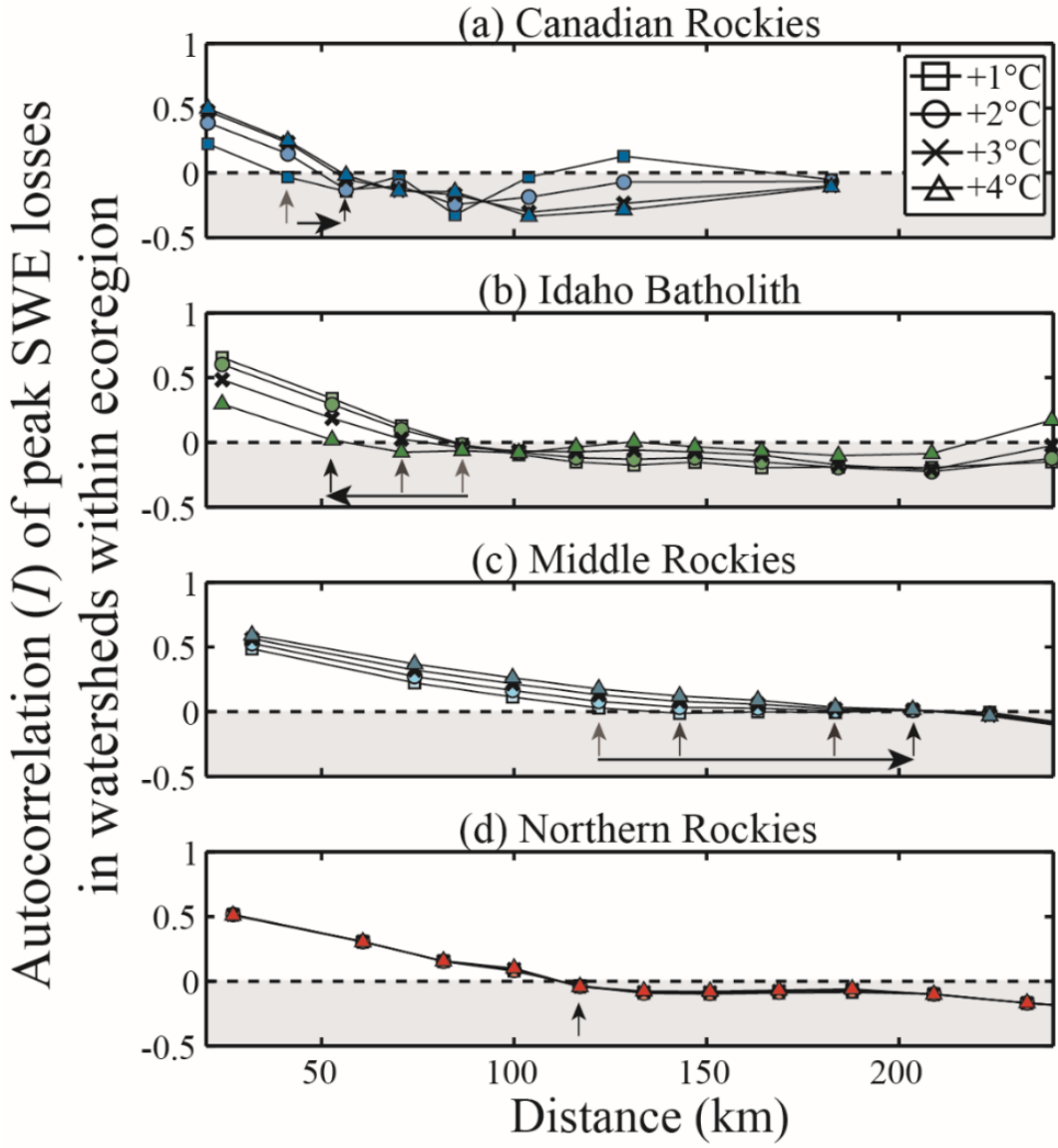


Figure 3.8. Spatial autocorrelation (Moran's I) of absolute peak SWE loss for HUC-10 watersheds in the (a) Canadian Rockies, (b) Idaho Batholith, (c) Middle Rockies and (d) Northern Rockies ecoregions. Positive autocorrelation of peak SWE loss between an ecoregion's HUC-10 watersheds persists at different characteristic scales and responds differently to warming. The vertical arrows highlight the distance (km) of positive spatial autocorrelation for a given warming scenario. Light to dark vertical arrows show change in the distance of autocorrelation with warming (+1°C to +4°C) and the horizontal arrows show the direction of change. When arrows overlap, only the darkest arrow will be visible; overlapping arrows indicate that the maximum distance of positive autocorrelation does not change with a given warming scenario.

3.9 References

- Abatzoglou, J. T. (2011), Influence of the PNA on declining mountain snowpack in the Western United States, *International Journal of Climatology*, 31(8), 1135-1142.
- Agresti, A. (1996), *An introduction to categorical data analysis*, Wiley New York.
- Bales, R. C., N. P. Molotch, T. H. Painter, M. D. Dettinger, R. Rice, and J. Dozier (2006), Mountain hydrology of the western United States, *Water Resources Research*, 42(8), 13.
- Barnett, T., R. Malone, W. Pennell, D. Stammer, B. Semtner, and W. Washington (2004), The effects of climate change on water resources in the west: Introduction and overview, *Climatic Change*, 62(1-3), 1-11.
- Barnett, T. P., J. C. Adam, and D. P. Lettenmaier (2005), Potential impacts of a warming climate on water availability in snow-dominated regions, *Nature*, 438(7066), 303-309.
- Barnett, T. P., et al. (2008), Human-induced changes in the hydrology of the western United States, *Science*, 319(5866), 1080-1083.
- Barrett, A. P. (2003), *National operational hydrologic remote sensing center snow data assimilation system (SNODAS) products at NSIDC*, 19 pp., NSIDC Spec. Rep. 11, Natl. Snow and Ice Data Cent., Boulder, Colo.
- Brunsdon, C., A. S. Fotheringham, and M. E. Charlton (1996), Geographically weighted regression: A method for exploring spatial nonstationarity, *Geographical Analysis*, 28(4), 281-298.
- Carroll, T., D. Cline, G. Fall, L. Li, and A. Nilsson (2003), Seasonal snow cover monitoring and modeling for the coterminous United States, paper presented at EGS-AGU-EUG Joint Assembly.

- Claeskens, G., and N. L. Hjort (2008), *Model selection and model averaging*, Cambridge University Press Cambridge.
- Fotheringham, A. S., M. E. Charlton, and C. Brunsdon (1998), Geographically weighted regression: a natural evolution of the expansion method for spatial data analysis, *Environment and Planning A*, 30(11), 1905-1927.
- Freedman, D., and P. Diaconis (1981), On the histogram as a density estimator: L 2 theory, *Probability theory and related fields*, 57(4), 453-476.
- Gesch, D., M. Oimoen, S. Greenlee, C. Nelson, M. Steuck, and D. Tyler (2002), The national elevation dataset, *Photogrammetric engineering and remote sensing*, 68(1), 5-32.
- Giroto, M., G. Cortes, S. A. Margulis, and M. Durand (2014), Examining spatial and temporal variability in snow water equivalent using a 27 year reanalysis: Kern River watershed, Sierra Nevada, *Water Resources Research*, 50(8), 6713-6734.
- Grunewald, T., Y. Buhler, and M. Lehning (2014), Elevation dependency of mountain snow depth, *Cryosphere*, 8(6), 2381-2394.
- Hurvich, C. M., and C.-L. Tsai (1989), Regression and time series model selection in small samples, *Biometrika*, 76(2), 297-307.
- Isaak, D. J., C. C. Muhlfeld, A. S. Todd, R. Al-Chokhachy, J. Roberts, J. L. Kershner, K. D. Fausch, and S. W. Hostetler (2012), The Past as Prelude to the Future for Understanding 21st-Century Climate Effects on Rocky Mountain Trout, *Fisheries*, 37(12), 542-556.
- Jordan, R. (1991), A one-dimensional temperature model for a snow cover: Technical documentation for SNTHERM. 89Rep., 1-49 pp.

- Kirchner, P. B., R. C. Bales, N. P. Molotch, J. Flanagan, and Q. Guo (2014), LiDAR measurement of seasonal snow accumulation along an elevation gradient in the southern Sierra Nevada, California, *Hydrology and Earth System Sciences*, 18(10), 4261-4275.
- Knowles, N., M. D. Dettinger, and D. R. Cayan (2006), Trends in snowfall versus rainfall in the Western United States, *Journal of Climate*, 19(18), 4545-4559.
- Kotz, S., and S. Nadarajah (2000), *Extreme value distributions*, World Scientific.
- Legendre, P., and L. F. Legendre (2012), *Numerical ecology*, Elsevier.
- Luce, C. H., and Z. A. Holden (2009), Declining annual streamflow distributions in the Pacific Northwest United States, 1948-2006, *Geophysical Research Letters*, 36, 6.
- Luce, C. H., J. T. Abatzoglou, and Z. A. Holden (2013), The Missing Mountain Water: Slower Westerlies Decrease Orographic Enhancement in the Pacific Northwest USA, *Science*, 342(6164), 1360-1364.
- Luce, C. H., V. Lopez-Burgos, and Z. Holden (2014), Sensitivity of snowpack storage to precipitation and temperature using spatial and temporal analog models, *Water Resources Research*, 50(12), 9447-9462.
- Lundquist, J. D., and D. R. Cayan (2007), Surface temperature patterns in complex terrain: Daily variations and long-term change in the central Sierra Nevada, California, *Journal of Geophysical Research-Atmospheres*, 112(D11).
- Marks, D., A. Winstral, M. Reba, J. Pomeroy, and M. Kumar (2013), An evaluation of methods for determining during-storm precipitation phase and the rain/snow transition elevation at the surface in a mountain basin, *Advances in Water Resources*, 55, 98-110.
- Rangel, T. F., J. A. F. Diniz, and L. M. Bini (2010), SAM: a comprehensive application for Spatial Analysis in Macroecology, *Ecography*, 33(1), 46-50.

- Rolland, C. (2003), Spatial and seasonal variations of air temperature lapse rates in Alpine regions, *Journal of Climate*, 16(7), 1032-1046.
- Stewart, I. T. (2009), Changes in snowpack and snowmelt runoff for key mountain regions, *Hydrological Processes*, 23 (1), 78-94.
- Tennant, C. J., B. T. Crosby, S. E. Godsey, R. W. VanKirk, and D. R. Derryberry (2015), A simple framework for assessing the sensitivity of mountain watersheds to warming-driven snowpack loss, *Geophysical Research Letters*, 42 (8), 2814–2822, doi:10.1002/2015GL06341 3.

Chapter 4: The influence of elevation, aspect, and vegetation on seasonal snowpack: case studies from five mountain Critical Zone Observatory sites across the western U.S.

4.1 Abstract

Warming could alter the hydrologic regimes of snow dominated areas by increasing the proportion of rain to snow and by expanding the extent, density, and activity of mountain vegetation. Toward these ends, we evaluate the influence of elevation, aspect, and forest cover on the spatial distribution of seasonal snow accumulation using snow-on, snow-off Light Detection and Ranging (LiDAR) data from five Critical Zone Observatory (CZO) sites across the western U.S. All sites exhibit increases in snow depth with elevation; however, the relationship between snow depth and elevation is not monotonic and rates of increase vary from site to site. The elevation distributions of the CZOs generally predict snow volume distributions with high accuracy, implying that hypsometry provides a useful measure of a watershed's sensitivity to warming-driven snowpack loss. At sites where elevation less reliably predicts snow storage, wind transport and aspect-dependent snow storage were important. The dependence of snow depth on aspect and vegetation varied with site. At four of the sites, northern aspects in alpine or non-forested areas have mean snow depths that were two to five times greater than snow depths in forested areas. At Reynolds Creek, a watershed characterized by low amounts of forest-cover (11% of total area), this trend reversed with mean snow depths in forested areas up to seven times greater than in open areas. Results from this study emphasize that the though the relation between elevation and snow depth is robust at coarser scales, the

regional-scale mass and energy fluxes and site specific topographic and vegetation characteristics produce a wide range of local patterns in snow accumulation.

4.2 Introduction

Understanding the processes controlling the rate of snowpack increase with elevation is critical for quantifying water resources and is an important driver of ecosystem health in mountain landscapes. Streamflow amount [Berghuijs *et al.*, 2014], timing [Stewart *et al.*, 2005], and summer low flows [Godsey *et al.*, 2013] all exhibit strong correlation with snow water equivalent or the fraction of precipitation falling as snow. Mountain snowpack amount and melt timing are also strongly linked to forest greenness [Trujillo *et al.*, 2012] and the amount and timing of carbon sequestration and efflux [Brooks *et al.*, 2011; Monson *et al.*, 2002; Stielstra *et al.*, 2015]. High certainty of future warming [IPCC, 2014], coupled with potential increases in precipitation [Seager *et al.*, 2013] will likely alter the volume and extent of mountain snowpacks and drive the need to improve our understanding of the processes controlling the spatial distribution of seasonal snowpacks. In particular, there is a pressing need to understand how snow storage varies across elevation gradients in mountain critical zones with diverse topography, different snowpack regimes, and non-uniform vegetation characteristics, as the effects of warming on snowpack will likely be region- and elevation-dependent [Tennant *et al.*, 2015].

The increasing availability of high resolution, spatially-extensive Light Detection and Ranging (LiDAR) derived snow depth products [e.g. Harpold *et al.*, 2014] offer the ability to understand how regional-scale climatic characteristics interact with the local topographic and vegetation characteristics to produce seasonal snow accumulation. For example, Kirchner *et al.* [2014] demonstrate that LiDAR snow-on and snow-off

measurements capture spatial patterns of snowpack increase with elevation that are not revealed by meteorological stations. Results from both high resolution LiDAR surveys [Grünewald *et al.*, 2014; Kirchner *et al.*, 2014] and spatially distributed data assimilation approaches [Giroto *et al.*, 2014] demonstrate that snow depths (or water equivalent) often increase approximately linearly with elevation up to some maximum value/threshold elevation. Above this elevation, snow depths often decline with increasing elevation. Moisture exhaustion of precipitating clouds [Kirchner *et al.*, 2014] and land cover dominated by steep, rocky exposures [Grünewald *et al.*, 2014] were posited to be driving factors controlling the elevation at which snow depths declined. Results from Tennant *et al.* [2015] suggest that both variability in snowpack amount and the elevation above which snow depths (or water equivalent) exhibit declines could be linked to the presence or absence of forest cover.

Although snow depths/SWE exhibit some predictable patterns, there can be extensive variability at any given site. Snowpack declines and changes in snowmelt runoff from mountainous areas throughout the western U.S. [Stewart *et al.*, 2005] and around globe [Stewart, 2009] vary regionally and locally. Stewart *et al.* [2009] posit that variability in snowpack and streamflow responses to warming could be driven by variations in local elevation and climatic characteristics. In attempt to capture these potential drivers, Tennant *et al.* [2015 and in review] developed a simple predictive framework that characterizes the elevation-area distributions or hypsometries of mountain watersheds and regional rates of increase in snow water equivalent with elevation and use this framework to simulate warming-driven snowpack loss. Their results suggest that differences in the central tendencies, variances, and shapes of mountain watershed

elevation distributions are capable of explaining a large amount of variance in simulated snowpack losses (R^2 of 0.97 on average).

The framework developed by *Tennant et al.* [2015] and applied in *Tennant et al.* [in review] is particularly appealing for watershed management or sensitivity analyses because it demonstrates that knowledge of a watershed's elevation distribution (easily obtained from a DEM) and information about the rate of increase of snowpack with elevation (obtained from spatially distributed models of SWE) can be used to evaluate the sensitivity of mountain watersheds to snowpack loss. However, a central assumption of this work is that a watershed's elevation distribution is an accurate descriptor of where the majority of snowpack storage occurs; elevations above the freezing line that comprise a large amount of area are posited to provide the majority of snowpack storage. While this idea is supported by theory and observations [*Roe*, 2005], the low density of meteorological stations in steep, high elevation terrain [*Kirchner*, 2006] make a robust test of this idea difficult. Furthermore, the framework developed by *Tennant et al.* [2015] focuses on the roles of elevation and rates of SWE increase with elevation in determining a watershed's sensitivity to warming. While elevation and precipitation are likely the most important drivers of snowpack accumulation at the watershed scale [*Clark et al.*, 2011] many studies have documented additional controls on snow depths, including redeposition by wind [*Winstral and Marks*, 2002; *Winstral et al.*, 2013] and sheltering by aspect and forest cover [*Anderson et al.*, 2014; *Biederman et al.*, 2014; *Link and Marks*, 1999; *Pomeroy et al.*, 2009; *Veatch et al.*, 2009]. Forests can influence spatial patterns of snow depth through interception, shading, wind sheltering, and radiation scattering,

causing snow depths to locally deviate from larger-scale elevation-based trends [Clark *et al.*, 2011; Rinehart *et al.*, 2008].

LiDAR-derived measurements of snow depth and vegetation height from five snow-dominated Critical Zone Observatories [CZOs; Harpold *et al.* 2014] provide the first opportunity to robustly test the influence of elevation, aspect, and vegetation on snowpack storage across sites that vary in their topographic, hydro-climatic, and vegetation characteristics. We use these novel datasets to answer the following questions.

(1) How consistent are the relationships between snow depth and elevation across the Critical Zone Observatories? (2) Is hypsometry an accurate predictor of where the majority of snowpack storage occurs? (3) How strongly do aspect and vegetation height influence snow depths? We hypothesize that the elevation distributions of the CZOs will closely match their snowpack distributions. This hypothesis will be tested using a dissimilarity index that quantifies the mismatch between the elevation and snowpack distributions. We further hypothesize that the CZOs with the greatest dissimilarities between their elevation and snowpack distributions will also exhibit the strongest aspect- or vegetation-dependent snow storage.

4.3 Data description and Critical Zone Observatories

4.3.1 LiDAR-derived snow depths

High resolution, spatially extensive measurements of snow depth can be obtained by differencing LiDAR-derived snow-covered and snow-free elevation products. A number of recent studies have validated the use of airborne LiDAR for measuring snow depth in both open and forested terrain with vertical accuracies in the decimeter range [Deems *et*

al., 2013; *Hopkinson et al.*, 2004]. The LiDAR-derived snow depth measurements used in this study were taken near or at peak snow accumulation and are from five U.S. National Science Foundation Critical Zone Observatories (CZOs) located in mountainous regions of the western U.S. (Figure 1): Boulder Creek Watershed (BCW), Jemez River Basin (JRB), Reynolds Creek Experimental Watershed (RCEW), and the Kings River Experimental Watershed (KREW) and Wolverton Basin (WOLV), both part of the southern Sierra CZO. The observatories differ in their land cover, elevation ranges and topographic characteristics (Figure 2), thus providing excellent test sites to evaluate controls on snow cover across a range of hydro-climates/snowpack regimes.

The National Center for Airborne Laser Mapping (NCALM) conducted the snow-covered surveys for all of the sites except for the RCEW which was surveyed by Watershed Sciences Inc. The accuracy of the LiDAR-derived snow depths was evaluated at BCW, JRB, KREW, and WOLV using ultrasonic snow depth sensors installed perpendicular to the snow surface in both forested and open terrain [*Harpold et al.*, 2014]. While the accuracy of the snow depths varied with location, the root mean square error (RMSE) of the LiDAR-derived snow depths at BCW, JRB, KREW and WOLV was 23 cm [*Harpold et al.*, 2014]. LiDAR derived snow depth accuracies at RCEW were quantified via manual snow survey measurements; the RMSE for all survey sites at RCEW was 27 cm [*Tinkham et al.*, 2014]. 1 m resolution gridded products of snow depth and bare-earth elevations produced by NCALM and the Boise Center Aerospace Laboratory were aggregated to 3 m resolution to reduce the bias of DEM derivative products [e.g. slope and curvature; *Kienzle*, 2004]. All snow depths on slopes greater than 50° were removed because of vertical bias of LiDAR on steep slope angles [*Deems et al.*, 2013]. All open

water bodies, buildings, roads or any other erroneous data points produced during interpolating and gridding of snow depths (e.g. edge effects) were identified by hand, masked, and removed to reduce the error of our analyses. For an in-depth evaluation of the LiDAR accuracies and methods used to produce gridded products see *Harpold et al.* [2014], *Kirchner et al.* [2014], and *Tinkham et al.* [2014].

In the following sections we describe the snow-covered extents for each CZO, provide further details of the LiDAR acquisitions, and discuss the topographic and vegetation characteristics of the CZOs. We delineate three vegetation cover categories based on measured canopy height. The alpine zone is defined as areas above a threshold elevation where vegetation heights are continuously < 2 m. Forested locations are designated as areas where vegetation heights are > 2 m and shrubland as areas where vegetation heights are < 2 m. For all CZOs, the snow-covered extents do not cover the full extent of the watershed area, thus our characterizations only apply to the snow-covered areas where LiDAR data were collected. We report our analyses using the Southern Rockies, Northern Basin and Range, and Sierra Nevada U.S. EPA Level-III ecoregions [*Commission for Environmental Cooperation*, 2009] as geographic grouping units (Figure 1).

4.3.2 Boulder Creek Watershed

The Boulder Creek CZO is located within the Boulder Creek Watershed (BCW) and drains 1160 km² of the Colorado Rocky Mountain Front Range (Figure 1). The LiDAR snow-covered surveys for the BCW were conducted on 5 May 2010 and 25 May 2010 and together covered an area >400 km². The snow-free LiDAR mission occurred on 21 - 26 August, 2010. Because melt occurred between 5 and 25 May, we only used snow

depths derived from the 5 May flight as these values better represent snow depths near peak accumulation. The full extent of the 5 May coverage was 112 km². The average RMSE of LiDAR-derived snow depths was 16 cm [Harpold *et al.*, 2014].

The 5 May snow-covered extent for BCW covers the greatest range of elevations (2316 - 4046) and has the greatest amount of area at high elevations of all the CZO sites (Figure 2a). East facing slopes compose the majority (63%) of BCW's area, with the most area (35%) located on southeast slopes (Figure 2b). The BCW has three vegetation cover categories, alpine, forest, and shrubland. The alpine zone is composed of elevations > 3298 m and occupies 27% of BCW's area. 38% of BCW is forested and the remaining 35% is covered by shrubland (Figure 2c).

Forest cover in BCW is primarily composed of Engleman spruce (*Picea engelmannii*), lodgepole pine (*Pinus contorta*), ponderosa pine (*Pinus ponderosa*), and subalpine fir (*Abies lasiocarpa*); above 3000 m land cover is dominated by rock and alpine tundra [Harpold *et al.*, 2014]. The average winter (1 October - 1 May) temperature and precipitation during the 2006 - 2011 water years at the Niwot SNOTEL (3020 m) were - 2.7°C and 452 mm, respectively [Harpold *et al.*, 2014]. The BCW is part of the Southern Rockies ecoregion (Figure 1) and is characterized by a continental snowpack regime with a long snow accumulation season of greater than 260 days [Trujillo and Molotch, 2014]. For further site characteristics and pictures visit the Boulder Creek Critical Zone Observatory webpage (<http://czo.colorado.edu/html/sites.shtml>, accessed 1 August 2015).

4.3.3 Jemez River Basin

The Jemez River Basin (JRB) Critical Zone Observatory is located in northern New Mexico (Figure 1) at the southern end of the Southern Rockies ecoregion. The snow-covered LiDAR flight occurred on 1 April 2010 and the snow-free flight on 29 June - 8 July 2010 [Guo, 2010]. The full extent of the snow-covered flight has an area of 294 km². The RMSE of LiDAR-derived snow depths was 22 cm [Harpold *et al.*, 2014]. The JRB snow-covered extent on 1 April 2010 ranged from 2247 m to 3430 m (Figure 2d). The JRB has a nearly even distribution of its area between the four aspect quadrants (Figure 2e). 49% of the JRB is covered by forest and the remaining 51% is shrubland; the JRB does not have an alpine zone (Figure 2f).

The lowlands of the JRB are primarily grasslands, at higher elevations land cover transitions to forests composed of aspen (*Populus tremuloides*), blue spruce (*Picea pungens*), Douglas-fir (*Pseudotsuga menziesii*), limber pine (*Pinus flexilis*), ponderosa pine, southwestern white pine (*Pinus strobiformis*), and white fir (*Abies concolor*) [Harpold *et al.*, 2014]. The average winter (1 October - 1 May) temperature and precipitation during the 2006 - 2011 water years at the Valles Caldera National Preserve Redondo climate station (3231 m) were -2.2 °C and 371 mm, respectively [Harpold *et al.*, 2014]. Like the BCW, the JRB is part of the Southern Rockies ecoregion (Figure 1). For further site characteristics and pictures visit the Jemez River Basin Critical Zone Observatory webpage (<http://criticalzone.org/catalina-jemez/>, accessed 1 August 2015).

4.3.4 Reynolds Creek Experimental Watershed

The Reynolds Creek Critical Zone Observatory is contained within the Reynolds Creek Experimental Watershed (RCEW) and is located in Owyhee Mountains of southwestern

Idaho (Figure 1). The snow-covered flight occurred on 19 March 2009 (snow-free on 10 - 18 November 2007) and covered an area of 75 km² [Glenn, 2009]. The RMSE of LiDAR-derived snow depths was 27 cm [Tinkham *et al.*, 2014]. The snow-covered area ranges in elevation from 1340 m to 2240 m (Figure 2g). The RCEW has the greatest amount of north-facing slopes of all of the CZO's (Figure 2h). The land cover in the RCEW is dominated by shrubland (89%), composed of big mountain sagebrush (*Artimesia tridentata*) and mountain snowberry (*Symphoricarpos oreophilus* Gray) with large areas of meadow (*Lupinus* ssp., *Carex* ssp., and *Poa* ssp.). Isolated stands of trees (11% of RCEW area, Figure 2i) are composed of aspen and Douglas-fir [Tinkham *et al.*, 2014]. The average winter (1 October - 1 May) temperature and precipitation during the 2006 - 2011 water years at the Reynolds Creek SNOTEL (1707 m) were 1.2 °C and 407 mm, respectively. The RCEW is located in the Northern Basin and Range ecoregion (Figure 1) and is characterized by an intermountain snowpack regime with an accumulation season between 220 and 260 days [Trujillo and Molotch, 2014]. For further site characteristics and pictures visit the Reynolds Creek Critical Zone Observatory webpage (<http://criticalzone.org/reynolds/>, accessed 1 August 2015).

4.3.5 Southern Sierra Critical Zone Observatory

4.3.5.1 Kings River Experimental Watershed

The Kings River Experimental Watershed (KREW) is located in Southern Sierra the Sierra Nevada Mountains of California (Figure 1) and is part of the Southern Sierra Critical Zone Observatory. The snow-covered LiDAR flight occurred on 20 March 2010 (snow-free on 5 - 8 August 2010) and covers an area of 18 km², with elevations that range from 1375 m to 2200 m (Figure 2j). The average RMSE of the LiDAR-derived

snow depths was 24.5 cm [Harpold *et al.*, 2014]. The KREW has the majority of its area (61%) on south-facing slopes (Figure 2k) and the greatest amount of forested area (60%) of all the CZOs (Figure 2o). The forests are composed of California black oak (*Quercus kelloggii*), incense-cedar (*Calocedrus decurrens*), Jeffrey pine (*Pinus jeffreyi*), lodgepole pine, ponderosa pine, and sugar pine (*Pinus lambertiana*) [Harpold *et al.*, 2014]. The average winter (1 October - 1 May) temperature and precipitation during the 2006 - 2011 water years at the Upper Providence climate station (1980 m) were 4.2 °C and 126.8 mm, respectively [Harpold *et al.*, 2014]. The KREW is located in the Sierra Nevada ecoregion (Figure 1) and is characterized by a maritime snowpack regime with an accumulation period of < 220 days [Trujillo and Molotch, 2014]. For further site characteristics and pictures visit the Southern Sierra Critical Zone Observatory webpage (<http://criticalzone.org/sierra/>, accessed 1 August 2015).

4.3.5.2 Wolverton Basin

The Wolverton (WOLV) basin is located in the Sierra Nevada Mountains of California (Figure 1) and is part of the Southern Sierra Critical Zone Observatory. The snow-covered LiDAR flight occurred on 21 and 22 March 2010 and the snow-free flight on 5 - 8 August 2010 [Anderson *et al.*, 2012; Guo and Bales, 2012]. The extent of the snow-covered flight is 59 km² and the overall RMSE of LiDAR-derived snow depths was 23 cm [Harpold *et al.*, 2014]. The WOLV snow-covered extent ranges in elevation from 1792 m to 3500 m (Figure 2m) with just over half of its area (51%) on north-facing slopes (Figure 2n). The majority (53%) of WOLV is in an alpine zone, with the remaining area composed of forest (19%) and shrubland (28%). The forested areas consist of red fir forests at low elevations that transition to subalpine forest in mid

elevations. The lower elevation forest is predominantly red fir (*Abies magnifica*), lodgepole pine, western white pine (*Pinus monticola*), and incense cedar; the subalpine forests includes Jeffery pine, red fir, western white pine, and lodgepole pine [Harpold *et al.*, 2014]. The average winter (1 October - 1 May) temperature and precipitation during the 2006 - 2011 water years at the Giant Forest meteorological station (2026 m) were 4.8 °C and 840 mm, respectively. Like the KREW, WOLV is located in the Sierra Nevada ecoregion (Figure 1). For further site characteristics and pictures visit the Southern Sierra Critical Zone Observatory webpage (<http://criticalzone.org/sierra/>, accessed 1 August 2015).

4.4 Methods

4.4.1 Snow depth, vegetation, and topographic analyses

We used grids of snow depth, bare earth elevation, and vegetation height published by Harpold *et al.* [2014] for all analyses. Grids of slope and aspect were calculated using the Spatial Analyst tool in ArcMap 10.2. (Environmental Systems Research Institute).

Because of the extensive small-scale variability present in LiDAR-based analyses we used a binning approach where the variables snow depth, slope, and vegetation height are binned by elevation and the mean value for each bin is reported. To provide an unbiased approach to selecting bin sizes, we used the Freedman and Diaconis rule [Freedman and Diaconis, 1981] which uses the data's variance and number of observations to set the bin size.

4.4.2 Elevation and snowpack distribution comparison

To evaluate if a CZO's elevation distribution was a good predictor of where the majority of its snow is stored we compared the CZO elevation distributions against their respective snowpack distributions. Distributions of snow volume were determined by taking the product of snow depth and the area of each cell (9 m²) and taking the mean snow volume for each elevation bin. To test how well the hypsometry (i.e. elevation distributions) of the snow-covered areas at each of the CZOs reflects the elevations of where the greatest snow volumes are stored we used Agresti's Dissimilarity Index [ADI; Agresti, 2002]:

$$ADI = 100 \left(\sum_{i=1}^N \frac{|O_i - E_i|}{2N} \right) \quad (1)$$

where O_i is the fractional amount of area and E_i is the fractional amount of snow volume at the i th elevation bin. The *ADI* score has the simple interpretation of being the smallest percentage of observed values (O) that need to be reallocated to match the expected values (E). We normalized area and snow volume by their respective ranges to calculate the *ADI* for each CZO.

4.4.3 Statistical analyses of snow depths in alpine, forested, and shrubland areas

To evaluate the influence of aspect and vegetation cover on mean snow depth we first grouped all snow depth values into northeast (NE; 0° to 90°), southeast (SE; 90° to 180°), southwest (SW; 180° to 270°), and northwest (NW; 270° to 360°) aspects. Snow depth values were further divided into alpine (areas above elevation where vegetation heights continuously < 2 m), forested (vegetation heights > 2m), and shrubland categories (vegetation heights < 2m below alpine zone). We used analysis of variance (ANOVA)

and the Tukey-Kramer Honestly Significant Differences (HSD) as a post-hoc test to evaluate group and pair-wise differences in mean snow depths for the aspect-dependent vegetation height groupings. We used a square root transformation to improve the normality and homoscedasticity of ANOVA residuals for the BCW and RCEW; JRB, KREW, and WOLV did not require transformations to meet ANOVA assumptions. The ANOVA and post-hoc Tukey-Kramer HSD test were performed in the R software package [*R Core Team*, 2013].

4.5 Results and discussion

4.5.1 How consistent are snow depth-elevation relationships?

Although the topography, elevation ranges, and regional snowpack regimes of the CZOs differ, snow depth generally increases with elevation across all sites (Figure 3). At all of the lowest elevations within each CZO, except RCEW, the rate of snow depth increase is equal to or nearly zero. The elevations and range of elevations where this zone occurs varies with each CZO (Figure 3). Above this zone there is a small range of elevations where snow depths exhibit rapid non-linear increase before increasing linearly with elevation. The JRB is notable compared to the other CZOs because of a small range between 2550 m and 2625 m where the rate of snow depth increase with elevation is nearly vertical; above 2625 m the rate of increase is much more linear (Figure 8).

At the highest elevations of all the CZO sites, except JRB, snow depths become more variable and generally decline with elevation (Figure 3). This pattern is the most consistent in RCEW and WOLV where above 2200 m and 3300 m, respectively, snow depth exhibits continuous declines with elevation (Figure 3). BCW and KREW also

exhibit decreases in snow depth at their highest elevations but with more complex patterns. KREW exhibits a local maxima in snow depth at 2080 m, after which snow depths decrease up to 2145 m; above this point, snow depths exhibit mostly consistent increases until the three highest elevation bins which show a negative relationship with elevation. BCW exhibits a similar pattern; after a local maxima in snow depth at 3360 m snow depths generally decline. However, this overall decrease in snow depths is interrupted by a local maxima at 3680 m and the global maxima at 3945 m. Elevations above 3945 m have decreasing snow depths (Figure 3).

4.5.2 Does hypsometry predict where most snow is stored?

Dissimilarity index (*ADI*) scores were generally low (3% - 13%), indicating that the elevation-area distributions of the CZOs are accurate indicators of where the greatest storage of snow occurs (Figure 4). An *ADI* score of 3% or lower [Agresti, 2002] indicates the elevation and snow volume distributions match quite closely. The highest *ADI* scores (i.e. poorest fit) were found in BCW (13%) and RCEW (6%) and indicate that the elevation-area distributions in these two CZO's do not predict snow storage as accurately (Figure 3). Nonetheless, the generally low *ADI* scores demonstrate that a catchment's hypsometry is a robust indicator of the elevations where the greatest snow volumes are stored and that hypsometry is useful for understanding the area/extent of a watershed likely to experience reductions in snow storage caused by warming.

While these results stress the importance of elevation in understanding the spatial distribution of snowpack, the higher *ADI* scores of BCW (13%) and RCEW (6%) indicate that factors beyond elevation are important in controlling snowpack. Previous research highlighting the importance of aspect and vegetation in modifying spatial patterns of

snow accumulation [Anderson *et al.*, 2014; Gustafson *et al.*, 2010; Jost *et al.*, 2007; Rinehart *et al.*, 2008; Veatch *et al.*, 2009] motivated us to evaluate the consistency and magnitude of influence of these variables on snow depths.

4.5.3 Aspect-dependent snow depths in forested and open terrain

ANOVA results indicate that mean snow depths are significantly different when grouped by 90° aspect quadrants or by vegetation height (alpine, forest, or shrubland) for all CZOs (Figure 5; SI Tables S1 - S5). Furthermore, the interaction of aspect and vegetation height is significant at each CZO, indicating that the influence of aspect on mean snow depth varies across alpine, forest, and shrubland areas (SI Tables S1 - S5). While all sites have significantly different mean snow depths between aspect or vegetation height groups, the roles and magnitude of these effects vary with CZO. The most consistent trends are greater snow depths on north-facing aspects and in alpine and shrubland zones (Figure 5). Below we discuss site-specific differences in aspect-and vegetation height-dependent snow depths and possible drivers for the observed patterns.

4.5.3.1 BCW aspect- and vegetation height-dependent snow depths

Snow depths across all aspects are greatest in the alpine zone of BCW which is comprised of the highest elevations where precipitation amounts and the length of the accumulation season are greatest. Variability in aspect-dependent snow depths is greatest in the alpine zone where northeast and southeast aspects exhibit as much as two times greater snow depths than northwest or southwest aspects (Figure 5a). The much greater mean snow depths on northeast and southeast slopes in the alpine zone indicate that redistribution of snow from western to eastern slopes by consistent high westerly winds (Knowles *et al.*, in press) is an important control on the spatial distribution of snow

depths in the alpine zone. Furthermore, inspection of snow depths across vegetation classes indicates that the strong aspect-dependent snow storage is limited to the alpine zone; mean snow depths in forest and shrubland zones are much less variable (Figure 5a). In fact, only the mean snow depths for northeast and northwest aspects in shrubland areas exhibit significant differences from south-facing snow depths in forested areas. These results emphasize the importance of wind and forest cover; southeast aspects in the alpine zone can store nearly as much snow as northeast aspects and forest and shrubland cover can mask the influence of aspect-dependent snow storage (Figure 5a).

4.5.3.2 JRB aspect- and vegetation height-dependent snow depths

Like BCW, JRB is located in the southern Rockies ecoregion in a high mountain continental setting (Figure 1). However, JRB does not reach as high of elevations as BCW and lacks an alpine zone (Figure 2f). JRB exhibits the some of the greatest differences in aspect-dependent snow depths both in forest and shrubland areas. North-facing aspects across vegetation classes have mean snow depths that are as much as one and a half times those on south-facing aspects (Figure 5b). Within areas of low vegetation (i.e. shrubland), the role of aspect is even stronger; southeast facing slopes have a mean snow depth that is ~ 100 mm greater than southwest slopes (Figure 5b, shrubland). Mean snow depths on north-facing slopes in both forest and shrubland do not exhibit statistically significant differences (Figure 5b). Results from JRB highlight the importance of snow storage on northern slopes in a high mountain, continental setting with the lowest latitude of the CZOs in this study (Figures 1 and 5b).

4.5.3.3 RCEW aspect- and vegetation height-dependent snow depths

RCEW displays the most striking departure in vegetation height-dependent snow depths; snow depths across all aspects in forested areas have much greater means than in shrubland areas (Figure 5c). Differences in the means between forested and shrubland snow depths range from more than two and a half times greater (northeast shrubland vs. southwest forested) up to seven times greater (southwest shrubland vs. northeast forested; Figure 5c). While the strongest differences in mean snow depth are related to vegetation height, RCEW also exhibits aspect-dependent controls. Mean snow depths on northeast- and southeast-facing aspects are generally higher than on northwest- or southwest-facing slopes (Figure 5c). Winds in RCEW are routinely out of the west to southwest and cause preferential deposition of wind transported snow in sheltered, NE- and SE-facing aspects [Winstral and Marks, 2002; Winstral et al., 2013]. Winstral et al. [2013] and Winstral and Marks [2002] used detailed field observations and a mass- and energy-balance snow model to demonstrate that wind is an important driver influencing the spatial patterns of snow accumulation at scales from $< 1 \text{ km}^2$ up to 14 km^2 in sub-catchments of RCEW. The much higher means for forest- and aspect-dependent snow groups observed in this study coupled with the findings of Winstral et al. [2013] and Winstral and Marks [2002] suggest that wind transport and preferential deposition of snow in sheltered areas can play an important role in controlling spatial patterns of snow accumulation at the scale of the upper RCEW (75 km^2). Furthermore, the aspect snow depth pattern observed in RCEW is similar to that of BCW's alpine zone and implies that areas with patchy or alpine vegetation cover are conducive to fetch-generation and transport of snow by wind.

4.5.3.4 KREW and WOLV aspect- and vegetation height-dependent snow depths

Northeast and northwest aspects in the alpine zones of KREW and WOLV have the highest mean snow depths (Figure 5d and e). At both sites, northern aspects in the alpine zones have mean snow depths that can be up to 1000 mm greater than mean snow depths on southern aspects. WOLV has the greatest aspect-driven differences in snow depth in its alpine zone; all aspects exhibit statistically significant differences (Figure 5e). A similar trend is observable in WOLV's forest and shrubland areas where northern aspects have mean snow depths that are greater than ones on southern aspects. Mean snow depths on southwest slopes in forest and shrubland areas of WOLV are higher (although not statistically significant) and indicate that west-to-east rain shadow effects could be important in controlling snow depths over relatively small spatial scales ($< 59 \text{ km}^2$). The aspect-dependent differences in snow depth observed in WOLV are not as strong in KREW; snow depths on northeast aspects with forest and shrubland areas are the only ones that tend to be significantly higher than other aspects (Figure 5d). Differences in the characteristics of aspect-dependent snow storage of KREW and WOLV and their relatively small separation distance ($\sim 64 \text{ km}$) suggest that topographic controls on snow depths can be important even when synoptic-scale weather patterns are generally similar.

4.6 Conclusions

We used LiDAR-derived observations of snow depth from five mountainous critical zone sites with different topographic, climatic, and vegetation characteristics to explore how elevation, vegetation, and aspect influence seasonal patterns of snow accumulation. Elevation, wind, radiation, and snow-vegetation interactions influence seasonal snow accumulations differently across the sites. Hypsometry was found to be a good, coarse

predictor of where the greatest volumes of snowpack storage occur at most sites, but as illustrated by RCEW and BCW, the interactions of wind transport, vegetation, and aspect can play a disproportionate role in determining snow accumulation over large areas (10's - 100's km²). These results offer insights into the processes driving seasonal snow accumulation across a broad range of hydroclimatic and topographic settings and have implications for resource management and studies of critical zone processes.

4.7 Acknowledgements

This work was supported by NSF RC CZO Cooperative Agreement # EAR 1331872 and USDA ARS and a NSF CZO SAVI Award # 1445246. LiDAR data were collected by NCALM under awards EAR-0922307 (Jemez), EPS-0447689 (Reynolds), EAR-0922307 (Sierra). The work presented here benefited from numerous conversations with Adrian Harpold of University of Nevada at Reno.

4.8 Figures

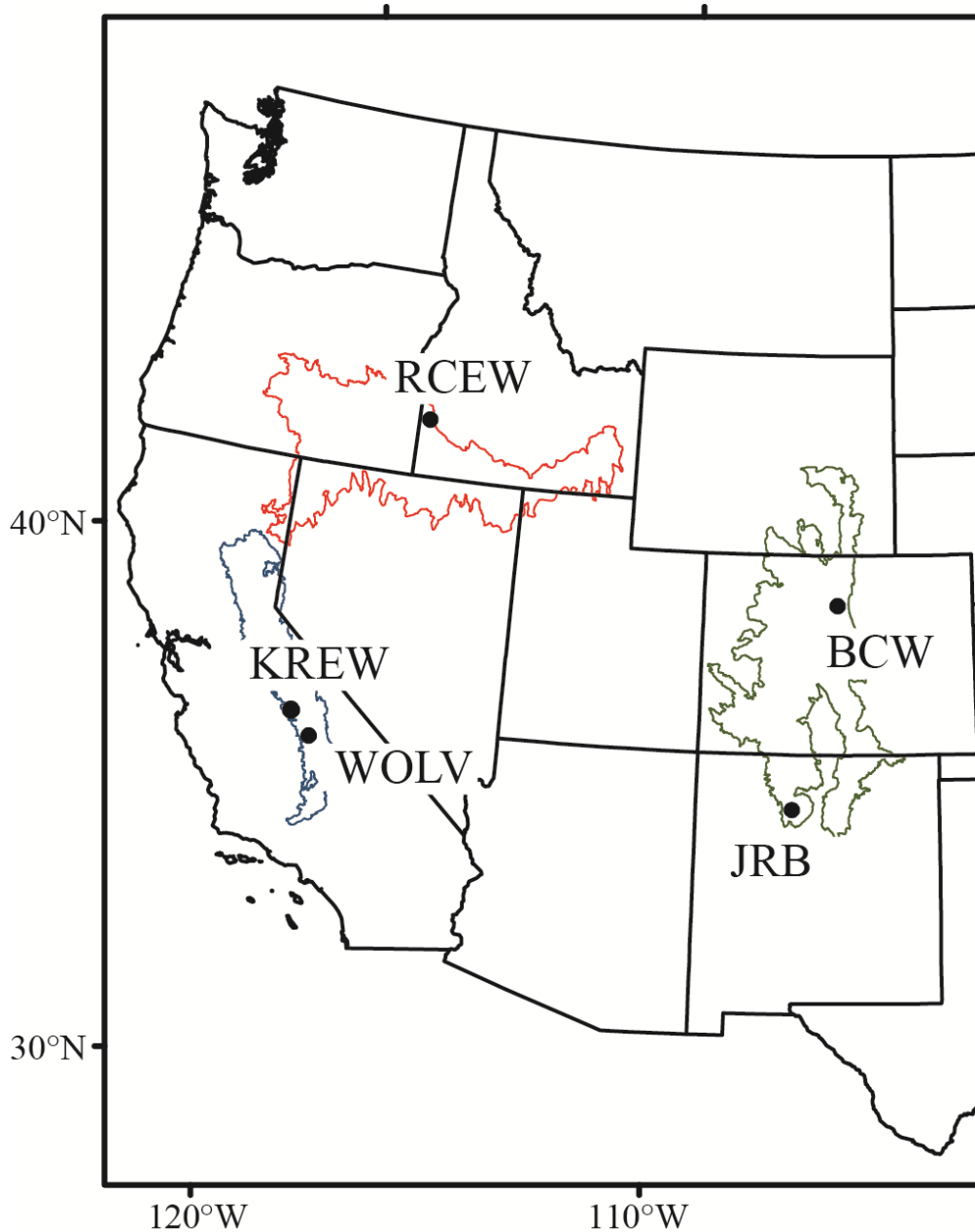


Figure 4.1. Locations of critical zone observatories: Boulder Creek Watershed (BCW), Jemez River Basin (JRB), Reynolds Creek Watershed (RCEW), Kings River Experimental Watershed (KREW), and Wolverton Basin (WOLV). Basins fall within U.S. EPA Level-III boundaries for the Southern Rockies (green outline), Northern Basin and Range (red outline) and Sierra Nevada (blue outline) ecoregions. Ecoregion delineations from the *Commission for Environmental Cooperation* [2009].

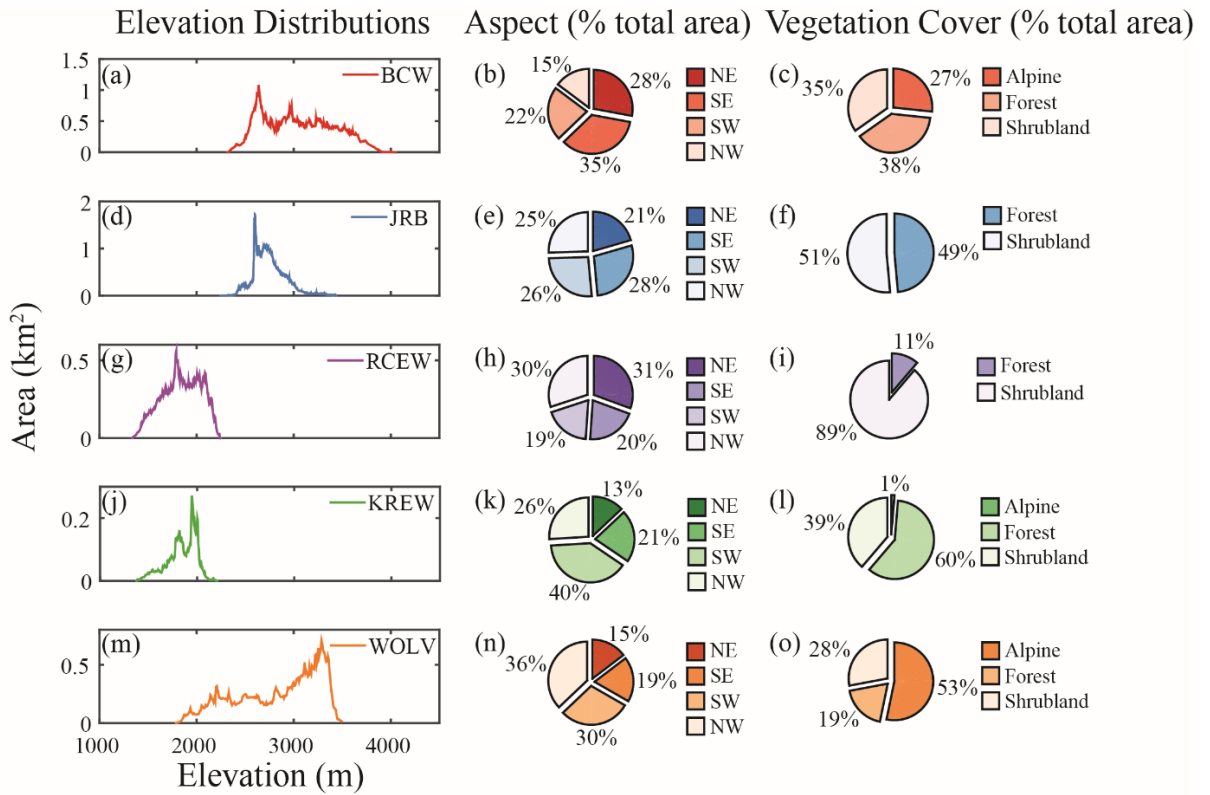


Figure 4.2. Elevation-area relationships, aspect proportions, and vegetation cover proportions for the snow-covered extents of Boulder (BCW), Jemez (JRB), Reynolds (RCEW), King’s (KREW), and Wolverton (WOLV) study areas. Aspect is binned into 90° quadrants: NE (0° to 90°), SE (90° to 180°), SW (180° to 270°), and NW (270° to 360°). Vegetation cover is classified as shrubland (vegetation height < 2m), forest (vegetation height > 2m), and alpine (areas above the elevation where vegetation heights are continuously < 2m). Note that the elevation distributions and aspect and vegetation characteristics vary for each of the snow-covered extents at these critical zone observatories.

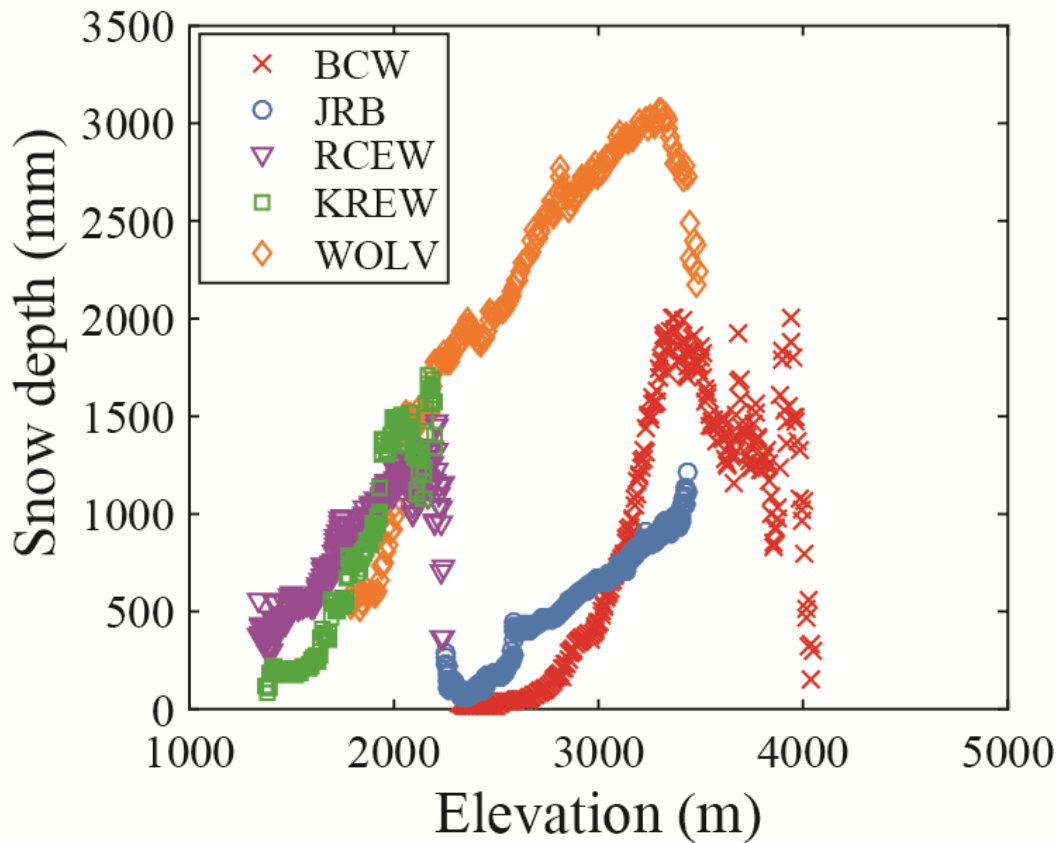


Figure 4.3. Average snow depth plotted against binned elevations for the CZOs. Note that the forms of the snow depth-elevation relationships and their rates of increase vary with CZO. Also note that not all of the CZOs, except JRB and KREW, exhibit decreases in snow depth at their highest elevations. For those that do, there are variations in the forms and rates of decrease.

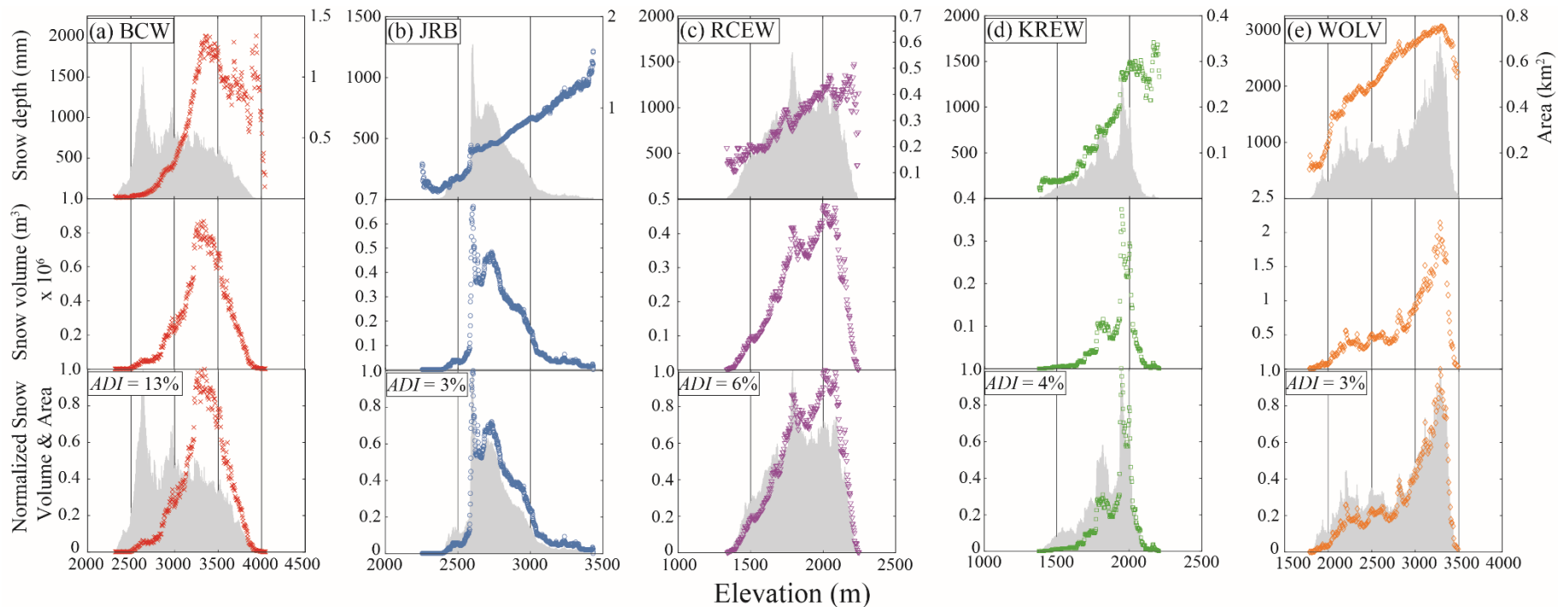


Figure 4.4. Top row is snow depth (colored symbols) and area (gray shading), middle row is snow volume, and bottom row is normalized snow volume (colored symbols) and area (gray shading) plotted against elevation for sites at (a) Boulder (BCW), (b) Jemez (JRB), (c) Reynolds (RCEW), (d) King's (KREW) and (e) Wolverton (WOLV). The elevation and snow volume distributions generally match with exceptions at BCW and RCEW. The Agresti Dissimilarity Index (*ADI*) is the smallest percentage of the CZO snow volume distribution that needs to be reallocated to match the elevation distribution; a score of 0% indicates a perfect match between distributions.

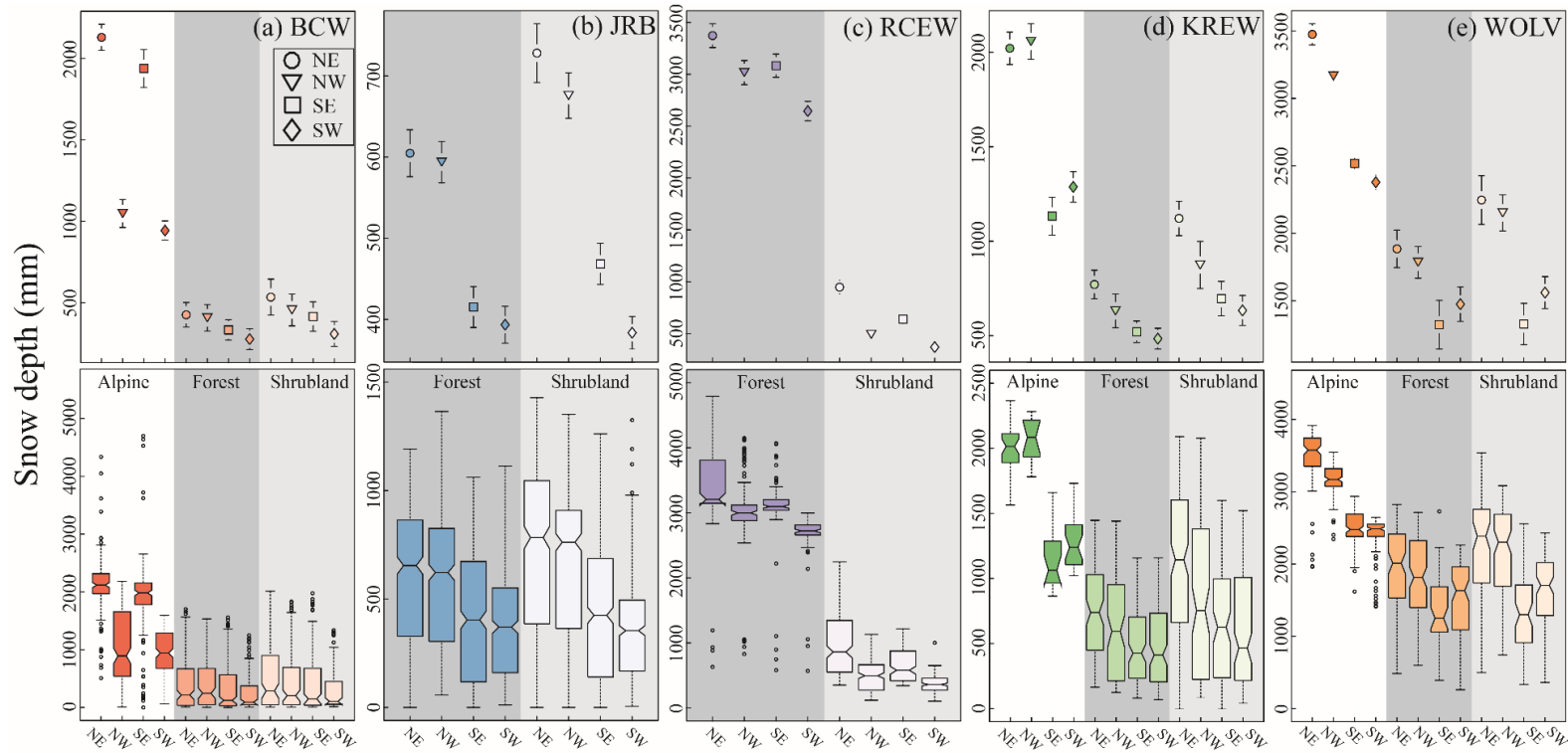


Figure 4.5. Comparison of aspect-dependent snow depths in alpine (white background), forested (dark gray shading), and shrubland (light gray shading) areas for (a) Boulder (BCW), (b) Jemez (JRB), (c) Reynolds (RCEW), (d) King’s (KREW) and (e) Wolverton (WOLV) sites. The top row shows mean snow depths (symbols) and 95% confidence intervals (vertical lines) based on the results of a Tukey’s HSD test. If the confidence intervals between two means do not overlap the groups’ means are significantly different. The bottom row shows boxplots of group snow depths. The notches on the boxplots extend to $\pm 1.58(\text{inter-quartile range}/\text{square root}(n))$, and provide an additional, non-parametric test for significant differences in central tendencies of the groups. If the notches do not overlap the medians can be considered significantly different [Chambers *et al.*, 1983].

4.9 References

- Anderson, B. T., J. P. McNamara, H. P. Marshall, and A. N. Flores (2014), Insights into the physical processes controlling correlations between snow distribution and terrain properties, *Water Resources Research*, 50(6), 4545-4563.
- Anderson, S.P., Qinghua, G., and Parrish, E.G., 2012, Snow-on and snow-off LiDAR point cloud data and digital elevation models for study of topography, snow, ecosystems and environmental change at Southern Sierra Critical Zone Observatory, California: Southern Sierra CZO, University of California at Merced , digital media.
- Berghuijs, W. R., R. A. Woods, and M. Hrachowitz (2014), A precipitation shift from snow towards rain leads to a decrease in streamflow, *Nature Climate Change*, 4(7), 583-586.
- Biederman, J. A., P. D. Brooks, A. A. Harpold, D. J. Gochis, E. Gutmann, D. E. Reed, E. Pendall, and B. E. Ewers (2014), Multiscale observations of snow accumulation and peak snowpack following widespread, insect-induced lodgepole pine mortality, *Ecohydrology*, 7(1), 150-162.
- Breslow, N. (1970), A generalized Kruskal-Wallis test for comparing K samples subject to unequal patterns of censorship, *Biometrika*, 57(3), 579-594.
- Brooks, P. D., P. Grogan, P. H. Templer, P. Groffman, M. G. Öquist, and J. Schimel (2011), Carbon and Nitrogen Cycling in Snow-Covered Environments, *Geography Compass*, 5(9), 682-699.
- Deems, J. S., T. H. Painter, and D. C. Finnegan (2013), Lidar measurement of snow depth: a review, *Journal of Glaciology*, 59(215), 467-479.

- Dunn, O. J. (1964), Multiple comparisons using rank sums, *Technometrics*, 6(3), 241-252.
- Freedman, D., and P. Diaconis (1981), On the histogram as a density estimator: L 2 theory, *Probability theory and related fields*, 57(4), 453-476.
- Giroto, M., G. Cortes, S. A. Margulis, and M. Durand (2014), Examining spatial and temporal variability in snow water equivalent using a 27 year reanalysis: Kern River watershed, Sierra Nevada, *Water Resources Research*, 50(8), 6713-6734.
- Glenn, Nancy. 2009. LiDAR-derived Snow-on Digital Elevation Model of Reynolds Creek Experimental Watershed LiDAR (1 meter). Boise State University, Boise Aerospace Center Laboratory. Boise, ID.
https://data.boisestate.edu/arcgis/rest/services/CZO/RCEW_DEM_2009_1m/ImageServer
- Godsey, S., J. Kirchner, and C. Tague (2013), Effects of changes in winter snowpacks on summer low flows: case studies in the Sierra Nevada, California, USA, *Hydrological Processes*.
- Guo, Qinghua, Jon Pelletier, Matej Durcik (2010). "CZO Dataset: Jemez River Basin - LiDAR (2010) - Snow-on." Retrieved 04 Aug 2015, from <http://criticalzone.org/national/data/dataset/2612/>.
- Guo, Qinghua, Roger Bales, 2012, Snow-on and snow-off LiDAR point cloud data and digital elevation models for study of topography, snow, ecosystems and environmental change at Southern Sierra Critical Zone Observatory, California: Southern Sierra CZO, University of California at Merced, digital media.

- Gustafson, J. R., P. D. Brooks, N. P. Molotch, and W. C. Veatch (2010), Estimating snow sublimation using natural chemical and isotopic tracers across a gradient of solar radiation, *Water Resources Research*, 46.
- Harpold, A. A., et al. (2014), LiDAR-derived snowpack data sets from mixed conifer forests across the Western United States, *Water Resources Research*, 50(3), 2749-2755.
- Hopkinson, C., M. Sitar, L. Chasmer, and P. Treitz (2004), Mapping snowpack depth beneath forest canopies using airborne lidar, *Photogrammetric Engineering and Remote Sensing*, 70(3), 323-330.
- Jost, G., M. Weiler, D. R. Gluns, and Y. Alila (2007), The influence of forest and topography on snow accumulation and melt at the watershed-scale, *Journal of Hydrology*, 347(1-2), 101-115.
- Kirchner, J. W. (2006), Getting the right answers for the right reasons: Linking measurements, analyses, and models to advance the science of hydrology, *Water Resources Research*, 42(3), 5.
- Kirchner, P. B., R. C. Bales, N. P. Molotch, J. Flanagan, and Q. Guo (2014), LiDAR measurement of seasonal snow accumulation along an elevation gradient in the southern Sierra Nevada, California, *Hydrology and Earth System Sciences*, 18(10), 4261-4275.
- Link, T. E., and D. Marks (1999), Point simulation of seasonal snow cover dynamics beneath boreal forest canopies, *Journal of Geophysical Research-Atmospheres*, 104(D22), 27841-27857.

- Monson, R. K., A. A. Turnipseed, J. P. Sparks, P. C. Harley, L. E. Scott-Denton, K. Sparks, and T. E. Huxman (2002), Carbon sequestration in a high-elevation, subalpine forest, *Global Change Biology*, 8(5), 459-478.
- Pomeroy, J. W., D. Marks, T. Link, C. Ellis, J. Hardy, A. Rowlands, and R. Granger (2009), The impact of coniferous forest temperature on incoming longwave radiation to melting snow, *Hydrological Processes*, 23(17), 2513-2525.
- Rinehart, A. J., E. R. Vivoni, and P. D. Brooks (2008), Effects of vegetation, albedo, and solar radiation sheltering on the distribution of snow in the Valles Caldera, New Mexico, *Ecohydrology*, 1(3), 253-270.
- Roe, G. H. (2005), Orographic precipitation, in *Annual Review of Earth and Planetary Sciences*, edited, pp. 645-671, Annual Reviews, Palo Alto.
- Seager, R., M. F. Ting, C. H. Li, N. Naik, B. Cook, J. Nakamura, and H. B. Liu (2013), Projections of declining surface-water availability for the southwestern United States, *Nature Climate Change*, 3(5), 482-486.
- Stewart, I. T. (2009), Changes in snowpack and snowmelt runoff for key mountain regions, *Hydrological Processes*, 23(1), 78-94.
- Stewart, I. T., D. R. Cayan, and M. D. Dettinger (2005), Changes toward earlier streamflow timing across western North America, *Journal of Climate*, 18(8), 1136-1155.
- Stielstra, C. M., K. A. Lohse, J. Chorover, J. C. McIntosh, G. A. Barron-Gafford, J. N. Perdrial, M. Litvak, H. R. Barnard, and P. D. Brooks (2015), Climatic and landscape influences on soil moisture are primary determinants of soil carbon fluxes in seasonally snow-covered forest ecosystems, *Biogeochemistry*, 123(3), 447-465.

- Tinkham, W. T., A. M. S. Smith, H. P. Marshall, T. E. Link, M. J. Falkowski, and A. H. Winstral (2014), Quantifying spatial distribution of snow depth errors from LiDAR using Random Forest, *Remote Sensing of Environment*, 141, 105-115.
- Trujillo, E., and N. P. Molotch (2014), Snowpack regimes of the Western United States, *Water Resources Research*, 50(7), 5611-5623.
- Trujillo, E., N. P. Molotch, M. L. Goulden, A. E. Kelly, and R. C. Bales (2012), Elevation-dependent influence of snow accumulation on forest greening, *Nature Geoscience*, 5(10), 705-709.
- Veatch, W., P. D. Brooks, J. R. Gustafson, and N. P. Molotch (2009), 'Quantifying the effects of forest canopy cover on net snow accumulation at a continental, mid-latitude site', *Ecohydrology*, 2(2), 115-128.
- Winstral, A., and D. Marks (2002), Simulating wind fields and snow redistribution using terrain based parameters to model snow accumulation and melt over a semi-arid mountain catchment, *Hydrological Processes*, 16(18), 3585-3603.
- Winstral, A., D. Marks, and R. Gurney (2013), Simulating wind-affected snow accumulations at catchment to basin scales, *Advances in Water Resources*, 55, 64-79.

5 Appendix 1

Supporting Information for

A simple framework for assessing the sensitivity of mountain watersheds to warming driven snowpack loss

Christopher J. Tennant¹, Benjamin T. Crosby¹, Sarah E. Godsey¹, Robert W. VanKirk² and DeWayne R. Derryberry³

¹ Department of Geosciences, Idaho State University, 921 South 8th Ave. Stop 8072, Pocatello, ID 83209-8072, USA, ² Henry's Fork Foundation, P.O. Box 550, Ashton, ID, 83420, USA and

Department of Mathematics, Humboldt State University, 1 Harpst St., Arcata, CA, 95521, USA, ³ Department of Mathematics, Idaho State University, 921 South 8th Ave. Stop 8150, Pocatello, ID 83209-8150, USA



Figure S1: Sampled watersheds from the northern Rocky Mountains, USA. The white outline shows the area used to characterize the relationship between peak SWE and elevation as well as land cover classifications (SI Figure 5). The Snake River Plain of south central Idaho was omitted because it does not accumulate significant snow cover. Catchment boundaries were designated using the 12-digit hydrologic units from the national Watershed Boundary Dataset (U.S. Geological Survey and U.S. Department of Agriculture, 2013). Elevations for watersheds were extracted from a 30 m digital elevation model from the National Elevation Dataset [Gesch *et al.*, 2002] and exported to R and MATLAB for characterization.

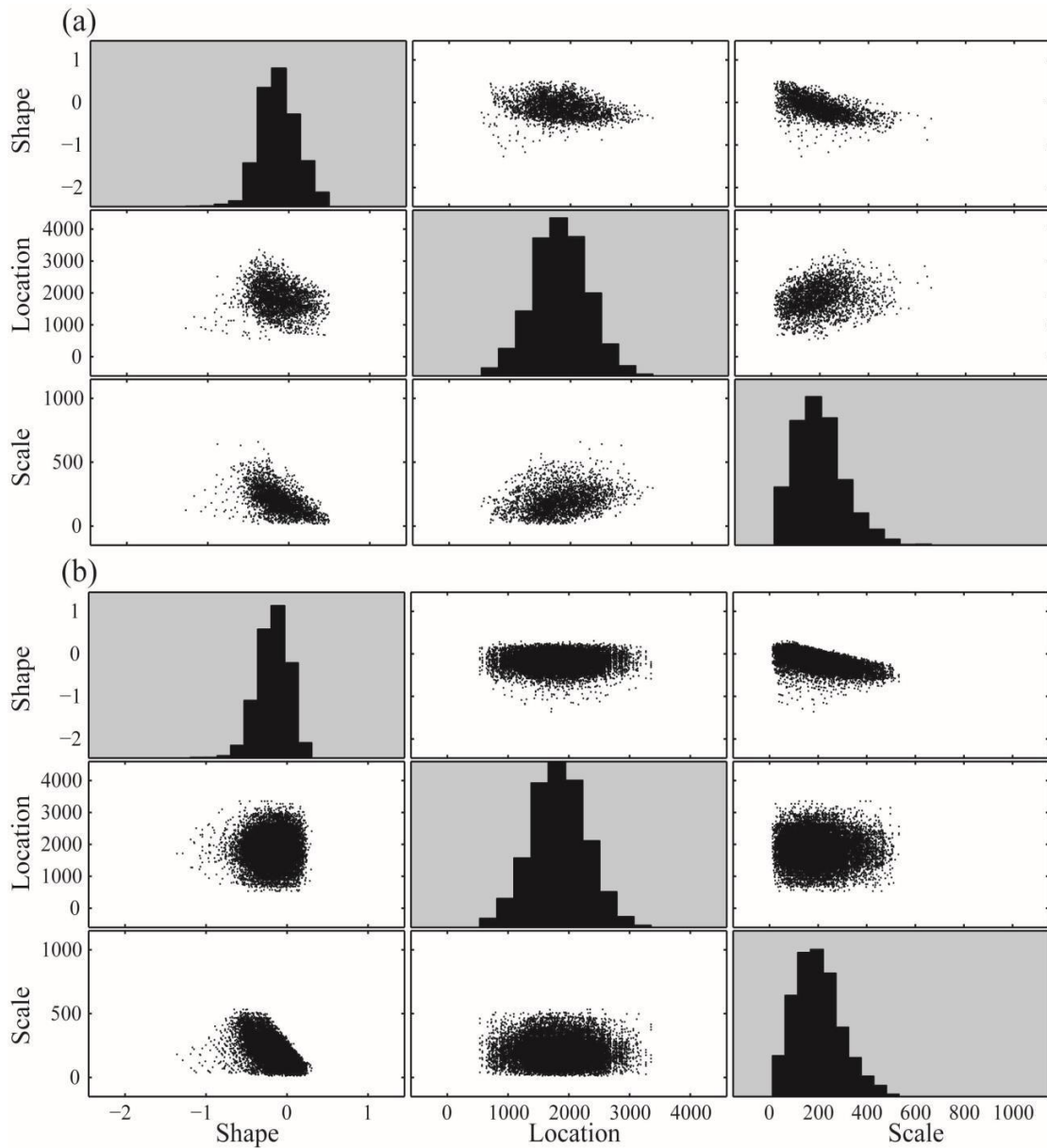


Figure S2: Scatterplot matrices of estimated GEV parameters (shape, location, and scale) for (a) northern Rockies watersheds ($n = 3,175$) and (b) 20,000 Monte Carlo simulated watershed elevation distributions. The main diagonals (grey background) show normalized histograms (y-axis, 0 – 100%) for the GEV parameters (shape, location, and scale). Normalized histograms are provided to compare distributions between northern Rockies and Monte Carlo simulated watershed elevation distributions. Location is neither correlated with scale nor shape.

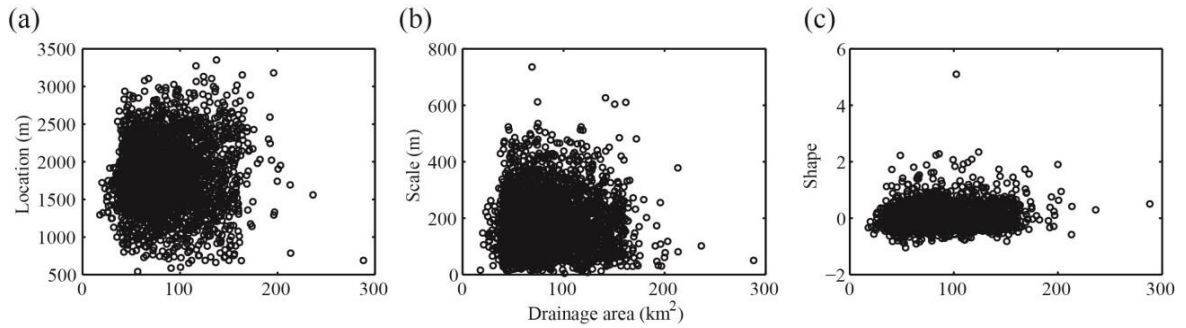


Figure S3: GEV parameters location (a), scale (b), and shape (c) from watersheds in the northern Rocky Mountains plotted against their respective drainage areas. Note that GEV parameters are not correlated with drainage area.

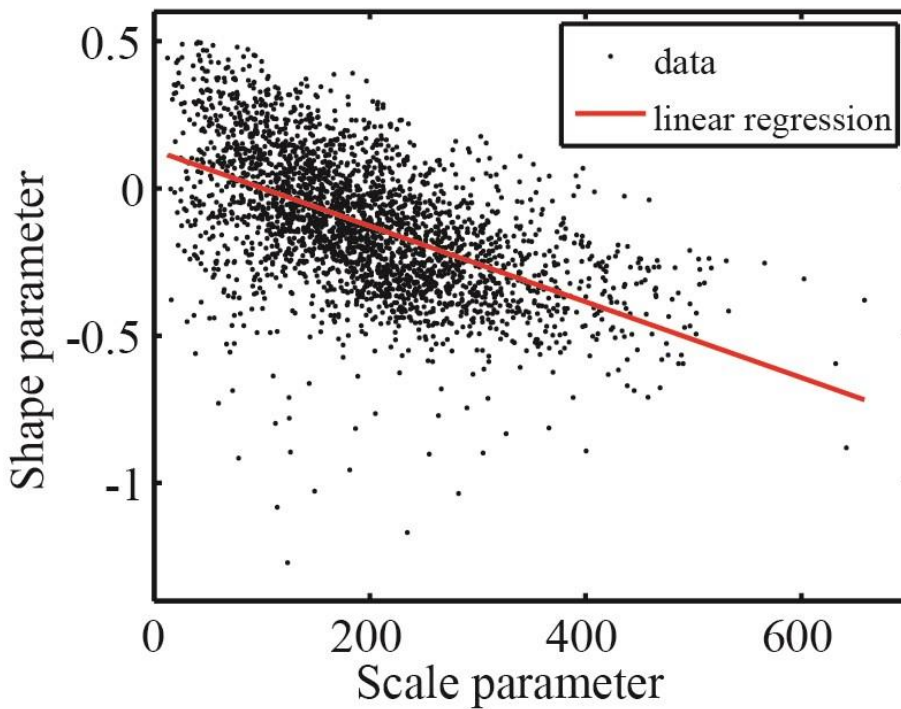


Figure S4: Negative correlation between the shape and scale parameters of the generalized extreme value (GEV) distribution for northern Rocky Mountain watersheds. From this data, we developed a regression equation that has the form $shape = -0.00013(scale) + 0.1299 + \varepsilon$ (statistics: $R^2 = 0.32$, p-value = $2.2e-16$, degrees of freedom = 2783, and the residual standard error is 0.1902). For the Monte Carlo simulations, we add ε to the linear regression which is the product of a random value from the standard normal distribution (mean = 0, standard deviation = 1) and the residual error from the regression. This error term (ε) was added so our simulations captured the observed covariance between the scale and shape parameters for the northern Rocky Mountain watersheds. Scatter plots and histograms of the observed and simulated watershed elevation distributions are shown in SI Figure 3.

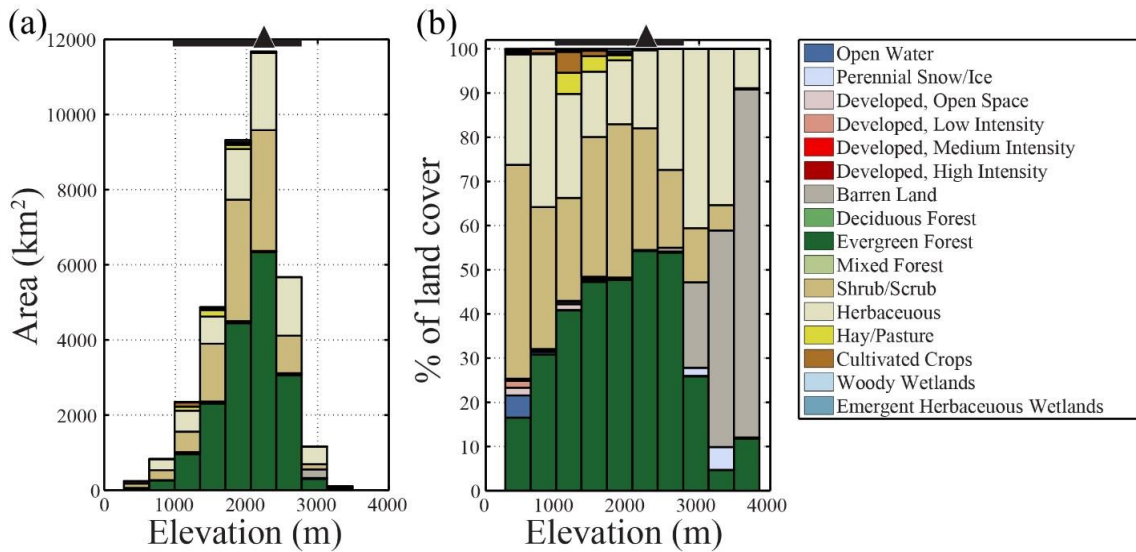


Figure S5: Elevation-area histogram (a) for the region used to characterize the relationship between peak snow water equivalent (SWE) and elevation (white outline in SI Figure 1). Histogram bins are colored by land cover type. Stacked bar plot (b) of percent of land cover type across the range of elevations used to characterize the relationship between peak snow water equivalent and elevation. Evergreen forests compose the majority of the land area (17,738 km²) in the region used for the SWE-elevation characterization (SI Figure 1). The thick horizontal lines shows the range of elevations (990 – 2776 m) where evergreen forest are the dominant land cover type and the triangle shows the midpoint (2240 m) of the elevation bin where evergreen forests reach their maximum percent cover. For a complete description of land cover types and classification techniques, see *Jin et al.* [2013].

Land Cover Class	Range of Elevations (m)									
	276 - 633	633 - 990	990 - 1347	1347 - 1704	1704 - 2062	2062 - 2419	2419 - 2776	2776 - 3133	3133 - 3490	3490 - 3847
Open Water (%)	5.02	0.58	0.13	0.10	0.12	0.13	0.17	0.15	0.06	0.00
Perennial Snow/Ice (%)	0.00	0.00	0.00	0.00	0.00	0.00	0.08	1.82	5.17	0.25
Developed, Open Space (%)	1.78	0.31	1.28	0.46	0.22	0.03	0.00	0.00	0.00	0.00
Developed, Low Intensity (%)	1.57	0.23	0.55	0.37	0.14	0.01	0.00	0.00	0.00	0.00
Developed, Medium Intensity (%)	0.32	0.04	0.11	0.16	0.07	0.00	0.00	0.00	0.00	0.00
Developed, High Intensity (%)	0.00	0.00	0.01	0.00	0.00	0.00	0.00	0.00	0.00	0.00
Barren Land (%)	0.02	0.01	0.03	0.03	0.03	0.06	0.86	19.32	49.01	78.78
Deciduous Forest (%)	0.09	0.05	0.05	0.07	0.01	0.00	0.00	0.00	0.00	0.00
Evergreen Forest (%)	16.53	30.83	40.78	47.24	47.64	54.26	53.86	25.87	4.67	11.80
Mixed Forest (%)	0.00	0.00	0.00	0.00	0.01	0.00	0.00	0.00	0.00	0.00
Shrub/Scrub (%)	48.40	32.15	23.31	31.59	34.70	27.53	17.61	12.24	5.72	0.28
Herbaceous (%)	24.97	34.58	23.55	14.81	14.47	17.66	27.39	40.58	35.38	8.90
Hay/Pasture (%)	0.43	0.24	4.78	3.53	1.17	0.05	0.00	0.00	0.00	0.00
Cultivated Crops (%)	0.23	0.95	4.71	1.18	0.31	0.00	0.00	0.00	0.00	0.00
Woody Wetlands (%)	0.37	0.02	0.36	0.41	0.49	0.10	0.01	0.00	0.00	0.00
Emergent Herbaceous Wetlands (%)	0.26	0.01	0.35	0.04	0.61	0.17	0.02	0.01	0.00	0.00

Table S1: Percentages of land cover classes binned by elevation (see section 2.5 in manuscript for methods) for the region used to characterize the relationship between peak SWE and elevation (SI Figure 1). Values highlighted in grey show the maximum land cover type for a given elevation bin.

Warming amount (°C) Bayesian Information Criterion (BIC) selected regression for peak SWE loss

+ 1	$SWE_{loss} = location + scale + shape + location^2 + shape^2 + location^3 + scale \cdot shape + location^2 \cdot scale^2$
+ 2	$SWE_{loss} = location + scale + shape + location^2 + location^3 + location \cdot scale^2 + scale \cdot shape + location^2 \cdot scale^2$
+ 3	$SWE_{loss} = location + scale + shape + location^2 + location^3 + location \cdot scale^2 + scale \cdot shape + location^2 \cdot scale^2$
+ 4	$SWE_{loss} = location + scale + shape + location^2 + location \cdot scale + location^3 + location \cdot scale^2 + scale \cdot location^2$
+ 5	$SWE_{loss} = location + scale + shape + location^2 + location \cdot scale + location^3 + location \cdot shape^2 + scale \cdot location^2$

Table S2: Peak SWE loss regression equations selected by the Bayesian Information Criterion (BIC) for each degree of warming. Each regression was selected using an exhaustive search algorithm of generalized extreme value (GEV) predictor variables up to third order interactions. The order of terms does not reflect their relative influence. The predictor and response variables were standardized to facilitate comparison of the importance between lower and higher order predictors. Predictor coefficient estimates and regression statistics are provided for each regression in SI Table 3 below.

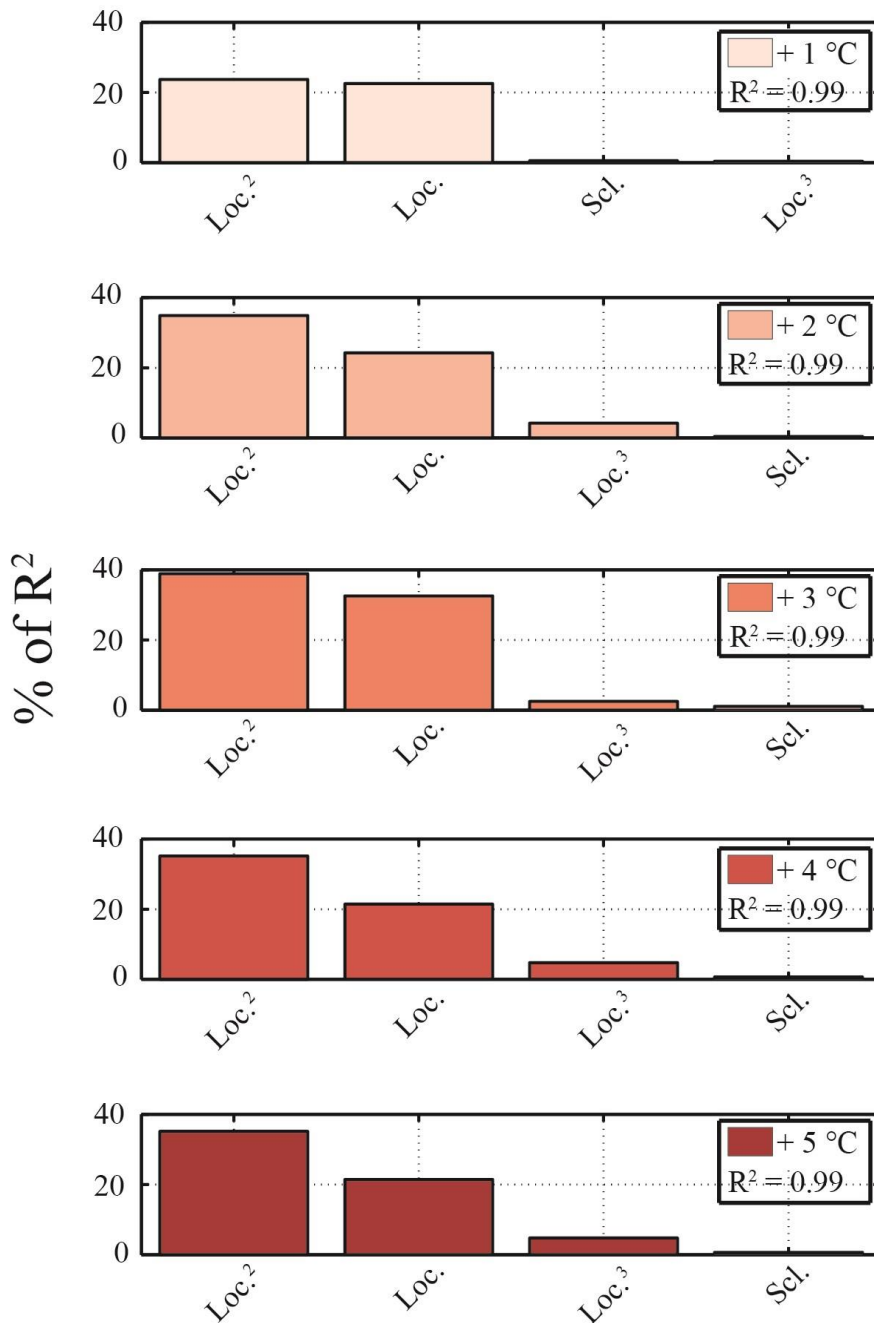


Figure S6: Relative importance of regression predictors (SI Table 1) for peak SWE loss at each warming scenario as determined using sequential R^2 values (see Grömping (2006), method 'lmg' for details). Figure only includes predictors (SI Table 1) that explain $> 1\%$ of the variation in peak SWE loss. The regression coefficient location² explains most of the variance for warming responses $+2^\circ$ to $+5^\circ\text{C}$. The increase in importance of the regressors location² and location³ for warming amounts $+2^\circ$ to $+5^\circ\text{C}$ indicates that the pattern of peak SWE loss becomes increasing non-linear as warming proceeds.

Peak SWE loss regression coefficient estimates and statistics (+ 1° to + 5°C)

+ 1°C	<i>Estimate</i>	<i>Standard Error</i>	<i>t value</i>	<i>p value</i>
(Intercept)	-0.84168	0.002214	-380.16	<2e-16
<i>location</i> ²	-8.16536	0.018148	-449.93	<2e-16
<i>location</i>	6.857705	0.0172933	396.55	<2e-16
<i>location</i> ³	0.839707	0.0021363	393.06	<2e-16
<i>scale</i>	-0.12967	0.0006807	-190.5	<2e-16
<i>shape</i>	-0.07985	0.0009277	-86.08	<2e-16
<i>location</i> ² · <i>scale</i> ²	0.046601	0.0005496	84.79	<2e-16
<i>scale</i> · <i>shape</i>	-0.02424	0.0007012	-34.57	<2e-16
<i>shape</i> ²	-0.01516	0.0009614	-15.77	<2e-16

+ 2°C	<i>Estimate</i>	<i>Standard Error</i>	<i>t value</i>	<i>p value</i>
(Intercept)	-0.9404177	0.002191	-429.21	<2e-16
<i>location</i> ²	-9.4694299	0.017734	-533.98	<2e-16
<i>location</i>	8.1633889	0.016929	482.22	<2e-16
<i>location</i> ³	0.9449283	0.002137	442.25	<2e-16
<i>scale</i>	-0.1401967	0.000653	-214.7	<2e-16
<i>location</i> ² · <i>scale</i> ²	0.1230383	0.003136	39.23	<2e-16
<i>location</i> · <i>scale</i> ²	-0.0813732	0.003105	-26.21	<2e-16
<i>shape</i>	-0.0731193	0.000636	-114.98	<2e-16
<i>scale</i> · <i>shape</i>	-0.0159987	0.000498	-32.14	<2e-16

+ 3°C	<i>Estimate</i>	<i>Standard Error</i>	<i>t value</i>	<i>p value</i>
(Intercept)	-0.9628	0.0023	-412.36	<2e-16
<i>location</i> ²	-10.3300	0.0192	-537.18	<2e-16
<i>location</i>	8.9950	0.0183	492.55	<2e-16
<i>location</i> ³	0.9686	0.0023	425.95	<2e-16
<i>location</i> ² · <i>scale</i> ²	0.1596	0.0033	48.32	<2e-16
<i>scale</i>	-0.1545	0.0007	-217.05	<2e-16
<i>location</i> · <i>scale</i> ²	-0.1238	0.0033	-37.76	<2e-16
<i>shape</i>	-0.0758	0.0007	-108.72	<2e-16
<i>scale</i> · <i>shape</i>	-0.0140	0.0005	-25.69	<2e-16

+ 4°C	<i>Estimate</i>	<i>Standard Error</i>	<i>t value</i>	<i>p value</i>
(Intercept)	-0.9802	0.0026	-377.56	<2e-16
<i>location</i> ²	-11.2200	0.0216	-518.99	<2e-16
<i>location</i>	9.9540	0.0206	482.97	<2e-16
<i>location</i> ³	0.9933	0.0026	389.47	<2e-16
<i>location</i> · <i>scale</i>	-0.3047	0.0046	-66	<2e-16
<i>scale</i> · <i>location</i> ²	0.2666	0.0040	67.28	<2e-16
<i>scale</i>	-0.1588	0.0008	-208.4	<2e-16
<i>shape</i>	-0.0768	0.0008	-100.79	<2e-16
<i>location</i> · <i>scale</i> ²	0.0675	0.0022	31.03	<2e-16

+ 5°C	<i>Estimate</i>	<i>Standard Error</i>	<i>t value</i>	<i>p value</i>
(Intercept)	-0.9173	0.0034	-269.74	<2e-16
<i>location</i> ²	-11.5000	0.0282	-408.34	<2e-16
<i>location</i>	10.3700	0.0269	385.15	<2e-16
<i>location</i> ³	0.9297	0.0033	278.49	<2e-16
<i>scale</i> · <i>location</i> ²	0.3232	0.0051	63.3	<2e-16
<i>location</i> · <i>scale</i>	-0.3212	0.0051	-62.87	<2e-16
<i>scale</i>	-0.1767	0.0010	-174.75	<2e-16
<i>shape</i>	-0.0802	0.0010	-79.32	<2e-16
<i>location</i> · <i>shape</i> ²	0.0261	0.0009	28.56	<2e-16

Table S3: Peak SWE loss coefficient estimates and regression statistics for standardized generalized extreme value predictors for a range of warming (+ 1° to + 5°C). For all regressions, the residual standard errors were < 0.08, the adjusted R² values were > 0.99, the F-statistic values were > 10⁵, and the p-values < 0.0001. To compare the relative importance of different terms, see SI Figure 6.

References

- Gesch, D., M. Oimoen, S. Greenlee, C. Nelson, M. Steuck, and D. Tyler (2002), The national elevation dataset, *Photogrammetric engineering and remote sensing*, 68(1), 5-32.
- Grömping, Ulrike. Relative importance for linear regression in R: the package relaimpo. *Journal of statistical software* 17.1 (2006): 1-27.
- Jin, S., Yang, L., Danielson, P., Homer, C., Fry, J., and Xian, G. 2013. A comprehensive change detection method for updating the National Land Cover Database to circa 2011. *Remote Sensing of Environment*, 132: 159 – 175.
- U.S. Geological Survey and U.S. Department of Agriculture, N. R. C. S. (2013), *Federal Standards and Procedures for the National Watershed Boundary Dataset (WBD)* (4 ed.), edited, p. 63, U.S. Geological Survey Techniques and Methods 11-A3.

6 Appendix 2

Supporting Information for

Sensitivity of Rocky Mountain ecoregions to warming-driven snowpack loss

Christopher J. Tennant¹, Sarah E. Godsey¹, Benjamin T. Crosby¹, Robert W. VanKirk²
and DeWayne R. Derryberry³

¹ Department of Geosciences, Idaho State University, 921 South 8th Ave. Stop 8072, Pocatello, ID 83209-8072, USA, ² Henry's Fork Foundation, P.O. Box 550, Ashton, ID, 83420, USA and Department of Mathematics, Humboldt State University, 1 Harpst St., Arcata, CA, 95521, USA, ³ Department of Mathematics, Idaho State University, 921 South 8th Ave. Stop 8150, Pocatello, ID 83209-8150, USA

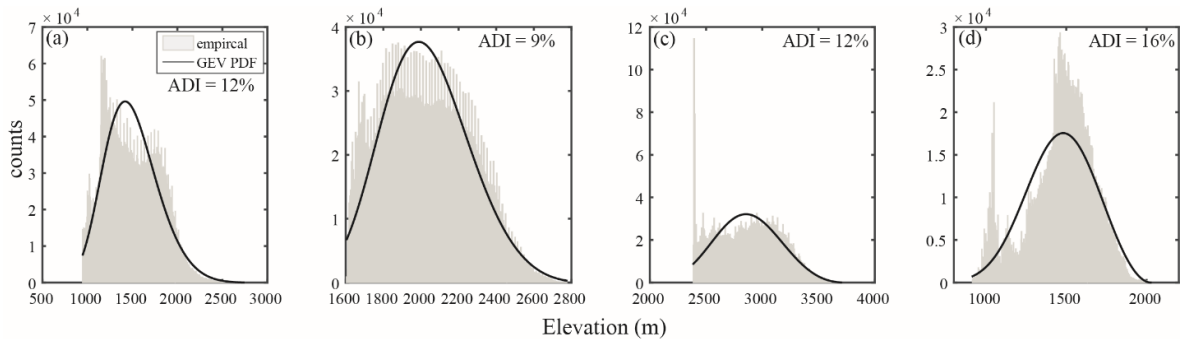


Figure S1: Agresti's dissimilarity index (ADI; eq. 2) for randomly selected HUC-10 watersheds from the (a) Canadian Rockies (HUC 1701020606), (b) Idaho Batholith (HUC 1704021905), (c) Middle Rockies (HUC 1007000101) and (d) Northern Rockies (HUC 1701021002) ecoregions (Figure 1). The black lines show the expected values from the generalized extreme value probability density function, where the generalized extreme value (GEV) location (μ), scale (σ), and shape (k) parameters determine the expected values (eq. 1). The histograms show the 10 m resolution elevation data for each catchment. The bin width of each histogram was set using the Freedman-Diaconis rule [Freedman and Diaconis, 1981].

ECOREGION	LINEAR FIT	R ²	P-VALUE
CANADIAN ROCKIES	$SWE_{pk} = 2164 - 0.62(elev)$	0.18	<0.0001
IDAHO BATHOLITH	$SWE_{pk} = 681 - 0.08(elev)$	0.10	<0.0001
MIDDLE ROCKIES	$SWE_{pk} = 1367 - 0.27(elev)$	0.29	<0.0001

Table S1: Linear fits for peak SWE-elevation relationship above change point elevation (see Figure 3 in manuscript). SWE_{pk} is the average annual peak SWE (mm) and $elev$ is a vector of elevations (m) that range from the turning point elevation to the maximum elevation within the respective ecoregions.

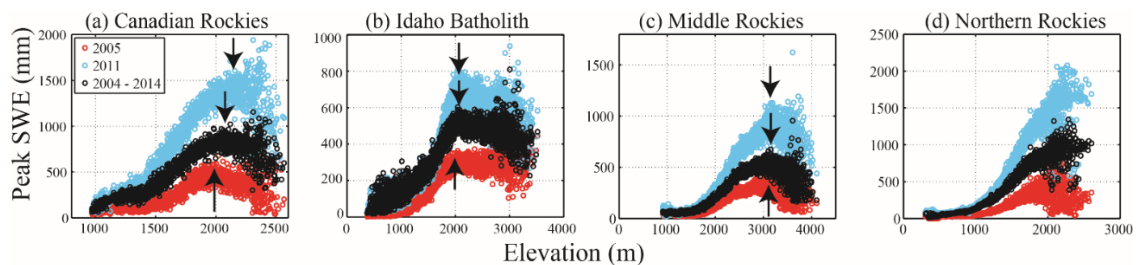


Figure S2: Peak SWE-elevation relationships for the (a) Canadian Rockies, (b) Idaho Batholith, (c) Middle Rockies, and (d) Northern Rockies for water years 2005 (red circles) and 2011 (blue circles) and the average across the 2004 – 2014 water years. The arrows point to the turning point locations (see section 3.2.2 for methods for identifying the turning point). The turning point elevations vary by (a) 150 m in the Canadian Rockies, (b) 60 m in the Idaho Batholith, and (c) 40 m for the Middle Rockies. The average annual peak SWE-elevation for (d) the Northern Rockies does not have a turning point elevation, even across the spread of water years. Analysis of mountain snowpack maps from the Natural Resources Conservation Service for the four ecoregions indicates that on average 1 April SWE was 35 % (2005) and 120 % (2011) of the 1981 – 2010 normal. Basin-wide, percent of normal snowpack maps can be found here, <http://www.wcc.nrcs.usda.gov/cgibin/westsnow.pl>.

Geographically Weighted Regressions (GWR)

All geographically weighted regressions were generated using the Spatial Analysis in Macroecology (SAM) software package [Rangel *et al.*, 2010]. All regressions took the following form; which is the generalized extreme value (GEV) specific version of eq. 6:

$$SWE_{pkLoss_i} = \beta_0(u_i, v_i) + \beta_j(u_i, v_i)\mu_j + \beta_j(u_i, v_i)\sigma_j + \beta_j(u_i, v_i)k_j + \varepsilon_i \quad (S4)$$

$$SWE_{pkLoss_i} = \beta_0 + \beta_1\mu_j + \beta_2\sigma_j + \beta_3k_j + \varepsilon_i \quad (S2)$$

where SWE_{pkLoss_i} is the average annual peak SWE loss for the i th HUC-10 watershed with centroid coordinates (u_i, v_i) for a given warming scenario (+1°C, +2°C, +3°C, and +4°C). β_0 is the intercept, λ , σ , k are the generalized value (GEV) location (μ), scale (σ), and shape (k) parameters respectively. In a GWR, regression coefficients (β) are allowed to vary with the geographic location (u_i, v_i) , j refers to column vectors that contain regression coefficients (β) and the GEV location, scale, and shape parameters used to predict SWE_{pkLoss_i} and ε is the residual error at the i th location. The same explanatory variables (location (μ), scale (σ), and shape (k)) were used to generate ordinary least squares (OLS) regressions (S2) to predict SWE_{pkLoss_i} , the only difference is that in OLS regression, regression coefficients (β) are fixed for a particular regression and are not allowed to vary as a function of geographic location. We compared Akaike Information Criteria corrected for sample size scores [AIC_c; Hurvich and Tsai, 1989] between GWR and OLS regressions; the lowest AIC_c indicates the best model (Tables S2, S4, S6, and S8).

Equation S1 was used to develop a GWR for each warming scenario (+1°C, +2°C, +3°C, and +4°C) for each ecoregion. The generalized value (GEV) location, scale, and shape parameters are fixed quantities, thus the regression coefficients (β) (Tables S3, S5, S7, and S9) change for each warming scenario and describe how peak SWE loss can be modeled as a function of the GEV parameters for a given amount of warming (+1°C, +2°C, +3°C, and +4°C).

As described in Section 3.4 we chose from three commonly used weighting functions, a bi-square, Gaussian, and moving window, to determine the weight that nearby observations receive when calibrating regression coefficients (β) for the i th watershed location. We performed a GWR using the three different weighting functions and selected the weighting function that both produced the lowest Akaike Information Criteria corrected for sample size score [AIC_c; Hurvich and Tsai, 1989] and resulted in the lowest amount of autocorrelation (assessed using Moran's I) in the GWR regression residuals. To determine the bandwidth for each regression/weighting function we used the Golden Section search [Grieg, 1980] and AIC_c to obtain the optimal bandwidth. For

each ecoregion we calculated the minimum and maximum separation distance between HUC-10 centroids and used this range of values to search for the optimal bandwidth

Below, we provide tables and figures that summarize which spatial weighting functions used, the bandwidth values (b in eq. 8 and 9), model diagnostics for the geographically weighted regression and ordinary least squares regression models, and summary statistics of the regression coefficients for the explanatory variables (i.e. the GEV parameters location (μ), scale (σ), and shape (k), denoted below as the Location, Scale, and Shape respectively) for +1°C, +2°C, +3°C, and +4°C for the four ecoregions. Plots of simulated SWE loss (eq. 3 and 4) versus GWR estimates of simulated peak SWE loss (eq. S1), residual plots, and plots of spatial autocorrelation (Moran's I) for simulated, and GWR estimated peak SWE loss and their residuals are provided for each warming scenario.

	+ 1°C		+ 2°C		+ 3°C		+ 4°C	
<i>Model Summary Statistics</i>	GWR	OLS	GWR	OLS	GWR	OLS	GWR	OLS
<i>Number of Watersheds (n)</i>	32	32	32	32	32	32	32	32
<i>Akaike Information Criterion (AICc)</i>	244	261	271	281	272	276	268	268
<i>Coefficient of Determination (r²)</i>	0.83	0.45	0.91	0.79	0.97	0.94	0.98	0.98
<i>F (r²)</i>	13	8	30	35	103	158	267	424
<i>P-value (r²)</i>	<.001	<.001	<.001	<.001	0	0	0	0

Table S2: Summary statistics of model performance for GWR (eq. S1) and OLS (eq. S2) for +1°C to +4°C warming for the Canadian Rockies ecoregion. The lower GWR (except +4°C) AIC_c scores indicates spatial structure in simulated HUC-10 peak SWE losses and that the GWRs perform better than the OLS regressions.

	+ 1°C					+ 2°C				
<i>Variable</i>	Min.	25th %	Median	75th %	Max.	Min.	25th %	Median	75th %	Max.
<i>Intercept</i>	102	138	162	213	354	83	138	170	257	461
<i>Location (m)</i>	-0.124	-0.042	-0.003	0.008	0.017	-0.102	0.015	0.070	0.081	0.098
<i>Scale (m)</i>	-0.281	-0.219	-0.194	-0.163	-0.093	-0.406	-0.318	-0.292	-0.230	-0.138
<i>Shape</i>	-118	-74	-66	-57	-44	-180	-110	-91	-73	-53
	+ 3°C					+ 4°C				
<i>Variable</i>	Min.	25th %	Median	75th %	Max.	Min.	25th %	Median	75th %	Max.
<i>Intercept</i>	-55	-2	22	109	278	-185	-153	-135	-82	18
<i>Location (m)</i>	0.069	0.166	0.211	0.219	0.235	0.264	0.317	0.340	0.347	0.357
<i>Scale (m)</i>	-0.358	-0.249	-0.208	-0.128	-0.052	-0.229	-0.129	-0.080	-0.045	0.016
<i>Shape</i>	-147	-85	-59	-47	-22	-81	-38	-18	-8	7

Table S3: Summary statistics for GWR (eq. S1) coefficients for the GEV explanatory variables location, scale, and shape for the Canadian Rockies ecoregion. A Gaussian spatial weighting function (eq. 9) was used for all warming scenarios. The bandwidths (b , eq. 9) for +1°C, +2°C, +3°C, and +4°C were 46 km, 49 km, 53 km, and 64 km, respectively. The minimum and maximum separation distances between the ecoregion HUC-10 centroids were 13 km and 233 km, respectively.

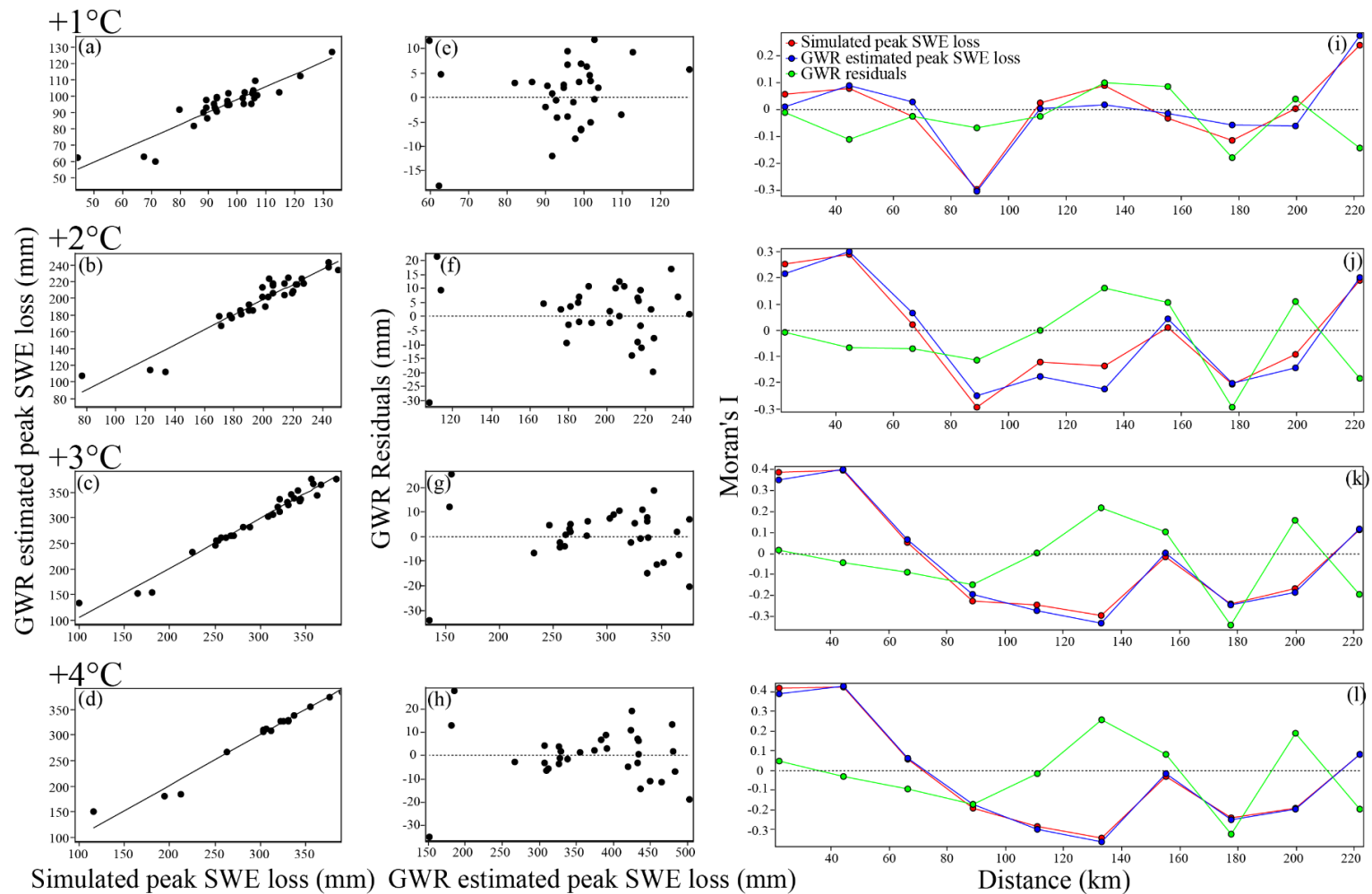


Figure S3: Simulated (eq. 3 and 4) versus GWR estimates of simulated peak SWE loss (eq. S1; a - d), GWR estimates of simulated peak SWE loss versus GWR residuals (e - h) and spatial autocorrelation (Moran's I) for simulated peak SWE loss, GWR estimates of simulated peak SWE loss and the GWR residuals for estimated peak SWE loss (i - l) for +1°C to +4°C for the Canadian Rockies ecoregion. At large separation distances Moran's I is unreliable because few HUC-10 pairs exist at large separation distances.

	+ 1°C		+ 2°C		+ 3°C		+ 4°C	
<i>Diagnostic Statistics</i>	GWR	OLS	GWR	OLS	GWR	OLS	GWR	OLS
<i>Number of Watersheds (n)</i>	163	163	163	163	163	163	163	163
<i>Akaike Information Criterion (AICc)</i>	1027	1239	1179	1466	1277	1566	1245	1552
<i>Coefficient of Determination (r²)</i>	0.97	0.57	0.97	0.41	0.96	0.16	0.97	0.05
<i>F (r²)</i>	50	71	58	37	39	10	43	3
<i>P-value (r²)</i>	0	<.001	<.001	<.001	0	<.001	0	0.047

Table S4: Summary statistics of model performance for GWR (eq. S1) and OLS (eq. S2) for +1°C to +4°C warming for the Idaho Batholith ecoregion. The lower GWR AIC_c scores indicates spatial structure in simulated HUC-10 peak SWE losses and that the GWRs perform better than the OLS regressions.

<i>Variable</i>	+ 1°C					+ 2°C				
	Min.	25th %	Median	75th %	Max.	Min.	25th %	Median	75th %	Max.
<i>Intercept</i>	-11	67	135	173	244	-27	89	262	342	548
<i>Location (m)</i>	-0.092	-0.066	-0.049	-0.009	0.044	-0.198	-0.132	-0.071	0.009	0.085
<i>Scale (m)</i>	-0.176	-0.064	-0.029	0.004	0.082	-0.349	-0.152	-0.061	-0.010	0.144
<i>Shape</i>	-91	-10	-3	8	74	-148	-31	-6	15	151
	+ 3°C					+ 4°C				
<i>Variable</i>	Min.	25th %	Median	75th %	Max.	Min.	25th %	Median	75th %	Max.
<i>Intercept</i>	-48	64	276	467	644	-185	-153	-135	-82	18
<i>Location (m)</i>	-0.213	-0.162	-0.056	0.053	0.122	0.264	0.317	0.340	0.347	0.357
<i>Scale (m)</i>	-0.452	-0.194	-0.080	-0.021	0.101	-0.229	-0.129	-0.080	-0.045	0.016
<i>Shape</i>	-209	-50	-8	8	199	-81	-38	-18	-8	7

Table S5: Summary statistics for GWR (eq. S1) coefficients for the GEV explanatory variables location, scale, and shape for the Idaho Batholith ecoregion. A bi-square spatial weighting function (eq. 8) was used for all warming scenarios. The bandwidth (b , eq. 8) for was fixed at 56 km for +1°C, for +2°C, +3°C, and +4°C a spatially adaptive kernel using 12%, 10%, and 11% of neighbors respectively was used. The minimum and maximum separation distances between the ecoregion HUC-10 centroids were 9 km and 365 km, respectively.

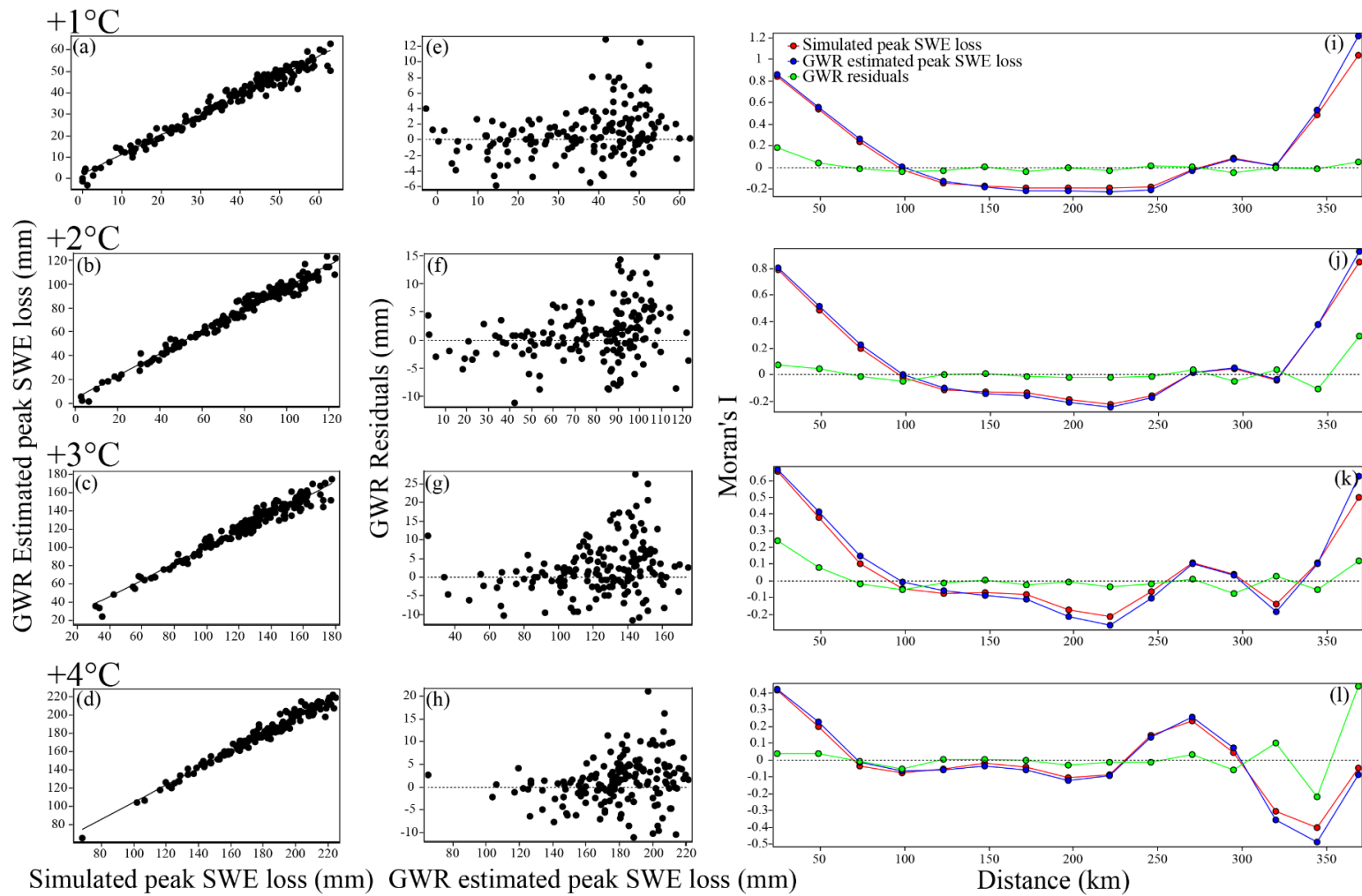


Figure S4: Simulated (eq. 3 and 4) versus GWR estimates of simulated peak SWE loss (eq. S1; a - d), GWR estimates of simulated peak SWE loss versus GWR residuals (e - h) and spatial autocorrelation (Moran's I) for simulated peak SWE loss, GWR estimates of simulated peak SWE loss and the GWR residuals for estimated peak SWE loss (i - l) for +1°C to +4°C for the Idaho Batholith ecoregion. At large separation distances Moran's I is unreliable because few HUC-10 pairs exist at large separation distances.

	+ 1°C		+ 2°C		+ 3°C		+ 4°C	
Diagnostic Statistics	GWR	OLS	GWR	OLS	GWR	OLS	GWR	OLS
<i>Number of Watersheds (n)</i>	268	268	268	268	268	268	268	268
<i>Akaike Information Criterion (AIC_c)</i>	1410	1999	1689	2307	1803	2438	1851	2482
<i>Coefficient of Determination (r²)</i>	0.98	0.41	0.99	0.55	0.99	0.68	0.99	0.78
<i>F (r²)</i>	85	62	127	108	191	185	281	318
<i>P-value (r²)</i>	0	<.001	0	0	0	<.001	0	<.001

Table S6: Summary statistics of model performance for GWR (eq. S1) and OLS (eq. S2) for +1°C to +4°C warming for the Middle Rockies ecoregion. The lower GWR AIC_c scores indicates spatial structure in simulated HUC-10 peak SWE losses and that the GWRs perform better than the OLS regressions.

	+ 1°C					+ 2°C				
Variable	Min.	25th %	Median	75th %	Max.	Min.	25th %	Median	75th %	Max.
<i>Intercept</i>	-73	-46	-7	64	228	-142	-105	-57	70	429
<i>Location (m)</i>	-0.066	0.003	0.031	0.049	0.062	-0.117	0.027	0.077	0.097	0.117
<i>Scale (m)</i>	-0.127	-0.060	-0.022	0.022	0.091	-0.251	-0.102	-0.006	0.054	0.189
<i>Shape</i>	-80	-11	-1	7	49	-163	-17	1	18	95
	+ 3°C					+ 4°C				
Variable	Min.	25th %	Median	75th %	Max.	Min.	25th %	Median	75th %	Max.
<i>Intercept</i>	-224	-161	-121	27	572	-306	-212	-171	-37	652
<i>Location (m)</i>	-0.147	0.072	0.123	0.142	0.176	-0.151	0.113	0.157	0.181	0.227
<i>Scale (m)</i>	-0.335	-0.108	0.015	0.084	0.252	-0.355	-0.093	0.057	0.116	0.285
<i>Shape</i>	-228	-21	7	28	124	-256	-15	13	38	127

Table S7: Summary statistics for GWR (eq. S1) coefficients for the GEV explanatory variables location, scale, and shape for the Middle Rockies ecoregion. A bi-square spatial weighting function (eq. 8) was used for all warming scenarios. The bandwidth (b , eq. 8) for +1°C, +2°C, +3°C, and +4°C were 69 km, 65 km, 65 km, and 65 km, respectively. The minimum and maximum separation distances between the ecoregion HUC-10 centroids were 7 km and 626 km, respectively.

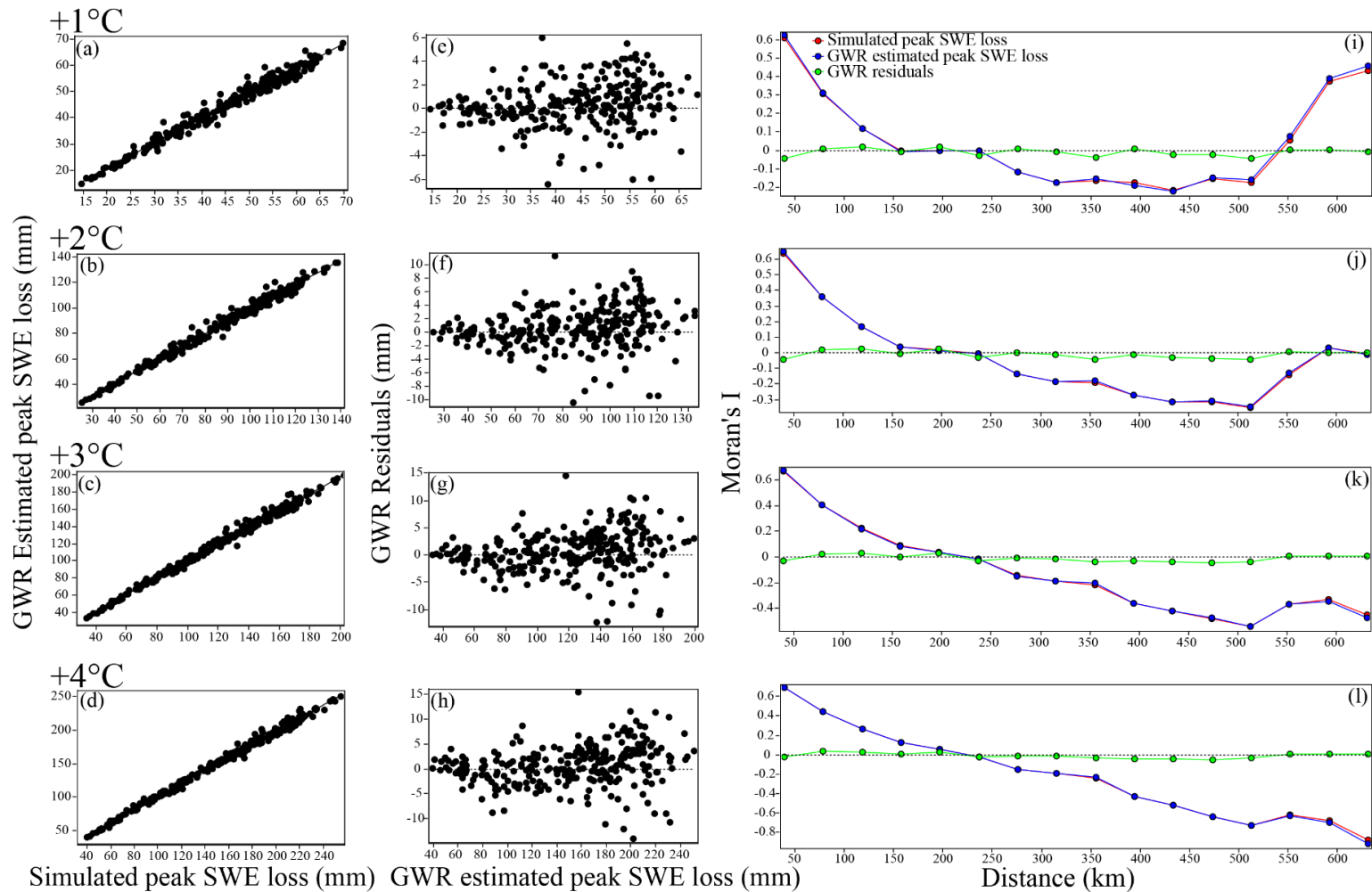


Figure S5: Simulated (eq. 3 and 4) versus GWR estimates of simulated peak SWE loss (eq. S1; a - d), GWR estimates of simulated peak SWE loss versus GWR residuals (e - h) and spatial autocorrelation (Moran's I) for simulated peak SWE loss, GWR estimates of simulated peak SWE loss and the GWR residuals for estimated peak SWE loss (i - l) for +1°C to +4°C for the Middle Rockies ecoregion. At large separation distances Moran's I is unreliable because few HUC-10 pairs exist at large separation distances.

	+ 1°C		+ 2°C		+ 3°C		+ 4°C	
Diagnostic Statistics	GWR	OLS	GWR	OLS	GWR	OLS	GWR	OLS
<i>Number of Watersheds (n)</i>	171	171	171	171	171	171	171	171
<i>Akaike Information Criterion (AICc)</i>	934	1092	1079	1258	1148	1347	1203	1414
<i>Coefficient of Determination (r²)</i>	0.995	0.96	0.996	0.97	0.997	0.98	1.00	0.98
<i>F (r²)</i>	361	1395	593	2062	797	2461	865	2518
<i>P-value (r²)</i>	0	0	0	0	0	<.001	<.001	<.001

Table S8: Summary statistics of model performance for GWR (eq. S1) and OLS (eq. S2) for +1°C to +4°C warming for the Northern Rockies ecoregion. The lower GWR AIC_c scores indicates spatial structure in simulated HUC-10 peak SWE losses and that the GWRs perform better than the OLS regressions.

	+ 1°C					+ 2°C				
Variable	Min.	25th %	Median	75th %	Max.	Min.	25th %	Median	75th %	Max.
<i>Intercept</i>	-91	-70	-59	-39	90	-197	-154	-134	-113	64
<i>Location (m)</i>	0.036	0.108	0.119	0.128	0.150	0.101	0.211	0.237	0.253	0.300
<i>Scale (m)</i>	-0.150	0.009	0.054	0.087	0.141	-0.209	0.079	0.130	0.172	0.265
<i>Shape</i>	-48	-2	12	19	27	-63	13	30	41	58
	+ 3°C					+ 4°C				
Variable	Min.	25th %	Median	75th %	Max.	Min.	25th %	Median	75th %	Max.
<i>Intercept</i>	-331	-245	-209	-172	-36	-455	-325	-276	-219	-112
<i>Location (m)</i>	0.188	0.291	0.336	0.365	0.437	0.213	0.349	0.414	0.458	0.555
<i>Scale (m)</i>	-0.179	0.165	0.213	0.246	0.361	-0.101	0.231	0.281	0.316	0.431
<i>Shape</i>	-55	27	51	62	103	-79	40	70	88	143

Table S9: Summary statistics for GWR (eq. S1) coefficients for the GEV explanatory variables location, scale, and shape for the Middle Rockies ecoregion. A bi-square spatial weighting function (eq. 8) was used for all warming scenarios. The bandwidth (b , eq. 8) for +1°C, +2°C, +3°C, and +4°C were 68 km, 71 km, 73 km, and 72 km, respectively. The minimum and maximum separation distances between the ecoregion HUC-10 centroids were 7 km and 433 km, respectively.

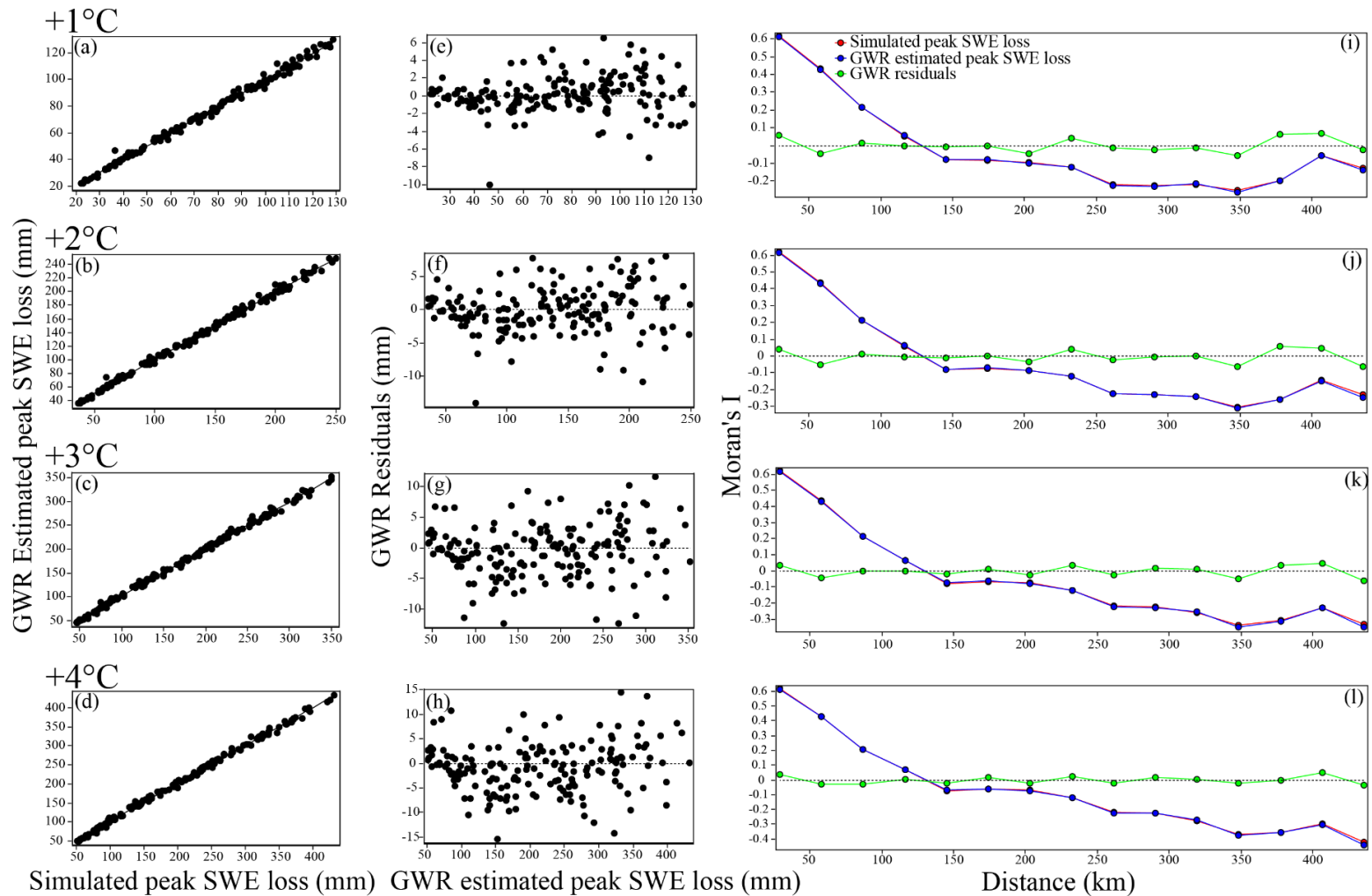


Figure S6: Simulated (eq. 3 and 4) versus GWR estimates of simulated peak SWE loss (eq. S1; a - d), GWR estimates of simulated peak SWE loss versus GWR residuals (e - h) and spatial autocorrelation (Moran's I) for simulated peak SWE loss, GWR estimates of simulated peak SWE loss and the GWR residuals for estimated peak SWE loss (i - l) for +1°C to +4°C for the Northern Rockies ecoregion. At large separation distances Moran's I is unreliable because few HUC-10 pairs exist at large separation distances

Freedman, D., and P. Diaconis (1981), On the histogram as a density estimator: L 2 theory, *Probability theory and related fields*, 57(4), 453-476.

Grieg, D. M. (180), *Optimisation*, London, Longman, p. 192.

Hurvich, C. M., and C.-L. Tsai (1989), Regression and time series model selection in small samples, *Biometrika*, 76(2), 297-307.

Rangel, T. F., J. A. F. Diniz, and L. M. Bini (2010), SAM: a comprehensive application for Spatial Analysis in Macroecology, *Ecography*, 33(1), 46-50.

7 Appendix 3

Supporting Information for:

The influence of elevation, aspect, and vegetation on seasonal snowpack: case studies from five mountain Critical Zone Observatories across the western U.S.

Group	d.f.	Sums of squares	Mean S.S.	F-ratio	P value of F-ratio
<i>Aspect</i>	3	11249	3750	36.24	< 2e-16
<i>Vegetation Height</i>	2	178548	89274	862.96	< 2e-16
<i>Aspect x Vegetation Height</i>	6	16553	2759	26.67	< 2e-16

Table S1: ANOVA results for mean snow depths in aspect, vegetation height, and aspect x vegetation height groups for BCW. The low p values indicate that the mean snow depths between the groups are significantly different. The abbreviations d.f. and S.S. are degrees of freedom and sum of squares respectively.

Group	d.f.	Sums of squares	Mean S.S.	F-ratio	P value of F-ratio
<i>Aspect</i>	3	53170174	17723391	203.42 1	< 2e-16
<i>Vegetation Height</i>	1	3496188	34961884	40.128	2.65E-10
<i>Aspect x Vegetation Height</i>	3	2190795	730265	8.382	1.50E-05

Table S2: ANOVA results for mean snow depths in aspect, vegetation height, and aspect x vegetation height groups for JRB. The low p values indicate that the mean snow depths between the groups are significantly different. The abbreviations d.f. and S.S. are degrees of freedom and sum of squares respectively.

Group	d.f.	Sums of squares	Mean S.S.	F-ratio	P value of F-ratio
<i>Aspect</i>	3	24141	8047	255.4	<2e-16
<i>Vegetation Height</i>	1	240777	240777	7641.6	<2e-16
<i>Aspect x Vegetation Height</i>	3	1087	362	11.5	2.00E-07

Table S3: ANOVA results for mean snow depths in aspect, vegetation height, and aspect x vegetation height groups for RCEW. The low p values indicate that the mean snow depths between the groups are significantly different. The abbreviations d.f. and S.S. are degrees of freedom and sum of squares respectively.

Group	d.f.	Sums of squares	Mean S.S.	F-ratio	P value of F-ratio
<i>Aspect</i>	3	43120121	14373374	71.092	< 2e-16
<i>Vegetation Height</i>	2	78591236	39295618	194.36 1	< 2e-16
<i>Aspect x Vegetation Height</i>	6	7532358	1255393	6.209	2.06E-06

Table S4: ANOVA results for mean snow depths in aspect, vegetation height, and aspect x vegetation height groups for KREW. The low p values indicate that the mean snow depths between the groups are significantly different. The abbreviations d.f. and S.S. are degrees of freedom and sum of squares respectively.

Group	d.f.	Sums of squares	Mean S.S.	F-ratio	P value of F-ratio
<i>Aspect</i>	3	102794732	34264911	123.65 7	< 2e-16
<i>Vegetation Height</i>	2	384017640	19200882 0	692.92 9	< 2e-16
<i>Aspect x Vegetation Height</i>	6	14736817	2456136	8.864	0.000001

Table S5: ANOVA results for mean snow depths in aspect, vegetation height, and aspect x vegetation height groups for WOLV. The low p values indicate that the mean snow depths between the groups are significantly different. The abbreviations d.f. and S.S. are degrees of freedom and sum of squares respectively.